

# Circuit Modelling of Submerged Arc Furnaces and Their Power Supply Systems

**Ida Monsen**

Computational Science: Physics  
60 ECTS study points

Department of Physics  
Faculty of Mathematics and Natural Sciences



**Ida Monsen**

Circuit Modelling of Submerged Arc  
Furnaces and Their Power Supply  
Systems

Supervisors:  
Vetle Kjær Risinggård  
Morten Hjorth-Jensen



## Abstract

Most submerged arc smelting furnaces consist of three grid connections and three transformers, sending high currents into three electrodes standing in a metal bath. Optimal electrical conditions are integral both for energy efficiency and for product quality, but direct observation of the system is practically impossible due to high temperatures and magnetic fields. We must therefore resort to modelling. In this thesis we develop simplified linear circuit models of such a three-phase system that includes both the primary and the secondary sides of the transformers, that is both the grid connection and the furnace itself. Using different symmetry assumptions we solve separate circuit models of the primary and secondary sides analytically. Then we implement a numerical solver using graph theory to solve the more complex circuit models.

We define a circuit model for low-voltage compensation, where the capacitors for power factor correction are placed on the secondary side. Using low-voltage compensation with our chosen parameters we get a maximum transformer power factor of 0.999, compared to 0.6430 with high-voltage compensation, but the capacitors have to withstand currents that are 59 times higher. We lastly compare our circuit model to measurements from a ferrosilicon furnace, and find the model to agree well with the measurements, being able to reproduce both the trends and in many cases absolute values of the measurements. After scaling all values to between 0 and 1, the r.m.s. error is of the order  $10^{-3}$  to  $10^{-4}$ . This shows that a simplified linear circuit model is able to capture most of the electrical behaviour of the furnace and supply system.



## Samandrag

Dei fleste metallurgiske smelteomnar består av tre uttak frå straumnettet og tre transformatorar, som vidare sender kraftige straumar gjennom tre elektrodar plassert i eit metallbad. Det er essensielt å ha optimale elektriske forhold, både av omsyn til effektivt energibruk og produktkvalitet, men høge temperaturar og magnetiske felt gjer direkte observasjonar av systemet praktisk talt umogleg. Modellering er derfor mykje brukt for å få betre forståing av og til å simulera systemet. I denne oppgåva utviklar me forenkla kretsmodellar av slike trefasesystem som inneheld både primærsida og sekundærsida av transformatorane, det vil seia både koplinga til straumnettet og omnen sjølv. Me løyser separate kretsmodellar for primærsida og sekundærsida analytisk. Deretter implementerer me ein numerisk løysingsmetode basert på kretsteori, som me bruker til å løysa meir komplekse kretslikningar.

Me definerer ein kretsmodell for lågspennings-kompensasjon, kor kondensatorane for å korrigera effektfaktoren er plassert på sekundærsida. Lågspennings-kompensasjon med våre parameterverdiar gjer ein maksimal effektfaktor i transformatorane på 0.999, samanlikna med 0.6430 for høgspennings-kompensasjon, men kondensatorane må tola straumar som er 59 gonger høgare. Til slutt samanliknar me kretsmodellen med målingar frå ein smelteovn for ferrosilisium. Me finner at modellen samsvarer godt med målingane, dei klarer å reprodusera både trendane og i mange høve absoluttverdiar til målingane ganske presist. Etter å ha skalert alle verdiar til mellom 0 og 1 er r.m.s.-feilen i storleiksorden  $10^{-3}$  to  $10^{-4}$ . Dette viser at ein forenkla lineær kretsmodell er i stand til å gjenskapa størstedelen av den elektriske oppførselen til omnen og forsyningssystemet.





# Acknowledgements

First, a huge thank you to my main supervisor Vetle. Our weekly Monday meetings filled with guidance and many laughs always charged me up for a new week. Thank you for giving me many possibilities to grow and for always believing in my abilities. I am also grateful to the rest of the people at NORCE for giving me a warm welcome and including me in your activities from the very start. To my co-supervisor Morten, thank you for helping me find a direction at the start of my master's studies and for saying yes to co-supervise even though you had more than enough to do already.

To my fellow students at the CCSE office and otherwise, thank you for a fun and inspiring study environment, good lunch conversations, table tennis and card games. You have made long days at the office much more enjoyable than they could have been. To the teachers and advisers who believed in me and supported me at important points throughout my education, I would not be where I am today without you. A special thank you to Signe, who gave me the ninth year maths textbook in eighth grade without asking my parents first. They wholeheartedly agreed afterwards, of course.

Thank you to mom and dad for always encouraging my curiosity, supporting all my endeavours, and showing interest in what I do. I could not ask for better or kinder parents. And lastly, thank you to my partner Bård. For countless maths and physics conversations, even when they are maths jokes at my expense, for being so generous with me when I am busy or tired, and for reminding me that there is a life outside of the study bubble. I am forever grateful for having you by my side.



# Contents

<b>1</b>	<b>Introduction</b>	<b>1</b>
1.1	Smelting furnaces . . . . .	1
1.1.1	Silicon and ferrosilicon . . . . .	1
1.1.2	Submerged arc furnaces. . . . .	2
1.1.3	Furnace models . . . . .	2
1.2	Research objective . . . . .	4
1.3	Thesis outline . . . . .	4
<b>2</b>	<b>Circuit theory</b>	<b>7</b>
2.1	Transformers . . . . .	10
2.2	Three-phase systems . . . . .	11
2.2.1	Symmetrical components . . . . .	12
2.3	Power factor correction . . . . .	13
2.3.1	High-voltage compensation. . . . .	13
<b>3</b>	<b>Graph theory</b>	<b>15</b>
3.1	Definitions . . . . .	15
3.2	Results for digraphs. . . . .	17
3.3	Finding a basis of $\ker(\mathcal{A})$ . . . . .	18
3.4	Solving circuit problems with graph theory . . . . .	18
3.4.1	General case . . . . .	18
3.4.2	Harmonic problems. . . . .	20
<b>4</b>	<b>Circuit models and other furnace theory</b>	<b>23</b>
4.1	Circuit models . . . . .	23
4.1.1	Secondary side . . . . .	23
4.1.2	Primary side . . . . .	24
4.1.3	Full equivalent circuit . . . . .	24
4.1.4	Low-voltage compensation . . . . .	26
4.2	Defining circulating currents. . . . .	26
4.2.1	Secondary side . . . . .	27
4.2.2	Primary side . . . . .	27
4.3	A furnace metamodel . . . . .	28
4.4	Electrical furnace control . . . . .	28
4.5	Measurement strategies . . . . .	29
4.5.1	Electrode currents . . . . .	29
4.5.2	Rogowski coils . . . . .	29
4.5.3	The Bøckman method. . . . .	30

<b>5</b>	<b>Analytical solutions</b>	<b>33</b>
5.1	Secondary side . . . . .	33
5.1.1	Balanced circuit . . . . .	34
5.1.2	Unbalanced electrodes . . . . .	35
5.1.3	Unbalanced transformers . . . . .	35
5.2	Primary side . . . . .	36
5.2.1	Balanced circuit . . . . .	37
5.2.2	Unbalanced capacitors . . . . .	39
5.2.3	Unbalanced transformers . . . . .	39
5.2.4	Power factor and capacitance . . . . .	39
<b>6</b>	<b>Implementation and preliminary results</b>	<b>43</b>
6.1	Implementation . . . . .	43
6.2	Validation . . . . .	44
6.3	Full system preliminary results. . . . .	46
6.3.1	Estimating transformer parameters . . . . .	47
6.3.2	Comparison with separate models . . . . .	48
6.4	Discussion . . . . .	50
<b>7</b>	<b>Low-voltage compensation</b>	<b>53</b>
7.1	Discussion . . . . .	57
<b>8</b>	<b>Metamodel simulations</b>	<b>59</b>
8.1	Interaction effect . . . . .	59
8.2	Discussion . . . . .	61
<b>9</b>	<b>Measurement comparison</b>	<b>63</b>
9.1	Data preprocessing . . . . .	63
9.1.1	Phase and amplitude estimation . . . . .	63
9.1.2	Scaling . . . . .	64
9.1.3	Choosing which measurements to use . . . . .	64
9.2	Data exploration . . . . .	65
9.3	Comparison. . . . .	67
9.4	Discussion . . . . .	72
<b>10</b>	<b>Conclusion</b>	<b>75</b>
10.1	Summary. . . . .	75
10.2	Future work. . . . .	76
<b>A</b>	<b>Circuit diagram symbols</b>	<b>77</b>
<b>B</b>	<b>Analytical current solutions</b>	<b>79</b>
<b>C</b>	<b>The Fourier and discrete Fourier transforms</b>	<b>81</b>
<b>D</b>	<b>Results for second data set</b>	<b>83</b>

# List of Figures

1.1	Drawing of a submerged arc smelting furnace, courtesy of Hannesson [7]	3
2.1	Circuit diagram of ideal an transformer . . . . .	11
2.2	Circuit diagram of a non-ideal transformer. . . . .	11
2.3	Circuit diagram of a non-ideal transformer approximation suitable for medium-sized and large transformers. . . . .	11
2.4	The two types of three-phase circuit connections . . . . .	12
3.1	Example drawing of a directed graph . . . . .	16
4.1	Circuit diagrams of (a) the secondary side equivalent circuit and (b) the primary side equivalent circuit . . . . .	24
4.2	Circuit diagram of the full system, with the primary and secondary sides connected through non-ideal transformers . . . . .	25
4.3	Circuit diagram of the full system with low-voltage compensation . . . . .	26
4.4	Schematic drawing of a Rogowski coil setup [42] . . . . .	30
4.5	Schematic drawing of electrode voltage measurement with the Bøckman method. . . . .	31
5.1	Directed graphs of (a) the secondary side circuit and (b) the primary side circuit	34
6.1	Primary side circulating currents for the case where one transformer has a different resistance $R_{p1}$ and reactance $X_{p1}$ from the other two transformers, calculated from the primary side circuit model . . . . .	46
6.2	Secondary side circulating currents for the case where one voltage source has a different magnitude from the two others, calculated with the secondary side circuit model. . . . .	46
6.3	Directed graph of the full system . . . . .	47
6.4	Time series of currents covering two periods, calculated both with the full circuit model <i>HVC</i> and with the separate models <i>Primary</i> and <i>Secondary</i> . . . . .	49
6.5	Circulating currents in primary and secondary side deltas when one transformer has a different windings ratio from the other two, calculated with the circuit models <i>HVC</i> , <i>Primary</i> , and <i>Secondary</i> . . . . .	50
6.6	The power factor seen from the grid as a function of capacitance, calculated both with the circuit model <i>HVC</i> and the circuit model <i>Primary</i> . . . . .	50
7.1	Directed graph of the full system circuit model with low-voltage compensation	54
7.2	Behaviour of some power factors, powers, currents and voltages in different parts of the system as a function of capacitance, for both low-voltage compensation and high-voltage compensation . . . . .	55

## List of Figures

7.3	LVC to HVC ratio of optimal capacitance, capacitor current and capacitor voltage as a function of transformer windings ratio . . . . .	57
8.1	Clamp positions and electrode resistances from a ferromanganese metamodel simulation of operation with resistance control . . . . .	60
8.2	An example of the resistance interaction effect in the metamodel . . . . .	61
8.3	The zero sequence component $V_0$ of the electrode voltages from the interaction example plotted in the complex plane . . . . .	62
9.1	Time series of two periods of high-resolution measurement data for current in electrode 1, voltage over electrode 1, and voltage over transformer A calculated from electrode voltages. . . . .	65
9.2	Phase differences between the three electrode currents . . . . .	65
9.3	Imbalance in high-resolution measurement data, calculated from symmetrical components . . . . .	66
9.4	The absolute value of the symmetrical components for high-resolution electrode voltage measurements . . . . .	66
9.5	The zero sequence component $V_0$ of electrode voltage from 20 minutes of high-resolution measurement data plotted in the complex plane . . . . .	67
9.6	Comparison of r.m.s. values from process data and r.m.s. values calculated from high-resolution measurement data for the data set of 20 minutes . . . . .	68
9.7	Comparison of r.m.s. current values from the full equivalent circuit model <i>HVC</i> and r.m.s. current values from high-resolution measurement data for the data set of 20 minutes . . . . .	69
9.8	Comparison of r.m.s. voltage values from the full equivalent circuit model <i>HVC</i> and r.m.s. voltage values from high-resolution measurement data for the data set of 20 minutes . . . . .	70
9.9	Comparison of power factor from the full equivalent circuit model <i>HVC</i> and power factor from high-resolution measurement data for the data set of 20 minutes . . . . .	71
D.1	Comparison of r.m.s. values from process data and r.m.s. values calculated from high-resolution measurement data for the data set of 3.75 minutes . . . . .	83
D.2	Comparison of r.m.s. current values from the full equivalent circuit model <i>HVC</i> and r.m.s. current values from high-resolution measurement data for the data set of 3.75 minutes . . . . .	84
D.3	Comparison of r.m.s. voltage values from the full equivalent circuit model <i>HVC</i> and r.m.s. voltage values from high-resolution measurement data for the data set of 3.75 minutes . . . . .	85
D.4	Comparison of power factor from the full equivalent circuit model <i>HVC</i> and power factor from high-resolution measurement data for the data set of 3.75 minutes . . . . .	86

# List of Tables

6.1	The parameter values used for numerical solutions to the primary side circuit	45
6.2	The parameter values used for numerical solutions to the secondary side circuit	45
6.3	The parameter values used for numerical solutions to the full system . . .	48
7.1	Optimal capacitance and other circuit values at this optimal capacitance, for both high-voltage and low-voltage compensation . . . . .	54
7.2	Slope and intercept of a first-order linear regression done on logarithmic data of transformer winding ratio versus ratio of LVC values to HVC values for several quantities . . . . .	56
8.1	The slope of the lines in Fig. 8.2, where we move two electrodes in sync and observe the change in resistance for all three electrodes . . . . .	61
9.1	R.m.s. error of values calculated with the full circuit model compared to high-resolution measurement data . . . . .	72
D.1	R.m.s. error of values calculated with the full circuit model compared to high-resolution measurement data for the data set of 3.75 minutes . . . . .	87

## List of Tables



# Chapter 1

## Introduction

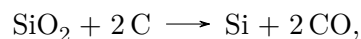
### 1.1 Smelting furnaces

Smelting is a process used to extract desired metals from some raw materials. The technology of smelting furnaces was developed early in the 20th century and is today the leading method for producing ferroalloys [1]. Smelting furnaces can be divided into open arc furnaces, where there is a visible arc, and submerged arc furnaces, where there is no visible arc because the electrodes are buried in the material inside the furnace [2]. There is still room for improvements in the smelting process, for example when it comes to cost reduction, better energy utilisation, and lower emissions [1]. In this thesis we will try to understand the electrical conditions of submerged arc furnaces better, by developing and studying equivalent circuit models of the furnace and supply system. We will use methods that are applicable to ferroalloy submerged arc furnaces in general, but we will mostly use specific values from a ferrosilicon furnace. We therefore focus on silicon and ferrosilicon furnaces in this introduction.

#### 1.1.1 Silicon and ferrosilicon

Silicon (Si) is the 14th element of the periodic table. It is not a metal, but has metallic properties in liquid form and is a semiconductor in solid form [3]. The use of silicon and ferrosilicon can be divided into four main groups [3]. The two first are as alloys in steel and aluminium. Ferrosilicon, alloys of silicon and iron in various forms, is most commonly used in steel alloys, while pure silicon is more desirable in aluminium alloys. Third, pure silicon and ferrosilicon with a high silicon content is used to make silicone in various forms. Silicones have many uses, for example in medicine, in cookware, as lubricants and as insulators. And lastly, silicon is used in electronics for its property as a semiconductor.

The natural source of silicon is quartz or quartzite. Quartz consists of silica, the silicon oxide  $\text{SiO}_2$ , and quartzite consists of quartz mixed with other materials [3]. Silicon and ferrosilicon is produced by smelting, the goal of which is, simply put, to remove the oxygen by a reduction reaction with carbon such that we are left with the silicon or ferrosilicon, depending on whether a source of iron is present. Coke and coal are typically used as carbon sources, and iron oxide is used as an iron source [4]. The simplified, unbalanced chemical equation for pure silicon is



but the reactions are more complex in reality [3], [4]. For example, silicon monoxide (SiO) gas and solid silicon carbide (SiC) are also formed [3]. The desired chemical

reactions are endothermic, meaning that they require energy input, usually in the form of heat.

Most ferroalloys, including silicon alloys, are produced in three-phase electric smelting furnaces, with three electrodes and a circular design, that operates with powers at the scale of tens of MVA [3], [4]. The needed heat is supplied by sending electric currents through the electrodes and coke bed, causing heat dissipation due to the elements' resistance. The production of pure silicon and ferrosilicon are very similar to each other, with the presence of iron being the biggest difference. The process typically consumes electricity of up to about 8000 kWh per tonne ferrosilicon [5] and reaches temperatures of about 2000° C [4]. As of 2010 the annual world production of silicon was  $1.8 \cdot 10^9$  kg [3]. The leading production countries are China, Brazil, Norway, the United States, and France, with China alone producing almost 50 percent of the world's silicon [3].

### 1.1.2 Submerged arc furnaces

An electric arc smelting furnace consists of a steel shell, carbon electrodes fastened to clamps so that their position can be adjusted, feed chutes for adding raw material and tap holes to extract the metal and slag [4]. When high currents are sent into the electrodes, it creates electric arcs from the electrode tips to the furnace contents. The heat dissipation in the arcs and due to resistance in the materials create a high enough temperature for the reduction reactions to take place [4], [6]. The three electrodes are fastened in holders with a slip system, so that more of the electrode can be fed into the furnace as the tip is consumed in reactions [6]. The electrical supply system consists of grid connections and capacitors on the primary side, transformers, and bus bars and flexible conductors on the secondary side that connect the transformers to the electrodes [2]. The transformers can change tap positions to vary the voltage supplied to the secondary side [4].

In a submerged arc furnace the electrodes are immersed in the furnace contents and there are no visible arcs. A typical smelting furnace is circular, with three electrodes arranged in an equilateral triangle and receiving three-phase AC current from three single-phase transformers or one three-phase transformer, but other configurations are possible [6]. Figure 1.1 shown a drawing of a submerged arc smelting furnace, drawn by Hannesson [7]. The drawing depicts a ferrosilicon furnace, but the general construction is the same for other types of submerged arc furnaces as well.

The resistance in the furnace depends on factors like temperature, material composition, and furnace geometry such as electrode position and electrode diameter. These factors will vary under operation, and therefore so will the resistance. Electrode position is the only factor that can be easily controlled, and is therefore used to adjust the resistance in operation control [4]. Proper furnace control gives the benefit of both better product quality and more efficient electricity usage [6], [8], and small improvements in electrical conditions can give significantly better profit [8].

### 1.1.3 Furnace models

We cannot directly observe or measure the inner workings of a submerged arc furnace due to the high temperatures and strong magnetic fields present. Much work has therefore been done on modelling electrical conditions of furnaces. We can divide the models roughly into four types: (1) empirical models, (2) analytical models based on models of charge conductivity, (3) physics-based mathematical models describing some or all of

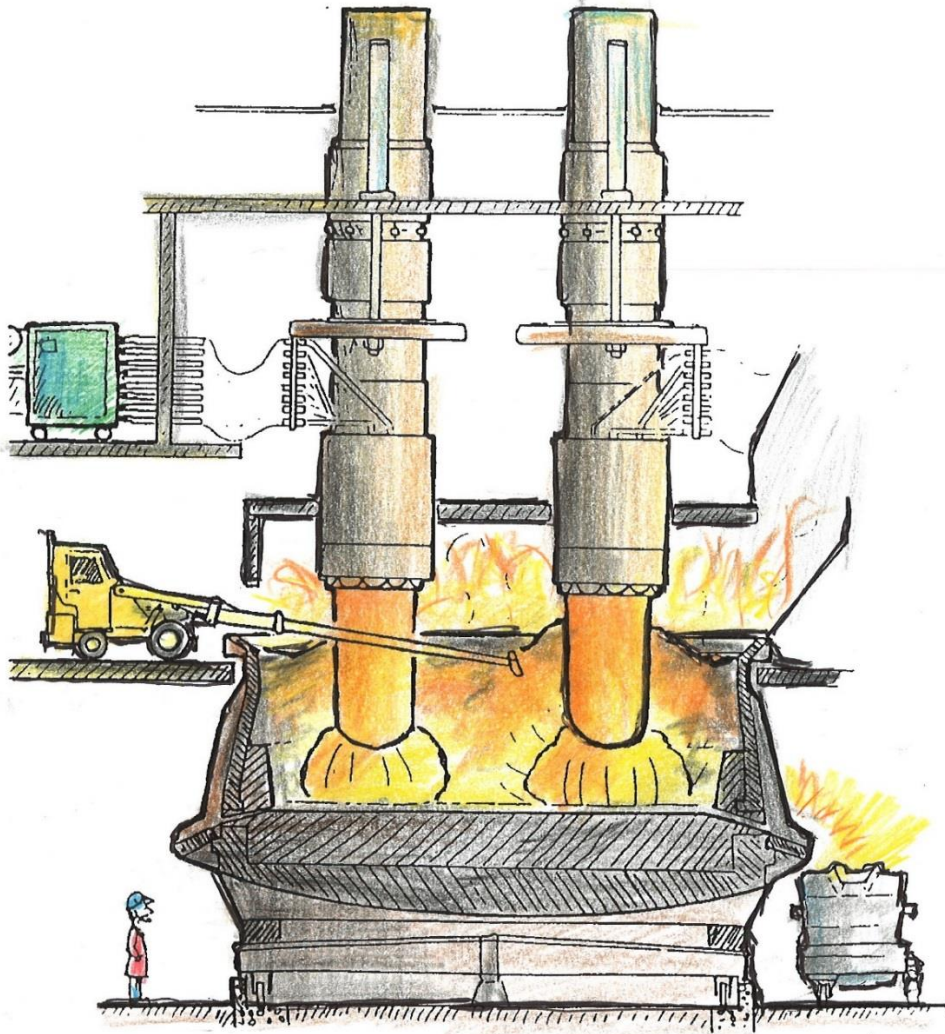


Figure 1.1: Drawing of a submerged arc smelting furnace, courtesy of Hannesson [7]. The cross section shows two of the three electrodes.

the electrical, magnetic and thermal conditions, chemical reactions, and heat and mass flow, and lastly (4) equivalent circuit models [4].

Physics-based models are common, with many different variations, see for example [9]–[19]. Some of these models are two-dimensional, some are three-dimensional, they might consider only one electrode or all three electrodes at once, use alternating current or simplify to direct current. Physics-based models are often good at studying details like current paths or heat distribution in specific parts of the furnace, but they are computationally costly.

Equivalent circuit models of submerged arc furnaces have been studied by for example [2], [4], [20], but circuit models are more commonly used for open arc furnaces [4]. Circuit models are computationally lightweight compared to physics-based models, but require that we assume current paths as part of the model design and strictly limit the analyses to electrical conditions.

## 1.2 Research objective

As described above, efforts have been made to analyse equivalent circuits of submerged-arc furnaces before, but they have focused on models of the secondary side. In this thesis we will also use circuit models, but unlike the other approaches we will develop and study a model of the secondary and primary sides together. Thus, the goal of our work is not to study the details of what happens inside the furnace, but rather to develop and study a model that can give an overview over the electrical conditions and behaviours of the entire system, both the power supply and the furnace itself. This gives us the option to look at how the primary side effects electrical conditions on the secondary side and vice versa.

We want a model that is as simple as possible, yet retains the most important aspects of the supply and furnace system. We therefore assume that the circuit is linear and that there are no higher harmonics present, although the arc is non-linear and therefore generate higher harmonics [2], [21]. We also limit ourselves to stationary models, although furnaces in truth are dynamic systems. A significant part of the thesis will be dedicated to evaluating how well our simplified system is able to represent the true system.

## 1.3 Thesis outline

Chapter 2 presents the circuit theory needed to understand the rest of this thesis, and here we go through all relevant circuit components and electrical concepts. We particularly look at transformers, three-phase systems, and power factor correction. Chapter 3 starts with a rigorous presentation of relevant graph theory, and goes on to detail how we use graph theory to solve circuit problems. We start with a general solution strategy and then explain how the problem simplifies when we restrict ourselves to harmonic problems. In Chapter 4 we look more closely at the furnace and power supply system. We develop circuit models for the secondary side, the primary side, and the whole system combined, and present a previously developed furnace metamodel that we will later make use of in simulations. The chapter ends with a presentation of electrical control strategies for submerged arc furnaces and how to make measurements of a furnace during operation.

Chapter 5 presents analytical solutions for the primary and secondary side circuit models, as they are small enough that we do not need numerics. We study the effect of

introducing unbalanced elements into the circuits, and for the primary side we look at the connection between capacitance and the grid power factor. In Chapter 6 we implement a numerical solver based on the graph solution method and verify it by comparing the analytical and numerical solutions of the primary and secondary side circuits. Then we solve the circuit model of the whole system and compare it with the solution of the two separate circuit models.

In Chapter 7 we study a circuit model of a furnace with low-voltage compensation. We compare and contrast it with the standard high-voltage compensation, studying the effects in different parts of the furnace and supply system. Chapter 8 uses the metamodel to implement and run simulations of a furnace operating with a resistance controller. We present an example showing that there is an interaction effect in the control simulation. In Chapter 9 we look at measurement data from a ferrosilicon furnace in operation. We first process and inspect the data itself, before comparing the measurement data to our circuit model. And finally, we conclude in Chapter 10.



## Chapter 2

# Circuit theory

We start by summarising the fundamental circuit theory that we will need. Kirchhoff's laws describe conditions for the currents and voltages in circuits due to conservation of charge and energy, respectively. Kirchhoff's current law states that

$$\sum_i I_i = 0 \quad (2.1)$$

for the currents  $I_i$  going into any circuit junction and Kirchhoff's voltage law states that

$$\sum_i V_i = 0 \quad (2.2)$$

for the potential differences  $V_i$  over any closed loop in a circuit [22]. The unit for current is ampere (A) and the unit for voltage or potential difference is volt (V).

We divide power supply into direct current (DC) and alternating current (AC). AC is common in both domestic and industrial applications, and an AC signal typically varies as a sine wave. The instantaneous current  $i$  can then be written as

$$i = I_p \sin(\omega t + \phi),$$

where  $I_p$  is the peak current or amplitude of the signal,  $\omega$  is the angular frequency,  $t$  is the time in seconds and  $\phi$  is a phase shift. It is often useful to use complex notation, with the complex current written as

$$I = I_p e^{j(\omega t + \phi - \pi/2)},$$

where  $j$  is the imaginary unit. This complex notation is sometimes called a phasor. The real current is the real part of the above expression,

$$i = \text{Re} \left( I_p e^{j(\omega t + \phi - \pi/2)} \right).$$

We assume all signals to be AC sinusoidal signals unless otherwise specified. Throughout the thesis we will use several different ways of stating currents and voltages, being careful to specify which representation we are using when.

The relevant circuit components are resistors, inductors and capacitors, with characteristic relationships between the instantaneous current  $i$  through and voltage  $v$  over the component. A resistor represent a non-perfect conducting material. For a resistor

$$v = Ri, \quad (2.3)$$

where  $R$  is the resistance measured in ohm ( $\Omega$ ). The greater the resistance, the less conductive the material is. In a resistor the current and voltage are in phase with each other.

An inductor represents an element where changing current induces a voltage counteracting the change. This happens for example in a coiled-up wire. For an inductor

$$v = L \frac{di}{dt}, \quad (2.4)$$

where  $L$  is the inductance measured in henry (H). In an inductor with a sinusoidal current, the voltage is ahead of the current by  $\pi/2$  radians, and an inductive element will in general have a voltage leading the current.

And finally, a capacitor is an element that can store and release electric charge. Two parallel conducting plates with an insulating layer between them acts as a capacitor. For a capacitor,

$$v = \frac{1}{C} \int i dt, \quad (2.5)$$

where  $C$  is the capacitance measured in farad (F). In a conductor with a sinusoidal current, the voltage is behind the current by  $\pi/2$  radians, and the voltage will in general lag the current in a capacitive element.

We will also use magnetically coupled components, that is components with mutual inductance where a changing current in one component induces a voltage in the other. The relationship between instantaneous current  $i_1$  in component 1 and voltage  $v_2$  in component 2 is given by

$$v_2 = M \frac{di_1}{dt}, \quad (2.6)$$

and the vice versa.  $M$  is called mutual inductance and is, as for self-inductance  $L$ , measured in henry (H) [22]. The mutual inductance of two perfectly magnetically coupled elements is given by

$$M = \sqrt{L_1 L_2}, \quad (2.7)$$

where  $L_1$  is the inductance in one element and  $L_2$  the inductance of the other [23].

For a resistor, the resistance  $R$  equals the peak to peak ratio of current to voltage since the signals are in phase with each other. The same peak to peak ratio is called reactance  $X$  for inductors and capacitors [22]. When the signals are sinusoidal, we find that the reactance of an inductor is

$$X_L = \omega L \quad (2.8)$$

and that the reactance of a capacitor is

$$X_C = \frac{1}{\omega C}. \quad (2.9)$$

Notably, the reactance is dependent on angular frequency  $\omega$  in addition to the inductance or capacitance.

The impedance  $Z$  of a component describes the instantaneous relationship between the voltage and current of that component,

$$Z = \frac{V}{I}, \quad (2.10)$$

where  $V$  and  $I$  are the complex voltage and current, respectively. Impedance is also a complex quantity, with magnitude equal to the resistance or reactance of a component



and angle corresponding to the phase shift between the current and voltage. In a resistor the current and voltage have the same phase, while in a capacitor the current leads the voltage by  $90^\circ$  and in an inductor the current lags the voltage by  $90^\circ$ . The impedances of a resistor, capacitor and inductor are thus given by

$$Z_R = R, \quad (2.11)$$

$$Z_C = -j \frac{1}{\omega C}, \quad (2.12)$$

$$Z_L = j\omega L, \quad (2.13)$$

respectively, where  $j$  is the imaginary unit [22]. An overview over the circuit symbols used in circuit diagram drawings in this thesis can be found in Appendix A.

The instantaneous power dissipation  $p$  in a component is equal to the product of instantaneous current  $i$  and instantaneous voltage  $v$ ,

$$p = vi. \quad (2.14)$$

Assuming the voltage and current to be sinusoidal with amplitudes  $V_p$  and  $I_p$ , and that the phase shift between them is  $\phi$  radians, the average power dissipation is

$$P = \frac{1}{2} V_p I_p \cos \phi. \quad (2.15)$$

We call  $P$  active power and measure it in watt (W). Alternatively, we can express the power in terms of root mean square (r.m.s.) values. For a sinusoidal current  $i = I_p \sin(\omega t + \phi)$ , the root mean square current is

$$I_{\text{rms}} = \left( \frac{\omega}{2\pi} \int_0^{2\pi/\omega} I_p^2 \sin^2(\omega t + \phi) dt \right)^{\frac{1}{2}} = \frac{I_p}{\sqrt{2}},$$

and in the same way

$$V_{\text{rms}} = \frac{V_p}{\sqrt{2}}.$$

Thus, the average power dissipation can also be expressed as

$$P = VI \cos \phi, \quad (2.16)$$

where  $V$  and  $I$  are r.m.s. values. The active power is positive in components that consume power and negative in components that deliver power. Reactive components store and return power to the circuit during each period of the signal, and this power is called reactive power  $Q$ . For sinusoidal signals it is given by

$$Q = \frac{1}{2} V_p I_p \sin \phi = VI \sin \phi, \quad (2.17)$$

and is measured in volt ampere reactive (var) to distinguish it from active power. Note that the reactive power is positive for inductive elements, since the voltage leads the current and therefore  $\phi$  is greater than zero, and negative for capacitive elements since the voltage lags the current.

For ease of calculations later, we will distinguish between apparent power  $S$  and total power  $\vec{S}$ . Apparent power is defined simply as

$$S = \frac{1}{2} V_p I_p = VI, \quad (2.18)$$

with units volt ampere (VA). Note that all three powers have the same dimension, the different units are merely used to distinguish the different forms of power. The relationship between active, reactive and apparent power is

$$S = \sqrt{P^2 + Q^2}.$$

Total power is a complex quantity defined as

$$\vec{S} = P + jQ,$$

such that  $S = |\vec{S}|$ . To find the correct apparent power of several components together, we add their total power and then take the absolute value instead of adding apparent power directly.

For a component with impedance  $Z = R \pm jX$ , we can find the active power as

$$P = \frac{1}{2}V_p I_p \cos \phi = \frac{1}{2}I_p^2 |Z| \cos \phi = \frac{1}{2}I_p^2 R = I^2 R \quad (2.19)$$

and the reactive power as

$$Q = \frac{1}{2}V_p I_p \sin \phi = \frac{1}{2}I_p^2 |Z| \sin \phi = \pm \frac{1}{2}I_p^2 X = \pm I^2 X. \quad (2.20)$$

The ratio of active to apparent power is called power factor,

$$\text{power factor} = \frac{P}{S} = \cos \phi, \quad (2.21)$$

where  $\phi$  as before is the phase angle between voltage and current. With the power definitions we have, the power factor will strictly speaking be negative when the component supplies active power such that  $P < 0$ . We will however take the power factor to be the absolute value, such that it always lies between 0 and 1, and just remember that a negative sign means that the component delivers active power instead of consuming it.

## 2.1 Transformers

Transformers are used to change the magnitude of AC signals, increasing the current and decreasing the voltage or vice versa, in the ideal case by the same factor. They work by using mutual inductance between two coils wound around the same core with a different number of windings. An ideal transformer is shown in Fig. 2.1. The two inductive elements represent the two coiled wires, and the fact that they are magnetically coupled through the common core is represented by the parallel lines. We call the side where we apply a voltage for the primary side, and the side where a voltage is induced for the secondary side. If there are  $N_1$  windings on the primary side and  $N_2$  windings on the secondary side, the relationship between the primary side voltage  $V_1$  and the secondary side voltage  $V_2$  is

$$\frac{V_1}{V_2} = \frac{N_1}{N_2}. \quad (2.22)$$

If the secondary side is on load, such that a current  $I_2$  is induced, the relationships between the currents will similarly be

$$\frac{I_1}{I_2} = \frac{N_2}{N_1}. \quad (2.23)$$

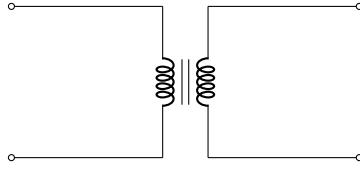


Figure 2.1: Circuit diagram of ideal an transformer.

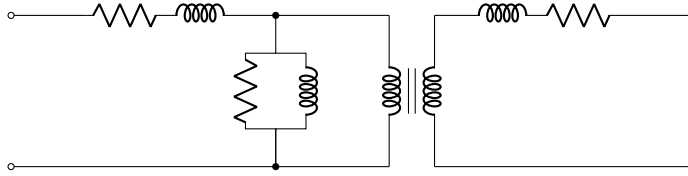


Figure 2.2: Circuit diagram of a non-ideal transformer.

In a real transformer there are several other effects that we need to take into account, and Eqs. (2.22) and (2.23) do not hold. These effects are magnetising current, core loss, winding resistance, and magnetic leakage flux [23]. Magnetising current and core loss can be represented as an inductor and a resistor, respectively, connected in parallel on one side of the ideal transformer. Winding resistance and magnetic leakage flux can be represented as a resistor and an inductor connected in series on each side. Figure 2.2 shows an equivalent circuit of such a transformer, redrawn after Hurley [23].

The values of the components making the transformer non-ideal will depend on the specific transformer, and the importance of each will also vary. Neglecting magnetizing current and core loss is usually a good approximation if the transformer is medium-sized or large [24]. We can make an equivalent circuit of this approximation where the winding resistances and magnetic leakage fluxes of both sides are represented by a single resistor and inductor located on either the primary or secondary side. Such a circuit is depicted in Fig. 2.3.

## 2.2 Three-phase systems

In industrial applications, power is often distributed through a three-phase system. As the name suggest, this means using three sources at once, each with a different phase. Three-phase circuits can be connected in either Y (wye) or  $\Delta$  (delta) connections, as shown in Figs. 2.4a and 2.4b, respectively [25]. The Y connection can also be called a star connection. If the phases of the three supplies differ by  $2\pi/3$  radians and the loads are equal, we call the system balanced. These conditions can never be met exactly, so all real systems are unbalanced to some degree. Using a three-phase system can deliver

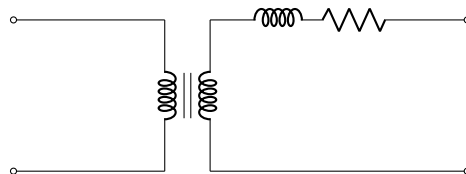


Figure 2.3: Circuit diagram of a non-ideal transformer approximation suitable for medium-sized and large transformers.

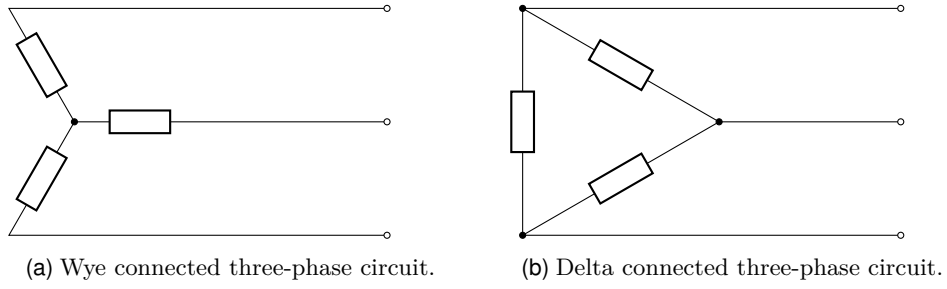


Figure 2.4: The two types of three-phase circuit connections.

the same amount of power as three separate single-phase systems, but with only half the number of conducting lines [25].

### 2.2.1 Symmetrical components

Symmetrical components are sometimes used to simplify calculations on three-phase systems. It is a decomposition of the three possibly unbalanced phasors into to three sets of three phasors, where two of the sets are balanced but have opposite rotation, and the third set have a common phase [26]. Symmetrical components can be used exactly the same way for both voltage and current phasors, and here we use voltages in our explanation.

Let the three voltage phasors in a three-phase system be represented by the complex numbers  $V_a$ ,  $V_b$  and  $V_c$  and let  $\alpha = e^{i2\pi/3}$ . The voltage phasors can then be decomposed as

$$\begin{bmatrix} V_a \\ V_b \\ V_c \end{bmatrix} = \begin{bmatrix} V_0 \\ V_0 \\ V_0 \end{bmatrix} + \begin{bmatrix} V_1 \\ V_1\alpha^2 \\ V_1\alpha \end{bmatrix} + \begin{bmatrix} V_2 \\ V_2\alpha \\ V_2\alpha^2 \end{bmatrix}, \quad (2.24)$$

where  $V_0$  is the common phasor (zero sequence),  $V_1$ ,  $V_1\alpha^2$ ,  $V_1\alpha$  is the set with positive rotation (positive sequence) and  $V_2$ ,  $V_2\alpha$ ,  $V_2\alpha^2$  is the set with negative rotation (negative sequence) [26]. Equation (2.24) can be written more compactly as

$$\mathbf{V}_{abc} = \mathbf{A}\mathbf{V}_{012}, \quad (2.25)$$

where

$$\mathbf{A} = \begin{bmatrix} 1 & 1 & 1 \\ 1 & \alpha^2 & \alpha \\ 1 & \alpha & \alpha^2 \end{bmatrix}, \quad \mathbf{V}_{abc} = \begin{bmatrix} V_a \\ V_b \\ V_c \end{bmatrix}, \quad \mathbf{V}_{012} = \begin{bmatrix} V_0 \\ V_1 \\ V_2 \end{bmatrix}.$$

We find the vector  $\mathbf{V}_{012}$  as

$$\mathbf{V}_{012} = \mathbf{A}^{-1}\mathbf{V}_{abc}, \quad (2.26)$$

where

$$\mathbf{A}^{-1} = \frac{1}{3} \begin{bmatrix} 1 & 1 & 1 \\ 1 & \alpha & \alpha^2 \\ 1 & \alpha^2 & \alpha \end{bmatrix} \quad (2.27)$$

is well defined. The exact same decomposition can be done with three-phase current.

The negative sequence to positive sequence ratio

$$\frac{V_2}{V_1} \quad (2.28)$$

is a much used standard for measuring voltage imbalance [27]. It assumes  $V_{abc}$  to be ordered so that it has a positive rotation, and has information about both the phase and absolute value of the imbalance. In a perfectly balanced system,  $V_0 = 0$  and  $V_2 = 0$ , in which case the ratio in Eq. (2.28) is zero. The further we are from zero, the more unbalanced the system is. If we have the opposite rotation of what we thought, Eq. (2.28) gives a number greater than one.

## 2.3 Power factor correction

Power factor correction is the procedure of installing reactive elements in a circuit to bring the power factor (2.21) closer to one [22]. This is useful because it allows for more efficient power use, as it means increasing the fraction of active power over apparent power, and because power companies charge industrial consumers for a poor power factor [22]. Power factor correction is thus both efficient and economically beneficial.

One can use capacitors for this purpose if the element causing the reduced power factor is inductive and vice versa, since the reactive effects of a capacitive and inductive element work towards cancelling each other out. Finding the element needed to bring the power factor to one is therefore a matter of calculating the reactive power of the circuit and adding an element which has the same absolute reactive power but opposite sign.

### 2.3.1 High-voltage compensation

Power factor correction is a standard procedure in submerged arc furnaces, especially since the power factor decreases with increasing furnace size [28]. In submerged arc furnaces the tradition is to place three capacitors in parallel on the primary side. This arrangement does not alter the power factor inside the furnace, but can bring the power factor as seen from the grid closer to one [28], [29]. We call this method high-voltage compensation (HVC) since the primary side is the high voltage side. Meintjes wrote in 1974 that capacitors “can theoretically be located on the secondary side [...], but the author knows of no practical application of this arrangement” [28, p. 149], and the situation is largely the same today. There are however some more recent attempts at placing the capacitors on the secondary side, which we will come back to later.



## Chapter 3

# Graph theory

We will use the framework of graph theory when solving linear circuit problems, specifically for finding currents and voltages in all parts of a circuit when we know the source voltages, the source currents, and the impedances of all components. We will first go through definitions and results from graph theory, and then explain how we use this framework to set up and solve matrix equations in a structured way.

The solution method we use is found in a book by Bermúdez *et al.* [30], but the method needs to be generalised for our use. We therefore need a more rigorous graph theory framework. In an attempt to provide the necessary rigour without delving too deep, we present graph theory definitions that are slightly adapted to our needs. This is all in the pursuit of being precise with the language and requirements for our solution method.

### 3.1 Definitions

There are slight differences in naming conventions and definitions between texts on graph theory, although the big picture is the same. We here provide definitions as given by Yadav [31] unless otherwise stated.

A simple graph  $\mathfrak{G}$ , from now on only called a graph, is a pair of finite sets  $(V, A)$  where  $A \subseteq V \times V$ . Or in other words, a graph consists of the elements in  $V$ , called nodes, and the elements in  $A$ , which are pairs of elements from  $V$  and are called edges. The edges are denoted  $r = \{a, b\}$ , where  $a, b \in V$ . As for any set, the order of the elements  $a$  and  $b$  do not matter.

In a simple directed graph, or digraph, edges additionally have a specified direction or orientation. They are sometimes called arcs, but we will stick to the name edges. Let  $r = (a, b) \in A$  be an edge of  $\mathfrak{G}$ . Then  $a$  is the tail and  $b$  is the head of  $r$ . Note that  $(a, b) \neq (b, a)$  for a digraph, since the ordering matters. When drawing digraphs we will use shaded discs for nodes and arrows for edges. An example is shown in Fig. 3.1. This graph has three nodes labelled 1, 2, and 3, an edge 1 going from node 1 to node 2, and an edge 2 going from node 1 to node 3. We will mostly be working with digraphs, but will give definitions for both graphs without a direction and for digraphs.

A path is a sequence of edges  $r_1, r_2, \dots, r_m$  for which there exists a sequence  $v_1, v_2, \dots, v_{m+1}$  of distinct nodes such that  $r_i = \{v_i, v_{i+1}\} \forall i \in \{1, \dots, m\}$ . If we do not require the sequence of nodes  $v_1, v_2, \dots, v_{m+1}$  to be distinct, we instead call the sequence of edges a trail. Two nodes  $a$  and  $b$  are connected if there exists a path between them or if  $a = b$ .

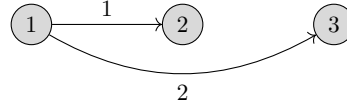


Figure 3.1: Example drawing of a directed graph with three nodes and two edges.

A directed path has the same definition, except that the sequence of edges  $r_1, r_2, \dots, r_m$  has a direction, that is  $r_i = (v_i, v_{i+1})$ . And similarly, if we do not require the sequence of nodes  $v_1, v_2, \dots, v_{m+1}$  to be distinct, we get a directed trail. There are several concepts or degrees of connectivity for digraphs, but for our purposes it is enough to know whether the nodes of the underlying non-directed graph are connected. We will therefore use the non-directed definitions of connectivity also for directed graphs.

We can partition the nodes of a graph into groups in such a way that all nodes within each group are connected, and no two nodes in different groups are connected. Each such group is called a connected component. It can be shown that connectivity is an equivalence relation with connected components as its equivalence class. A graph  $\mathfrak{G}$  is called connected if it only has one connected component, or equivalently if all pairs of nodes in the graph are connected. We will use this same definition of connected components for digraphs.

Consider the graph  $\mathfrak{G} = (V, A)$ . A graph  $\mathfrak{G}' = (V', A')$  is a subgraph of  $\mathfrak{G}$  if and only if  $V' \subseteq V$ ,  $A' \subseteq A$  and  $A' \subseteq V' \times V'$ . An equivalent definition applies to directed graphs.

Given a graph  $\mathfrak{G}$  with a trail  $r_1, r_2, \dots, r_n$  and a corresponding sequence of nodes  $v_1, v_2, \dots, v_n, v_1$ , where  $v_1$  is the only repeating node, meaning that this trail starts and ends at the same node. Then the subgraph  $\mathfrak{G}$  induced by this trail is called a cycle of  $\mathfrak{G}$ . If the graph and trail are directed, the resulting subgraph is a directed cycle. Note that a digraph may have no directed cycles, but the underlying non-directed graph can still have one or more cycles.

A tree is a connected graph  $\mathfrak{G}$  with no cycles. A graph where all its connected components are trees is called a forest. Thus, a forest with one connected component is also a tree. A spanning tree  $\mathfrak{T}$  is a subgraph of a connected graph  $\mathfrak{G}$  that contains all nodes of  $\mathfrak{G}$  and no cycles. That is,  $\mathfrak{T}$  is a tree that contains the same nodes as  $\mathfrak{G}$ . In extension of this concept, we also define a spanning forest  $\mathfrak{F}$  as a subgraph consisting of one spanning tree from each connected component.

For a directed tree and a directed spanning tree, we will differ from Yadav [31] and define it as a tree and spanning tree of the underlying non-directed graph, but with edges given the same orientation as the corresponding edges of the digraph. In accordance with Bermúdez *et al.* [30], we will call the edges of a spanning tree branches, and the edges of the graph not belonging to the spanning tree we call bonds or chords. The bonds make up what we call the co-tree of the graph.

The incidence matrix, as defined in [30], is a way of representing a digraph as a matrix. Given a directed graph  $\mathfrak{G}$  with  $N$  nodes and  $E$  edges, the incidence matrix  $\mathcal{A}$  of  $\mathfrak{G}$  is an  $N \times E$  matrix with elements

$$a_{ij} = \begin{cases} -1, & \text{if node } i \text{ is the tail node of edge } j \\ 1, & \text{if node } i \text{ is the head node of edge } j \\ 0, & \text{otherwise.} \end{cases} \quad (3.1)$$

Note that all  $E$  columns contain exactly one 1, one  $-1$  and otherwise zeros, which means that the sum of all the rows is a zero vector and thus the rows are linearly dependent.



We will also need the concept of a cycle matrix as defined in [30]. Given a digraph  $\mathfrak{G}$  with  $N$  nodes and  $E$  edges, where the underlying non-directed graph has  $L$  cycles. We give each cycle an arbitrary orientation, such that the edges belonging to the cycle may have the same or opposing direction to the cycle itself. The cycle matrix  $\mathcal{B}$  of size  $E \times L$  is then defined as

$$b_{jl} = \begin{cases} -1, & \text{if edge } j \text{ belongs to cycle } l \text{ with opposing directions} \\ 1, & \text{if edge } j \text{ belongs to cycle } l \text{ with the same direction} \\ 0, & \text{otherwise.} \end{cases} \quad (3.2)$$

## 3.2 Results for digraphs

We here state results and theorems from graph theory that will be used further on.

For a digraph  $\mathfrak{G}$  with  $N$  nodes and  $M$  connected components it holds that

$$\text{rank}(\mathcal{A}) = N - M, \quad (3.3)$$

where  $\mathcal{A}$  is the incidence matrix of  $\mathfrak{G}$  [30]. Thus  $\mathcal{A}$  has exactly  $N - M$  linearly independent columns.

If  $\mathfrak{G}$  is a connected digraph with  $N$  nodes and  $E$  edges, any selection of  $N - 1$  columns from the incidence matrix are linearly independent if and only if they constitute the edges of a directed spanning tree  $\mathfrak{T}$ . The remaining  $E - 1 + N$  columns correspond to the edges of its co-tree [30]. This result can be generalized to a graph with  $M$  connected components. Then, any selection of  $N - M$  columns from the incidence matrix are linearly independent if and only if they constitute the edges of a directed spanning forest  $\mathfrak{F}$ .

For a connected digraph  $\mathfrak{G}$  with  $N$  nodes and  $E$  edges, we have

$$\text{rank}(\mathcal{B}) = E - N + 1$$

for the cycle matrix  $\mathcal{B}$  defined in Eq. (3.2) [30]. This result can be generalized to

$$\text{rank}(\mathcal{B}) = E - N + M \quad (3.4)$$

if the digraph instead has  $M$  connected components. Consider a digraph  $\mathfrak{G}$  with  $N$  nodes,  $E$  edges and  $M$  connected components. It can be shown that

$$\mathcal{A}\mathcal{B} = 0 \quad (3.5)$$

for any incidence matrix and its corresponding cycle matrix [30], meaning that the columns of  $\mathcal{B}$  belong to the kernel of  $\mathcal{A}$ . From Eq. (3.3) and the fact that  $\mathcal{A}$  has  $E$  columns, the rank-nullity theorem from linear algebra tells us that the nullity of  $\mathcal{A}$  is  $E - N + M$ . Combined with Eq. (3.4) this gives us

$$\text{nullity}(\mathcal{A}) = \text{rank}(\mathcal{B}). \quad (3.6)$$

Let  $\mathfrak{G}$  be a digraph with  $N$  nodes,  $E$  edges and  $M$  connected components, and  $\mathfrak{F}$  be a directed spanning forest.  $\mathfrak{F}$  has  $N - M$  edges, and adding any one of the  $E - N + M$  remaining edges will result in a cycle for the underlying non-directed graph. We call such a cycle a fundamental cycle. A submatrix of the cycle matrix as defined in Eq. (3.2) consisting of the columns corresponding to these fundamental cycles is called a matrix of fundamental cycles. These  $E - N + M$  columns are linearly independent, and the matrix of fundamental cycles is therefore a basis for  $\mathcal{B}$ .

### 3.3 Finding a basis of $\ker(\mathcal{A})$

We will need a way to find a basis of the kernel of the incidence matrix  $\mathcal{A}$  when we use graph theory to solve circuit problems. We here describe a generalisation of the solution method outlined by Bermúdez *et al.* [30]. Bermúdez *et al.* assumes the graph to be connected, but we will look at the general case.

Equations (3.5) and (3.6) together tell us that

$$\ker(\mathcal{A}) = \text{im}(\mathcal{B}),$$

and therefore a basis of  $\mathcal{B}$  will also be a basis of  $\ker(\mathcal{A})$ . This basis is a matrix of fundamental cycles, which we will denote as  $\mathcal{B}_F$ . It remains to find  $\mathcal{B}_F$ .

For the digraph  $\mathfrak{G}$  with a corresponding directed spanning forest  $\mathfrak{F}$ , we can without loss of generality assume that the edges of the graph are numbered such that the edges contained in the spanning forest come first. We define the reduced incidence matrix  $\mathcal{A}_R$  as any submatrix of  $\mathcal{A}$  with  $N - M$  rows, where it holds that the  $M$  removed rows correspond to nodes from different trees of the forest.  $\mathcal{A}_R$  can then be decomposed as

$$\mathcal{A}_R = [\mathcal{A}_T \mathcal{A}_C],$$

where  $\mathcal{A}_T$  is an  $(N - M) \times (N - M)$  matrix with columns corresponding to the edges of the spanning forest, and  $\mathcal{A}_C$  is an  $(N - M) \times (E - N + M)$  matrix with columns corresponding to the edges of the co-trees of the connected components. The matrix  $\mathcal{B}_F$  can be decomposed as

$$\mathcal{B}_F = \begin{bmatrix} \mathcal{B}_T \\ \mathcal{I} \end{bmatrix},$$

where  $\mathcal{I}$  is the identity matrix of size  $(E - N + M) \times (E - N + M)$  and  $\mathcal{B}_T$  is a matrix of size  $(N - M) \times (E - N + M)$  [30]. From Eq. (3.5) we get that

$$0 = \mathcal{A}_R \mathcal{B}_F = \mathcal{A}_T \mathcal{B}_T + \mathcal{A}_C,$$

and solving for  $\mathcal{B}_T$  we get

$$\mathcal{B}_T = -\mathcal{A}_T^{-1} \mathcal{A}_C. \quad (3.7)$$

The above expression is always well defined, since  $\mathcal{A}_T$  is a square matrix of full rank.

## 3.4 Solving circuit problems with graph theory

### 3.4.1 General case

The solution method presented here can be found in [30]. We start by modelling the circuit of interest as a directed graph where edges correspond to the electrical components and nodes correspond to the junctions between them. The direction of the edges are chosen arbitrarily. Let  $\mathcal{A}$  be the incidence matrix of this graph as defined in Eq. (3.1), of size  $N \times E$  and with elements denoted by  $a_{ij}$ .

We denote the current along edge  $j$  at time  $t$  by  $I_j(t)$ ,  $j = 1, 2, \dots, E$  and let  $\Psi_i(t)$ ,  $i = 1, 2, \dots, N$  be an external current source entering at node  $i$ . Kirchhoff's current law (2.1) can then be rewritten as

$$\sum_{j=1}^E a_{ij} I_j(t) = -\Psi_i(t) \quad (3.8)$$

for each node  $i = 1, 2, \dots, N$ .

The voltage at node  $i$  and time  $t$  is denoted by  $V_i(t)$ ,  $i = 1, 2, \dots, N$ . We can then write the potential drop over the electrical components, which corresponds to the potential difference between the two nodes of an edge, as follows. Let the nodes  $m_{1j}$  and  $m_{2j}$  be the head and tail, respectively, of edge  $j$ . If edge  $j$  is a resistor with resistance  $R_j$ , Eq. (2.3) can be rewritten as

$$V_{m_{1j}}(t) - V_{m_{2j}}(t) = R_j I_j(t). \quad (3.9)$$

If edge  $j$  is a capacitor with capacitance  $C_j$ , Eq. (2.5) can be rewritten as

$$V_{m_{1j}}(t) - V_{m_{2j}}(t) = \frac{1}{C_j} \left( Q_j(0) + \int_0^t I_j(s) ds \right), \quad (3.10)$$

where  $Q_j(0)$  is the initial charge stored in the capacitor. If edge  $j$  is an inductor with inductance  $L_j$ , Eq. (2.4) can be rewritten as

$$V_{m_{1j}}(t) - V_{m_{2j}}(t) = L_j \frac{dI_j}{dt}(t). \quad (3.11)$$

If the edges  $l_1, l_2, \dots, l_S$  are magnetically coupled, we define the inductance matrix  $\mathcal{L}^S$  as the matrix with the self-inductance of the edges on the diagonal and the mutual inductance of the edges on the off-diagonals, that is

$$\begin{aligned} \ell_{ii} &= L_i, \\ \ell_{ij} &= M_{ij}. \end{aligned}$$

$M_{ij} = M_{ji}$  and the matrix  $\mathcal{L}^S$  is symmetric positive definite. This leads to the matrix equation

$$\mathcal{L}^S \frac{d\vec{I}_S}{dt}(t) = \Delta \vec{V}_S(t), \quad (3.12)$$

where

$$\begin{aligned} \vec{I}_S(t) &= (I_{l_1}(t), I_{l_2}(t), \dots, I_{l_S}(t))^T, \\ \Delta \vec{V}_S(t) &= (V_{m_{1l_1}}(t) - V_{m_{2l_1}}(t), \dots, V_{m_{1l_S}}(t) - V_{m_{2l_S}}(t))^T, \end{aligned}$$

are the vectors with the currents through and voltages over the edges. If no edges are magnetically coupled, Eq. (3.12) reduces to Eq. (3.11).

We now define the vectors

$$\begin{aligned} \vec{I}(t) &= (I_1(t), I_2(t), \dots, I_E(t))^T, \\ \vec{V}(t) &= (V_1(t), V_2(t), \dots, V_N(t))^T, \\ \vec{E}(t) &= (E_1(t), E_2(t), \dots, E_E(t))^T, \\ \vec{\Psi}(t) &= (\Psi_1(t), \Psi_2(t), \dots, \Psi_N(t))^T, \end{aligned}$$

of currents, voltages, source voltages and source currents, respectively. Define also a linear operator  $\mathcal{D}$  working on the vector  $\vec{I}(t)$  by

$$\mathcal{D}(\vec{I})_j(t) = \begin{cases} R_j I_j(t), & \text{if edge } j \text{ is a resistor} \\ \frac{1}{C_j} \left( Q_j(0) + \int_0^t I_j(s) ds \right), & \text{if edge } j \text{ is a capacitor} \\ L_j \frac{dI_j}{dt}(t), & \text{if edge } j \text{ is an inductor} \\ r_j I_j(t), & \text{if edge } j \text{ is a power source} \end{cases} \quad (3.13)$$

and

$$\mathcal{D}(\vec{I})_S(t) = \mathcal{L}^S \frac{d\vec{I}_S}{dt}(t), \quad (3.14)$$

where  $\mathcal{D}(\vec{I})_S = (\mathcal{D}(\vec{I})_{l_1}, \mathcal{D}(\vec{I})_{l_2}, \dots, \mathcal{D}(\vec{I})_{l_S})^T$ . We then write the circuit problem where the source currents  $\vec{\Psi}(t)$  and source voltages  $\vec{E}(t)$  are known and we wish to find the currents  $\vec{I}(t)$  and potentials  $\vec{V}(t)$  as

$$\mathcal{D}(\vec{I})(t) + \mathcal{A}^T \vec{V}(t) = \vec{E}(t), \quad (3.15)$$

$$\mathcal{A} \vec{I}(t) = -\vec{\Psi}(t). \quad (3.16)$$

If we solve Eqs. (3.15) and (3.16), we have solved the circuit problem. This system consists of  $E + N$  equations, and we have  $E + N$  unknowns. However, the equations are linearly dependent because of the non-trivial relationship between the currents  $\vec{I}(t)$  and potentials  $\vec{V}(t)$ . It is therefore possible to find a smaller and linearly independent system of equations.

Assuming that the graph corresponding to the circuit has  $M$  connected components, the rank of the incidence matrix  $\mathcal{A}$  is  $N - M$  and hence

$$\dim \ker(\mathcal{A}) = E - N + M.$$

We can then find a basis  $\{\mathbf{u}_1, \mathbf{u}_2, \dots, \mathbf{u}_{E-N+M}\}$  of  $\ker(\mathcal{A})$  as described in Sec. 3.3, with the property

$$\mathbf{u}_k^T \mathcal{A}^T = \mathbf{0} \quad \forall k = 1, 2, \dots, E - N + M.$$

Multiplying Eq. (3.15) with  $\mathbf{u}_k^T$  from the left thus results in the equations

$$\mathbf{u}_k^T \mathcal{D}(\vec{I})(t) = \mathbf{u}_k^T \vec{E}(t) \quad \forall k = 1, 2, \dots, E - N + M.$$

Define the  $E \times (E - N + M)$  matrix  $\mathbf{U}$  as

$$\mathbf{U} = (\mathbf{u}_1, \mathbf{u}_2, \dots, \mathbf{u}_{E-N+M}).$$

A new set of equations for the circuit problem is then

$$\mathbf{U}^T \mathcal{D}(\vec{I})(t) = \mathbf{U}^T \vec{E}(t), \quad (3.17)$$

together with  $N - M$  linearly independent equations from (3.16). This is a set of exactly  $E$  equations where the unknowns are the  $E$  currents  $\vec{I}(t)$ . And once the currents are known, we can easily find the potentials  $\vec{V}(t)$ .

This method works for source voltages and source currents of any form, and can handle both single phase and three-phase circuits, transient and stationary behaviour equally well in theory. But in practice it might require a numerical scheme since the equations involve both integrals and derivatives. Bermúdez *et al.* proposes a general numerical method using discretised time series, the backward formula as an approximation to the derivative, and the composed trapezoidal rule as an approximation to the integral.

### 3.4.2 Harmonic problems

The circuit problem where all source voltages and source currents are harmonic functions is simpler, as we can evaluate the required integrals and derivatives exactly and reduce

the problem to a system of linear algebraic equations. This section also follows the methods of [30].

When the source voltages and currents are harmonic functions of time and we work with linear circuits, all potentials and current intensities in the circuit will also be harmonic functions. We therefore define

$$\vec{I}(t) = \text{Re} \left( \tilde{\mathbb{I}} e^{i\omega t} \right), \quad (3.18)$$

$$\vec{V}(t) = \text{Re} \left( \tilde{\mathbb{V}} e^{i\omega t} \right), \quad (3.19)$$

$$\vec{E}(t) = \text{Re} \left( \tilde{\mathbb{E}} e^{i\omega t} \right), \quad (3.20)$$

$$\vec{\Psi}(t) = \text{Re} \left( \tilde{\Psi} e^{i\omega t} \right), \quad (3.21)$$

where  $\tilde{\mathbb{I}}$ ,  $\tilde{\mathbb{V}}$ ,  $\tilde{\mathbb{E}}$  and  $\tilde{\Psi}$  are complex vectors, with the so-called complex amplitudes of their respective quantities. We here use  $i$  to denote the imaginary unit. For a general complex vector  $\mathbb{A} e^{i\omega t}$  we have

$$\frac{d}{dt} \mathbb{A} e^{i\omega t} = i\omega \mathbb{A} e^{i\omega t}$$

and

$$\int \mathbb{A} e^{i\omega t} dt = \frac{1}{i\omega} \mathbb{A} e^{i\omega t}.$$

From this we can see that we can substitute the operator  $\mathcal{D}$  working on  $(\vec{I})(t)$  as defined in Eqs. (3.13) and (3.14) by a product  $\mathcal{D}(\omega) \tilde{\mathbb{I}} e^{i\omega t}$ , where  $\mathcal{D}(\omega)$  is a matrix defined by

$$\mathcal{D}(\omega)_{jj} = \begin{cases} R_j, & \text{if edge } j \text{ is a resistor} \\ -\frac{i}{\omega C_j}, & \text{if edge } j \text{ is a capacitor} \\ i\omega L_j, & \text{if edge } j \text{ is an inductor} \end{cases} \quad (3.22)$$

and

$$\mathcal{D}(\omega)_S = i\omega \mathcal{L}^S, \quad (3.23)$$

where  $\mathcal{L}^S$  is the inductance matrix as before.  $\mathcal{D}(\omega)$  is called the impedance matrix, as its diagonal elements equal the impedances in Eqs. (2.11), (2.12) and (2.13). The system of equations (3.15) and (3.16) can then be written as

$$\begin{aligned} \mathcal{D}(\omega) \tilde{\mathbb{I}} e^{i\omega t} + \mathcal{A}^T \tilde{\mathbb{V}} e^{i\omega t} &= \tilde{\mathbb{E}} e^{i\omega t}, \\ \mathcal{A} \tilde{\mathbb{I}} e^{i\omega t} &= -\tilde{\Psi} e^{i\omega t}, \end{aligned}$$

which simplifies to the time-independent system of equations

$$\mathcal{D}(\omega) \tilde{\mathbb{I}} + \mathcal{A}^T \tilde{\mathbb{V}} = \tilde{\mathbb{E}}, \quad (3.24)$$

$$\mathcal{A} \tilde{\mathbb{I}} = -\tilde{\Psi}. \quad (3.25)$$

Equations (3.24) and (3.25) are algebraic and therefore easily solvable if a solution exists. We can however reduce the number of equations by the same method as described in the general case. Let  $\mathbf{U}$  be a matrix with columns that form a basis of  $\ker(\mathcal{A})$ . Then

$$\mathbf{U}^T \mathcal{D}(\omega) \tilde{\mathbb{I}} = \mathbf{U}^T \tilde{\mathbb{E}} \quad (3.26)$$

together with  $N - M$  linearly independent equations from (3.25) constitute a system of  $E$  equations for the  $E$  unknowns  $\tilde{\mathbb{I}}$ .  $\tilde{\mathbb{V}}$  can then be found from (3.24) as the solution of

$$\mathcal{A}^T \tilde{\mathbb{V}} = \tilde{\mathbb{E}} - \mathcal{D}(\omega) \tilde{\mathbb{I}}, \quad (3.27)$$

and we extract the real, time-dependent solutions  $\vec{I}(t)$  and  $\vec{V}(t)$  according to Eqs. (3.18) and (3.19).



## Chapter 4

# Circuit models and other furnace theory

The goal of this thesis is to develop and use equivalent circuit models to study the furnace and supply system. In this chapter we present the circuit models and introduce some other needed concepts, namely a previously developed metamodel, furnace control, and how to make measurements of a furnace.

### 4.1 Circuit models

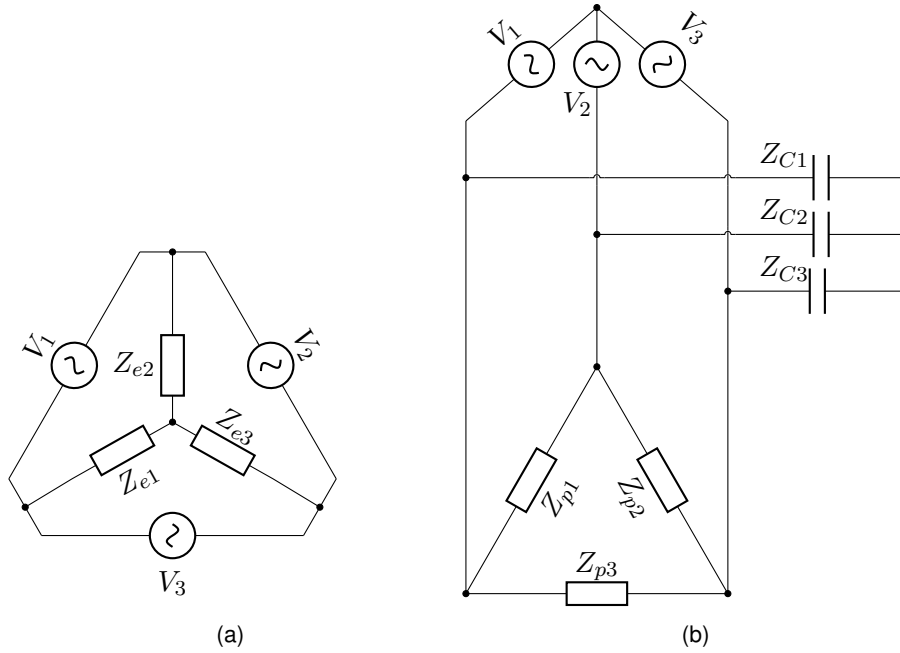
We here define circuit equivalent models of a submerged arc furnace that we will use for our further analyses. We first define models for the primary and secondary sides separately, and then combine them into one model for the entire system.

For all the models, we will need the impedance of the different elements. We know the voltage input from the grid and the capacitance on the primary side. The conducting lines are set to have non-zero, but negligibly small resistance. For the transformers we do not know the inductance of either side, the mutual inductance, or the resistance of the coils. Here we must resort to crude approximations, which we will do in Sec. 6.3.1. We can measure the electrode current and voltage as described in Sec. 4.5, and we can therefore calculate the electrode impedance.

#### 4.1.1 Secondary side

We begin by modelling the secondary side circuit, that is the secondary side of the transformers and the furnace itself. Valderhaug [4] presents a detailed equivalent circuit of a submerged arc furnace for ferrosilicon in chapter 4.3.1 of his thesis and Figure 4.5 of that chapter. Even though the values assigned to elements of this circuit will be different for different alloy furnaces, the structure is the same. The circuit model shows the different paths the currents can follow and models the different internal parts of the furnace with their own separated impedances. By assuming the electrode to electrode current to be negligible and lumping together some impedances, we can simplify the model somewhat. It is however still complicated enough that Valderhaug assumes symmetric conditions before proceeding with analytic studies.

We make the model even simpler by not modelling the arc and ohmic conduction between the electrodes and charge material separately. This is a possibly huge simplification, given that the arc is a non-linear element [29]. We also assume that the electrodes are not mutually inductive, although in reality they are [4]. With these



**Figure 4.1:** Circuit diagrams of (a) the secondary side equivalent circuit and (b) the primary side equivalent circuit.

assumptions, we get the circuit diagram shown in Fig. 4.1a, which is the same equivalent circuit as the one used by Barker *et al.* [32]. The transformers are modelled as sinusoidal voltage sources with non-zero internal impedance, and the impedance of the bus bars and flexible conductors are lumped together with this internal impedance. The electrodes are modelled as elements with both resistive and inductive components and connected in a wye through the metal bath.

#### 4.1.2 Primary side

The primary side consists of the grid connection, capacitors for power factor correction and the primary side of the transformers, and we therefore do not need to make as many simplifications and assumptions. In order to impose a constant potential at the nodes connecting the grid to our circuit, we model the supply as three sinusoidal voltage sources that are connected in a wye on the grid side. We look at the primary side transformers as highly inductive and resistive elements that are connected in a delta and model the capacitors as ideal. Figure 4.1b shows the circuit diagram of the primary side. The conducting lines connecting the grid and capacitors to the delta are given a negligible non-zero resistance which is not explicitly drawn.

#### 4.1.3 Full equivalent circuit

Combining the primary and secondary side models described above gives us a model of the full system. We do that by substituting the primary side impedances and secondary side voltage sources with transformer equivalent circuits like the one in Fig. 2.3, thus connecting the two sides. Figure 4.2 shows the resulting circuit diagram. In this figure we have lumped the resistor and inductor of the non-ideal transformer into one impedance element to simplify the drawing.



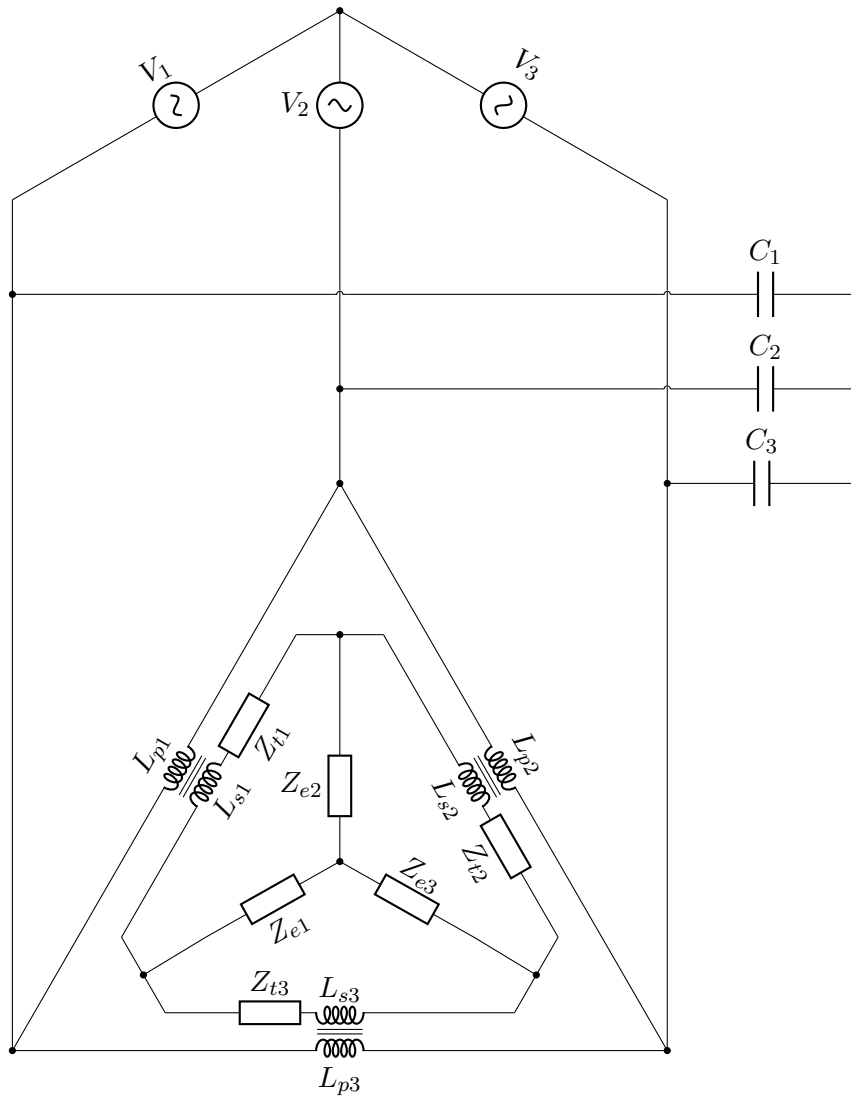


Figure 4.2: Circuit diagram of the full system, with the primary and secondary sides connected through non-ideal transformers.

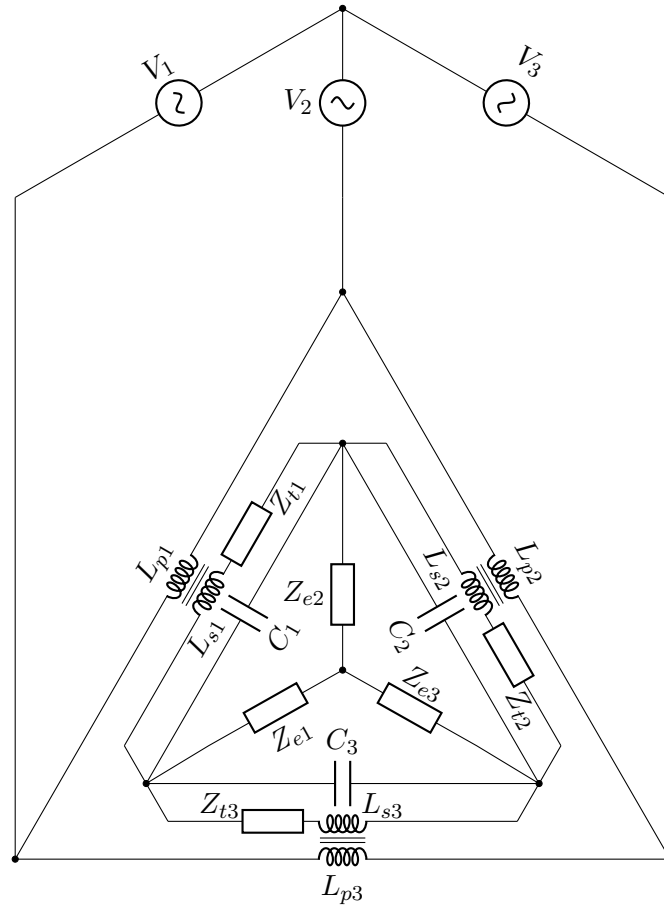


Figure 4.3: Circuit diagram of the full system with low-voltage compensation.

#### 4.1.4 Low-voltage compensation

An alternative to high-voltage compensation as described in Sec. 2.3.1 is placing the capacitors on the secondary side, between the transformers and the furnace itself [33]. We call this low-voltage compensation (LVC), as the capacitors are placed on the low-voltage side. This is a far less established way of doing power factor correction, reported to be “not practical” [29, p. 153] and only recently being introduced as a serious option [33]. Figure 4.3 shows the setup as it looks in our simplified model, where the capacitors are connected in parallel with the secondary side of the transformers. According to Li *et al.* [33], low-voltage compensation has the advantage of making it possible to improve the power factor of the transformer, whereas primary side capacitors do not affect the transformers or secondary side at all [28].

## 4.2 Defining circulating currents

There can exist circulating currents in the delta connection on both the primary and secondary sides. Sævarsdóttir *et al.* [34] estimated the circulating current in the secondary side delta due to skew tapping, a situation in which the three transformers operate at different tap positions and thus have different secondary side voltages. They did this by estimating the voltage difference due to skew tapping and the impedance of the components, and found a circulating current of 3.45 kA. We can use equivalent

circuit models to calculate circulating current, but we need to define it first.

### 4.2.1 Secondary side

We want all the current being supplied to the secondary side to enter the electrodes and thus contribute to heating the furnace, but this will in general not be the case. There might be a circulating current going around in the delta connection and not entering the electrodes. Denote the electrode currents  $I_1$ ,  $I_2$ , and  $I_3$  and the transformer currents  $I_4$ ,  $I_5$ , and  $I_6$ . We find an expression for the circulating current by decomposing the transformer currents into the circulating current  $I_c$  and another part  $\Delta I_x$ ,  $x = 4, 5, 6$ , such that

$$\begin{aligned} I_4 &= I_c + \Delta I_4 \\ I_5 &= I_c + \Delta I_5 \\ I_6 &= I_c + \Delta I_6. \end{aligned}$$

The currents going down into the electrodes are then

$$\begin{aligned} I_1 &= \Delta I_6 - \Delta I_4 \\ I_2 &= \Delta I_4 - \Delta I_5 \\ I_3 &= \Delta I_5 - \Delta I_6. \end{aligned}$$

We see that they are independent of  $I_c$ , and  $I_c$  is therefore truly a circulating current. If we require  $\Delta I_4 + \Delta I_5 + \Delta I_6 = 0$ , as would be the case for a balanced system with zero circulating current, the circulating current is given by

$$I_c = \frac{1}{3} (I_4 + I_5 + I_6). \quad (4.1)$$

### 4.2.2 Primary side

There can similarly exist a circulating current in the delta connection of the transformers on the primary side. Let the current in the conducting lines be denoted  $I_4$ ,  $I_5$ , and  $I_6$  and the transformer currents be denoted  $I_{10}$ ,  $I_{11}$ , and  $I_{12}$ . We follow the same procedure as for the secondary side, defining transformer currents as deviation from circulating current  $I_c$ ,

$$\begin{aligned} I_{10} &= I_c + \Delta I_{10} \\ I_{11} &= I_c + \Delta I_{11} \\ I_{12} &= I_c + \Delta I_{12}. \end{aligned}$$

The current entering the transformer delta connection can then be expressed as

$$\begin{aligned} I_4 &= \Delta I_{11} - \Delta I_{10} \\ I_5 &= \Delta I_{10} - \Delta I_{12} \\ I_6 &= \Delta I_{12} - \Delta I_{10}, \end{aligned}$$

which is independent of  $I_c$ . If we require  $\Delta I_{10} + \Delta I_{11} + \Delta I_{12} = 0$ , the circulating current is given by

$$I_c = \frac{1}{3} (I_{10} + I_{11} + I_{12}). \quad (4.2)$$

### 4.3 A furnace metamodel

As mentioned earlier, there are several well-developed physics-based models of submerged arc furnaces. However, one major drawback of physics-based models is the computational cost [35]. These models are therefore not fit for real time simulations like control operations, or for running a large number of test cases in a short amount of time. A metamodel of one such physics-based has therefore been developed by Sparta *et al.* [35]. A metamodel is here defined as “an approximation of an original physics-based model obtained by applying a suitable statistical analyses on a database generated with the original model” [35, p. 1268].

The metamodel is based on a physics-informed Finite Element Method (FEM) model. Sparta *et al.* generated a database of inputs and outputs with due consideration of spanning the relevant input space as well as possible. Then they developed a statistical model based on this database using partial least squares regression. The resulting metamodel is computationally fast, and retains the general behaviour of the original FEM model. Input parameters are electrode currents, furnace geometry descriptors and conductivity of coke beds and charge. Outputs include electrode resistance and reactance, and active and reactive power in different parts of the furnace.

A web-based simulator for the metamodel described above is openly available [36], [37], for both a ferromanganese [35] and a ferrosilicon [37] furnace. While this metamodel is static in nature, a sort of dynamic simulator has been made by generating input time series and successively solving the static model with changing input. For this thesis we have access to the Python source code for the ferromanganese model, which is the most updated version, so that we can build upon and make slight alterations to the functionality as needed. We can use the metamodel to for example find estimates of realistic parameters that are not readily available otherwise, study the effects of moving electrodes and run simulations.

### 4.4 Electrical furnace control

We will distinguish between process control and process optimisation. Process control refers to how we keep the furnace conditions stable under operation, whereas process optimisation is about finding the optimal working point. Controlling the electrical environment of the furnace is essential to keep it working optimally [38], and we here present some strategies for doing so.

The electrical control consists of power controllers and electrode controllers. Power controllers work by changing the transformer tap positions and thus adjusting the windings ratio of the transformers, and electrode controllers work by adjusting the electrode displacement in order to control either the electrode current or the electrode resistance [2], [4]. We will be focusing on electrode control.

Electrode current control normally works as three monovariable controllers, and tries to control the current in each electrode separately by lowering or lifting that electrode. This comes with the problem of interaction, as moving one electrode causes the currents in the other two to change as well [39], but it is possible to design a so-called decoupled controller that is non-interacting [4]. The other option is three monovariable controllers that move the electrodes separately to control the resistance. In theory resistance control does not cause interaction [39]. However, the resistance calculation is based on voltage measurements that could be unreliable or difficult to maintain. The current is in contrast easy to measure accurately [4].

Current and resistance control can have a structurally similar dead-zone control algorithm. We choose a current or resistance reference value that we aim for and a width for the co-called dead-zone around this reference value. The control system then works to keep the current or resistance within this dead-zone, by moving the electrode a fixed length after it has been outside of the dead-zone for a chosen length of time [4]. This waiting time is called the time-before-action period and is used to avoid moving the electrodes in response to fluctuations which correct themselves. The choice of parameter values for the reference value, width of the dead-zone and time-before-action will influence the performance of the control algorithm.

## 4.5 Measurement strategies

In order to operate a furnace optimally, we need to know the power consumption of the electrodes [40], and for this we need measurements of electrode current and voltage. For comparison with numerical models, we will also use measurements of transformer voltages and currents. Transformer voltages are measured directly by a voltmeter, but the other measurements are more complicated. Electrode currents are measured from the primary side, for the secondary side transformer currents we can use Rogowski coils, and electrode voltages are measured with a technique called the Bøckman method.

### 4.5.1 Electrode currents

Electrode currents are measured with a standard and reliable setup on the primary side [29]. It uses the principle of Eq. (2.23), that the primary and secondary currents are proportional with the windings ratio as proportionality constant. The measurement equipment is connected to the primary side through a set of transformers that can compensate for tap changes in the main transformers in case those are unbalanced. The connection is a delta-wye, mirroring the transformer and electrode connections on the secondary side [2]. This way, the measured currents are directly proportional to the electrode currents.

### 4.5.2 Rogowski coils

Rogowski coils measure AC currents based on Ampere's and Faradays' laws [41]. A schematic drawing of a Rogowski coil is shown in Fig. 4.4. The Rogowski coil itself is the coil wrapped around the conductor we wish to measure the current in. The changing current  $i(t)$  in the conductor will then induce a voltage  $v(t)$  in the Rogowski coil. The measured voltage in the coil is therefore proportional to the derivative of the current in the conductor,

$$v(t) = \frac{A}{s} \mu_0 \frac{di}{dt'} \Big|_{t'=t}, \quad (4.3)$$

where  $v(t)$  is the measured voltage,  $A$  is the cross-section area of the windings,  $s$  is the number of windings per unit length,  $\mu_0$  is the magnetic permeability of vacuum, and  $\frac{di}{dt'}$  is the derivative of the current [41]. Integrating this voltage signal we can thus find the current in the conductor. The circuit connected to the Rogowski coil in Fig. 4.4 is an integrator circuit designed to do that.

Rogowski coils are advantageous because of their flexibility, relatively low cost, good transient response, and ability to measure a wide range of currents with large variations in frequency [41].

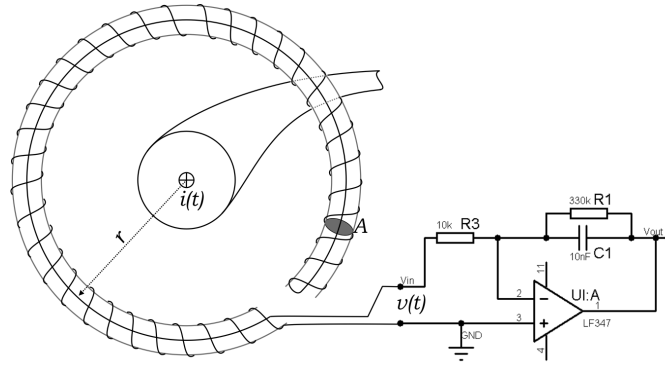
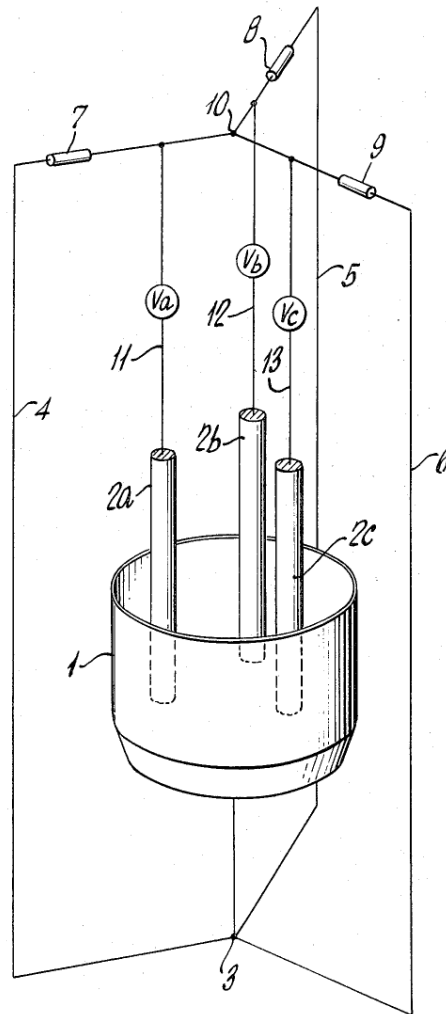


Figure 4.4: Schematic drawing of a Rogowski coil setup [42]. The left part of the figure shows the Rogowski coil itself wrapped around the conducting line. The circuit to the right is the so-called integrator circuit.

### 4.5.3 The Bøckman method

Measuring the voltage between the electrodes and the furnace bottom is difficult. Simply connecting a point of the furnace bottom to a conductor to get the potential in the furnace bottom will result in potentially large errors, as there will be non-negligible induced voltages in any such conductor due to the strong magnetic fields present [2]. To remedy this we can use the so-called Bøckman method [43], [44].

Figure 4.5 shows a schematic drawing of the measurement configuration in the Bøckman method. Instead of using a single conductor, we connect three conducting lines to the furnace bottom. These lines are numbered 4, 5, and 6 in the drawing. The conducting lines are placed symmetrically around the furnace, led to a point above the furnace with weak magnetic fields, and connected through three equal resistances numbered 7, 8, and 9 in a wye connection, numbered 10 on the drawing. The idea is that in the perfectly balanced case and with this symmetric arrangement, the induced voltages will cancel each other out as they have the same magnitude and are  $2\pi/3$  radians shifted with respect to each other. That leaves us with the true potential of the furnace bottom. However, the measurements can still be faulty if the furnace is unbalanced [40]. While the Bøckman method is the most accurate way of measuring electrode voltage, it can be difficult to implement and maintain reliably [29].



**Figure 4.5:** Schematic drawing of electrode voltage measurement with the Bøckman method. The drawing is taken from Bøckman’s original patent [44].





## Chapter 5

# Analytical solutions

Analytical approaches are feasible when treating the primary and secondary sides separately. In this chapter we thus find analytical solutions for the separate models, both in the balanced and unbalanced case, and use them to find analytical expressions for circulating currents, effects and power factor. We will need digraphs representing the circuit diagrams in Fig. 4.1, and they are presented in Fig. 5.1. The graphs are numbered such that the edges constituting a spanning tree come first.

### 5.1 Secondary side

The incidence matrix of the secondary side digraph in Fig. 5.1a is

$$\mathcal{A} = \begin{bmatrix} 1 & 1 & 1 & 0 & 0 & 0 \\ -1 & 0 & 0 & -1 & 0 & 1 \\ 0 & -1 & 0 & 1 & -1 & 0 \\ 0 & 0 & -1 & 0 & 1 & -1 \end{bmatrix}$$

and the inductance matrix is

$$\mathcal{D} = \begin{bmatrix} Z_{e1} & 0 & 0 & 0 & 0 & 0 \\ 0 & Z_{e2} & 0 & 0 & 0 & 0 \\ 0 & 0 & Z_{e3} & 0 & 0 & 0 \\ 0 & 0 & 0 & Z_{v1} & 0 & 0 \\ 0 & 0 & 0 & 0 & Z_{v2} & 0 \\ 0 & 0 & 0 & 0 & 0 & Z_{v3} \end{bmatrix},$$

where  $Z_{ei}$ ,  $i = 1, 2, 3$  are the electrode impedances and  $Z_{vi}$ ,  $i = 1, 2, 3$  are the source voltage impedances. Edges 4, 5 and 6 have voltage sources and there are no current sources, giving the vectors

$$\tilde{\mathbf{E}} = \begin{bmatrix} 0 & 0 & 0 & V_1 & V_2 & V_3 \end{bmatrix},$$

$$\tilde{\Psi} = \begin{bmatrix} 0 & 0 & 0 & 0 \end{bmatrix},$$

of complex amplitudes. Following the method in Sec. 3.3, we find the basis of  $\ker(\mathcal{A})$  to be

$$\mathbf{U} = \begin{bmatrix} -1 & 0 & 1 \\ 1 & -1 & 0 \\ 0 & 1 & -1 \\ 1 & 0 & 0 \\ 0 & 1 & 0 \\ 0 & 0 & 1 \end{bmatrix},$$

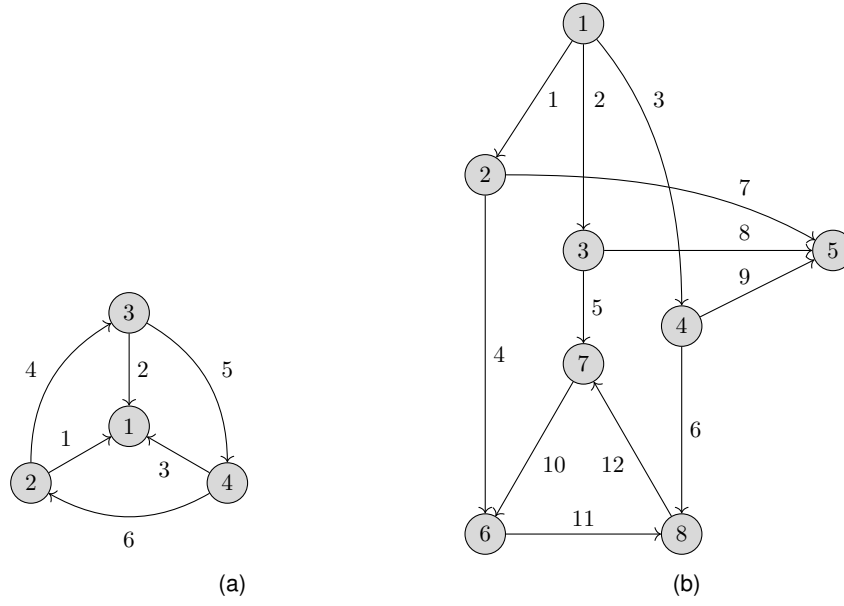


Figure 5.1: Directed graphs of (a) the secondary side circuit and (b) the primary side circuit.

resulting in the matrix equation

$$\begin{bmatrix} -Z_{e1} & Z_{e2} & 0 & Z_{v1} & 0 & 0 \\ 0 & -Z_{e2} & Z_{e3} & 0 & Z_{v2} & 0 \\ Z_{e1} & 0 & -Z_{e3} & 0 & 0 & Z_{v3} \\ 1 & 1 & 1 & 0 & 0 & 0 \\ -1 & 0 & 0 & -1 & 0 & 1 \\ 0 & -1 & 0 & 1 & -1 & 0 \end{bmatrix} \begin{bmatrix} I_1 \\ I_2 \\ I_3 \\ I_4 \\ I_5 \\ I_6 \end{bmatrix} = \begin{bmatrix} V_1 \\ V_2 \\ V_3 \\ 0 \\ 0 \\ 0 \end{bmatrix} \quad (5.1)$$

where  $I$  and  $V$  denote complex amplitudes. This equation can be solved analytically, and we will be using the Python library `SymPy` [45] to do so.

### 5.1.1 Balanced circuit

In a balanced circuit the three source voltages have the same amplitude and are phase shifted by  $2\pi/3$  relative to each other such that  $V_1 + V_2 + V_3 = 0$ , the electrode impedances are equal, meaning that  $Z_{e1} = Z_{e2} = Z_{e3} = Z_e$ , and the impedances of the source voltages are also equal, such that  $Z_{v1} = Z_{v2} = Z_{v3} = Z_v$ . The solution of Eq. (5.1) is then

$$\begin{bmatrix} I_1 \\ I_2 \\ I_3 \\ I_4 \\ I_5 \\ I_6 \end{bmatrix} = \frac{1}{3Z_e + Z_v} \begin{bmatrix} V_3 - V_1 \\ V_1 - V_2 \\ V_2 - V_3 \\ V_1 \\ V_2 \\ V_3 \end{bmatrix}. \quad (5.2)$$

The circulating current as defined in Eq. (4.1) is

$$I_c = \frac{1}{3} (I_4 + I_5 + I_6) = \frac{V_1 + V_2 + V_3}{9Z_e + 3Z_v} = 0. \quad (5.3)$$

In a balanced circuit there is no circulating current.

### 5.1.2 Unbalanced electrodes

In a circuit where the electrodes are unbalanced, we still have  $V_1 + V_2 + V_3 = 0$  and  $Z_{v1} = Z_{v2} = Z_{v3} = Z_v$ , but the electrode impedances are not equal. This will practically always be the case in a real furnace, since the electrodes are moved independently and the material in the furnace is not distributed with perfect symmetry around them. In this case we get a solution of the form

$$\begin{bmatrix} I_1 \\ I_2 \\ I_3 \\ I_4 \\ I_5 \\ I_6 \end{bmatrix} = \frac{1}{\alpha} \begin{bmatrix} V_3(3Z_{e2} + Z_v) - V_1(3Z_{e3} + Z_v) \\ V_1(3Z_{e3} + Z_v) - V_2(3Z_{e1} + Z_v) \\ V_2(3Z_{e1} + Z_v) - V_3(3Z_{e2} + Z_v) \\ 2V_1Z_{e3} + V_1Z_v - V_2Z_{e1} - V_3Z_{e2} \\ 2V_2Z_{e1} + V_2Z_v - V_3Z_{e2} - V_1Z_{e3} \\ 2V_3Z_{e2} + V_3Z_v - V_1Z_{e3} - V_2Z_{e1} \end{bmatrix}, \quad (5.4)$$

where

$$\alpha = 3Z_{e1}Z_{e2} + 3Z_{e1}Z_{e3} + 2Z_{e1}Z_v + 3Z_{e2}Z_{e3} + 2Z_{e2}Z_v + 2Z_{e3}Z_v + Z_v^2.$$

The circulating current is

$$I_c = \frac{1}{3} (I_4 + I_5 + I_6) = \frac{V_1Z_v + V_2Z_v + V_3Z_v}{3\alpha} = 0. \quad (5.5)$$

There is no circulating current, even if the electrode impedances are different.

### 5.1.3 Unbalanced transformers

Unbalanced transformers may occur in some control scenarios, where the operators choose to use different tap positions, or windings ratios, for different transformers [34]. We model unbalanced transformers as the voltage sources on the secondary side having different magnitude, but still assume that the supplied voltages are phase shifted by  $2\pi/3$  compared to each other. For simplicity we also assume here that the internal impedance of the voltage sources are equal, although that is probably not true. Thus, we have  $Z_{v1} = Z_{v2} = Z_{v3} = Z_v$  and  $Z_{e1} = Z_{e2} = Z_{e3} = Z_e$ , but  $V_1 + V_2 + V_3 \neq 0$ . The current solution is in this case

$$\begin{bmatrix} I_1 \\ I_2 \\ I_3 \\ I_4 \\ I_5 \\ I_6 \end{bmatrix} = \frac{1}{3Z_eZ_v + Z_v^2} \begin{bmatrix} (V_3 - V_1)Z_v \\ (V_1 - V_2)Z_v \\ (V_2 - V_3)Z_v \\ V_1Z_v + (V_1 + V_2 + V_3)Z_e \\ V_2Z_v + (V_1 + V_2 + V_3)Z_e \\ V_3Z_v + (V_1 + V_2 + V_3)Z_e \end{bmatrix}. \quad (5.6)$$

We get a non-zero circulating current

$$I_c = \frac{1}{3} (I_4 + I_5 + I_6) = \frac{(V_1 + V_2 + V_3)Z_v + 3(V_1 + V_2 + V_3)Z_e}{9Z_eZ_v + 3Z_v^2} = \frac{V_1 + V_2 + V_3}{3Z_v}. \quad (5.7)$$

## 5.2 Primary side

The incidence matrix and impedance matrix of the digraph in Fig. 5.1b are

$$\mathcal{A} = \begin{bmatrix} -1 & -1 & -1 & 0 & 0 & 0 & 0 & 0 & 0 & 0 & 0 & 0 \\ 1 & 0 & 0 & -1 & 0 & 0 & -1 & 0 & 0 & 0 & 0 & 0 \\ 0 & 1 & 0 & 0 & -1 & 0 & 0 & -1 & 0 & 0 & 0 & 0 \\ 0 & 0 & 1 & 0 & 0 & -1 & 0 & 0 & -1 & 0 & 0 & 0 \\ 0 & 0 & 0 & 0 & 0 & 0 & 1 & 1 & 1 & 0 & 0 & 0 \\ 0 & 0 & 0 & 1 & 0 & 0 & 0 & 0 & 0 & 1 & -1 & 0 \\ 0 & 0 & 0 & 0 & 1 & 0 & 0 & 0 & 0 & -1 & 0 & 1 \\ 0 & 0 & 0 & 0 & 0 & 1 & 0 & 0 & 0 & 0 & 1 & -1 \end{bmatrix},$$

$$\mathcal{D} = \begin{bmatrix} Z & 0 & 0 & 0 & 0 & 0 & 0 & 0 & 0 & 0 & 0 & 0 \\ 0 & Z & 0 & 0 & 0 & 0 & 0 & 0 & 0 & 0 & 0 & 0 \\ 0 & 0 & Z & 0 & 0 & 0 & 0 & 0 & 0 & 0 & 0 & 0 \\ 0 & 0 & 0 & Z & 0 & 0 & 0 & 0 & 0 & 0 & 0 & 0 \\ 0 & 0 & 0 & 0 & Z & 0 & 0 & 0 & 0 & 0 & 0 & 0 \\ 0 & 0 & 0 & 0 & 0 & Z & 0 & 0 & 0 & 0 & 0 & 0 \\ 0 & 0 & 0 & 0 & 0 & 0 & Z_{C1} & 0 & 0 & 0 & 0 & 0 \\ 0 & 0 & 0 & 0 & 0 & 0 & 0 & Z_{C2} & 0 & 0 & 0 & 0 \\ 0 & 0 & 0 & 0 & 0 & 0 & 0 & 0 & Z_{C3} & 0 & 0 & 0 \\ 0 & 0 & 0 & 0 & 0 & 0 & 0 & 0 & 0 & Z_{p1} & 0 & 0 \\ 0 & 0 & 0 & 0 & 0 & 0 & 0 & 0 & 0 & 0 & Z_{p3} & 0 \\ 0 & 0 & 0 & 0 & 0 & 0 & 0 & 0 & 0 & 0 & 0 & Z_{p2} \end{bmatrix},$$

where the impedance of edges 1 to 6 are set to the same  $Z$ , representing a small non-zero resistance in the conducting wires,  $Z_{Ci}$ ,  $i = 1, 2, 3$  are the impedances of the capacitors and  $Z_{pi}$ ,  $i = 1, 2, 3$  are the impedances of the primary side transformers. The complex amplitudes of the source voltages and currents are

$$\tilde{\mathbf{E}} = [V_1 \ V_2 \ V_3 \ 0 \ 0 \ 0 \ 0 \ 0 \ 0 \ 0 \ 0 \ 0 \ 0],$$

$$\tilde{\Psi} = [0 \ 0 \ 0 \ 0 \ 0 \ 0 \ 0 \ 0 \ 0],$$

and the basis of  $\ker(\mathcal{A})$  is

$$\mathbf{U} = \begin{bmatrix} -1 & -1 & -1 & 1 & 0 \\ 1 & 0 & 1 & 0 & -1 \\ 0 & 1 & 0 & -1 & 1 \\ 0 & 0 & -1 & 1 & 0 \\ 0 & 0 & 1 & 0 & -1 \\ 0 & 0 & 0 & -1 & 1 \\ -1 & -1 & 0 & 0 & 0 \\ 1 & 0 & 0 & 0 & 0 \\ 0 & 1 & 0 & 0 & 0 \\ 0 & 0 & 1 & 0 & 0 \\ 0 & 0 & 0 & 1 & 0 \\ 0 & 0 & 0 & 0 & 1 \end{bmatrix}.$$

The equation for the primary side system is then

$$\begin{bmatrix} -Z & Z & 0 & 0 & 0 & 0 & -Z_{C1} & Z_{C2} & 0 & 0 & 0 & 0 \\ -Z & 0 & Z & 0 & 0 & 0 & -Z_{C1} & 0 & Z_{C3} & 0 & 0 & 0 \\ -Z & Z & 0 & -Z & Z & 0 & 0 & 0 & 0 & Z_{p1} & 0 & 0 \\ Z & 0 & -Z & Z & 0 & -Z & 0 & 0 & 0 & 0 & Z_{p3} & 0 \\ 0 & -Z & Z & 0 & -Z & Z & 0 & 0 & 0 & 0 & 0 & Z_{p2} \\ -1 & -1 & -1 & 0 & 0 & 0 & 0 & 0 & 0 & 0 & 0 & 0 \\ 1 & 0 & 0 & -1 & 0 & 0 & -1 & 0 & 0 & 0 & 0 & 0 \\ 0 & 1 & 0 & 0 & -1 & 0 & 0 & -1 & 0 & 0 & 0 & 0 \\ 0 & 0 & 1 & 0 & 0 & -1 & 0 & 0 & -1 & 0 & 0 & 0 \\ 0 & 0 & 0 & 0 & 0 & 0 & 1 & 1 & 1 & 0 & 0 & 0 \\ 0 & 0 & 0 & 1 & 0 & 0 & 0 & 0 & 0 & 1 & -1 & 0 \\ 0 & 0 & 0 & 0 & 1 & 0 & 0 & 0 & 0 & -1 & 0 & 1 \end{bmatrix} \begin{bmatrix} I_1 \\ I_2 \\ I_3 \\ I_4 \\ I_5 \\ I_6 \\ I_7 \\ I_8 \\ I_9 \\ I_{10} \\ I_{11} \\ I_{12} \end{bmatrix} = \begin{bmatrix} V_2 - V_1 \\ V_3 - V_1 \\ V_2 - V_1 \\ V_1 - V_3 \\ V_3 - V_2 \\ 0 \\ 0 \\ 0 \\ 0 \\ 0 \\ 0 \\ 0 \end{bmatrix}. \quad (5.8)$$

where  $I$  and  $V$  are complex amplitudes.

### 5.2.1 Balanced circuit

Let the three voltage sources are balanced such that  $V_1 + V_2 + V_3 = 0$ , the capacitors have equal impedances  $Z_{C1} = Z_{C2} = Z_{C3} = Z_C$  and the transformers have equal impedances  $Z_{p1} = Z_{p3} = Z_{p2} = Z_p$ . The solution of Eq. (5.8) is then

$$\begin{bmatrix} I_1 \\ I_2 \\ I_3 \\ I_4 \\ I_5 \\ I_6 \\ I_7 \\ I_8 \\ I_9 \\ I_{10} \\ I_{11} \\ I_{12} \end{bmatrix} = \frac{1}{3Z^2 + 6ZZ_C + ZZ_p + Z_CZ_p} \begin{bmatrix} V_1(3Z + 3Z_C + Z_p) \\ V_2(3Z + 3Z_C + Z_p) \\ V_3(3Z + 3Z_C + Z_p) \\ 3V_1Z_C \\ 3V_2Z_C \\ 3V_3Z_C \\ V_1(3Z + Z_p) \\ V_2(3Z + Z_p) \\ V_3(3Z + Z_p) \\ V_2Z_C - V_1Z_C \\ V_1Z_C - V_3Z_C \\ V_3Z_C - V_2Z_C \end{bmatrix}, \quad (5.9)$$

and the circulating current in the delta connected transformers, as defined in Eq. (4.2), is

$$I_c = \frac{1}{3} (I_{10} + I_{11} + I_{12}) = \frac{V_2Z_C - V_1Z_C + V_1Z_C - V_3Z_C + V_3Z_C - V_2Z_C}{9Z^2 + 18ZZ_C + 3ZZ_p + 3Z_CZ_p} = 0. \quad (5.10)$$

We can also calculate the reactive power  $Q$ , active power  $P$  and apparent power  $S$  in the primary side transformers and capacitors. We assume that the load in the conductors is purely resistive, such that  $Z = R$  for some resistance  $R$ , and that the load in the conductors is purely reactive, such that  $Z_C = -j/\omega C$  for some angular frequency  $\omega$  and capacitance  $C$ . The impedance of the transformers are assumed to have both resistive and reactive elements, such that  $Z_p = R_p + j\omega L$  for some resistance  $R_p$ , angular

frequency  $\omega$  and inductance  $L$ . The reactive power in a transformer is then

$$\begin{aligned}
Q_{10} &= \frac{1}{2} |I_{10}|^2 X_{p1} \\
&= \frac{1}{2} \left| \frac{-V_1 Z_C + V_2 Z_C}{3Z^2 + 6ZZ_C + ZZ_p + Z_C Z_p} \right|^2 X_{p1} \\
&= \frac{1}{2} \left| \frac{jV_0 \frac{1}{\omega C} - j \left( -\frac{1}{2} + j \frac{\sqrt{3}}{2} \right) V_0 \frac{1}{\omega C}}{3R^2 - j6R \frac{1}{\omega C} + R(R_p + j\omega L) - j \frac{1}{\omega C} (R_p + j\omega L)} \right|^2 \omega L \\
&= \frac{V_0^2}{8\omega^2 C^2} \frac{\sqrt{3}^2 + 3^2}{\left( 3R^2 + RR_p + \frac{L}{C} \right)^2 + \left( -\frac{6R}{\omega C} + R\omega L - \frac{R_p}{\omega C} \right)^2} \omega L \\
&= \frac{\frac{3}{2} V_0^2 \omega L}{\left( 3R^2 + RR_p + \frac{L}{C} \right)^2 \omega^2 C^2 + \left( -\frac{6R}{\omega C} + R\omega L - \frac{R_p}{\omega C} \right)^2 \omega^2 C^2},
\end{aligned}$$

and because of symmetry the three primary side transformers have the same reactive power

$$Q_p = \frac{\frac{3}{2} V_0^2 \omega L}{\left( 3R^2 + RR_p + \frac{L}{C} \right)^2 \omega^2 C^2 + \left( -\frac{6R}{\omega C} + R\omega L - \frac{R_p}{\omega C} \right)^2 \omega^2 C^2}. \quad (5.11)$$

For the capacitors

$$\begin{aligned}
Q_7 &= \frac{1}{2} |I_7|^2 X_{C1} \\
&= \frac{1}{2} \left| \frac{V_1 (3Z + Z_p)}{3Z^2 + 6ZZ_C + ZZ_p + Z_C Z_p} \right|^2 X_{C1} \\
&= \frac{\frac{1}{2} \left( 9R^2 + 6RR_p + R_p^2 + \omega^2 L^2 \right) V_0^2 \omega C}{\left( 3R^2 + RR_p + \frac{L}{C} \right)^2 \omega^2 C^2 + \left( -\frac{6R}{\omega C} + R\omega L - \frac{R_p}{\omega C} \right)^2 \omega^2 C^2},
\end{aligned}$$

and again because of symmetry the reactive power of all three capacitors is

$$Q_C = \frac{\frac{1}{2} \left( 9R^2 + 6RR_p + R_p^2 + \omega^2 L^2 \right) V_0^2 \omega C}{\left( 3R^2 + RR_p + \frac{L}{C} \right)^2 \omega^2 C^2 + \left( -\frac{6R}{\omega C} + R\omega L - \frac{R_p}{\omega C} \right)^2 \omega^2 C^2}. \quad (5.12)$$

We similarly find that

$$P_p = \frac{\frac{3}{2} V_0^2 R_p}{\left( 3R^2 + RR_p + \frac{L}{C} \right)^2 \omega^2 C^2 + \left( -\frac{6R}{\omega C} + R\omega L - \frac{R_p}{\omega C} \right)^2 \omega^2 C^2}$$

and

$$P_C = 0$$

since the capacitors are purely reactive. The apparent power is then

$$\begin{aligned}
S_p &= \sqrt{P_p^2 + Q_p^2} \\
&= \frac{\frac{3}{2} V_0^2 \sqrt{R_p^2 + \omega^2 L^2}}{\left( 3R^2 + RR_p + \frac{L}{C} \right)^2 \omega^2 C^2 + \left( -\frac{6R}{\omega C} + R\omega L - \frac{R_p}{\omega C} \right)^2 \omega^2 C^2}
\end{aligned}$$

and

$$\begin{aligned}
S_C &= \sqrt{P_C^2 + Q_C^2} \\
&= \frac{\frac{1}{2} (9R^2 + 6RR_p + R_p^2 + \omega^2 L^2) V_0^2 \omega C}{\left(3R^2 + RR_p + \frac{L}{C}\right)^2 \omega^2 C^2 + \left(-\frac{6R}{\omega C} + R\omega L - \frac{R_p}{\omega C}\right)^2 \omega^2 C^2}
\end{aligned}$$

for the transformers and capacitors, respectively.

### 5.2.2 Unbalanced capacitors

We can also find the solution when we have unbalanced capacitors, that is with  $V_1 + V_2 + V_3 = 0$  and  $Z_{p1} = Z_{p3} = Z_{p2} = Z_p$ , but not equal capacitor impedances. The expressions are long and can be found in Eq. B.1 in Appendix B. We find that the circulating current in the delta is

$$I_c = \frac{1}{3} (I_{10} + I_{11} + I_{12}) = 0, \quad (5.13)$$

so unbalanced capacitors do not lead to a circulating current.

### 5.2.3 Unbalanced transformers

When the transformers are unbalanced we have  $V_1 + V_2 + V_3 = 0$  and  $Z_{C1} = Z_{C2} = Z_{C3} = Z_C$ . The current solution is shown in Eq. B.2 in Appendix B. We find the circulating current in the delta to be

$$\begin{aligned}
I_c &= \frac{1}{3} (I_{10} + I_{11} + I_{12}) \\
&= \frac{V_1 Z_C (3Z^2 + ZZ_{p2} + 6ZZ_C + Z_{p2}Z_C)(Z_{p1} - Z_{p3})}{3\alpha} \\
&\quad + \frac{V_2 Z_C (3Z^2 + ZZ_{p3} + 6ZZ_C + Z_{p3}Z_C)(Z_{p2} - Z_{p1})}{3\alpha} \\
&\quad + \frac{V_3 Z_C (3Z^2 + ZZ_{p1} + 6ZZ_C + Z_{p1}Z_C)(Z_{p3} - Z_{p2})}{3\alpha}.
\end{aligned}$$

When the transformers are unbalanced, there is a non-zero circulating current in the delta connected transformers on the primary side.

### 5.2.4 Power factor and capacitance

The power factor observed by the grid, corresponding to the power factor of edges 1, 2 and 3 in Fig. 5.1b, should ideally be 1, and this is the reason for including capacitors as high-voltage compensation. Assuming the circuit to be balanced, we can find the power factor directly from the phase difference between the voltage  $V_1$  and current  $I_1$  from Eq. (5.9). The voltage is

$$V_1 = V_0$$

for some real number  $V_0$ , and thus has phase angle 0 in the complex plane. For the current expression we use  $Z = R$ ,  $Z_C = -j/\omega C$  and  $Z_p = R_p + j\omega L$  as before. This

gives us a current

$$\begin{aligned}
 I_1 &= \frac{V_1 (3Z + 3Z_C + Z_p)}{3Z^2 + 6ZZ_C + ZZ_p + Z_C Z_p} \\
 &= V_0 \frac{3R - 3j\frac{1}{\omega C} + R_p + j\omega L}{3R^2 - j6R\frac{1}{\omega C} + R(R_p + j\omega L) - j\frac{1}{\omega C}(R_p + j\omega L)} \\
 &\propto 9R^3 + 6R^2 R_p - 6\frac{RL}{C} + RR_p^2 + R\omega^2 L^2 + \frac{18R + 3R_p}{\omega^2 C^2} \\
 &\quad + j \left( \frac{9R^2 + 6RR_p + R_p^2 + \omega^2 L^2}{\omega C} - \frac{3L}{\omega C^2} \right).
 \end{aligned}$$

We then find the power factor from the phase angle of  $I_1 \propto a + jb$ . Since we have a power supply and not power consumption at this point in the circuit, we let the power factor be the positive angle of  $I_1$  instead of the negative angle, such that

$$\cos \varphi = \frac{a}{\sqrt{a^2 + b^2}}.$$

We can differentiate the above expression with respect to  $C$  to find the capacitance that gives us the greatest power factor, but this is a tedious process. Instead, we use the fact that  $\cos \varphi = 1$  when  $b = 0$ . This gives us the equation

$$\frac{9R^2 + 6RR_p + R_p^2 + \omega^2 L^2}{\omega C} - \frac{3L}{\omega C^2} = 0,$$

which solving for  $C$  yields

$$C_{\text{opt}} = \frac{3L}{9R^2 + 6RR_p + R_p^2 + \omega^2 L^2}. \quad (5.14)$$

Under the assumptions we have made, this is the optimal choice of  $C$ .

Another way of finding the optimal capacitance is to set the reactive power in Eq. (5.11) of the transformers equal to the reactive power in Eq. (5.12) of the capacitors, as these are the only elements in the circuit with reactive components. The resulting equation shortens to

$$3L = (9R^2 + 6RR_p + R_p^2 + \omega^2 L^2) C,$$

which solving for  $C$  gives the criterion

$$C_{\text{opt}} = \frac{3L}{9R^2 + 6RR_p + R_p^2 + \omega^2 L^2},$$

agreeing with the optimal choice of  $C$  found in Eq. (5.14) above. We interpret this as all the reactive power being pumped between the capacitors and transformers, and thus none of the reactive power leaks back into the power grid.

Looking at current values at limits for  $C$  is also instructive. We have

$$\begin{aligned}
 \lim_{C \rightarrow \infty} I_1 &= V_0 \lim_{Z_C \rightarrow 0} \frac{3Z + 3Z_C + Z_p}{3Z^2 + 6ZZ_C + ZZ_p + Z_C Z_p} \\
 &= V_0 \frac{3Z + Z_p}{3Z^2 + ZZ_p} \\
 &= \frac{V_0}{Z},
 \end{aligned}$$



and thus a power factor  $\cos \varphi = 1$  for this limit. It is however useless in practice, as capacitors with infinite capacitance corresponds to having conductors with no resistance. All the current would therefore flow in this loop, and no current would enter the transformers. The other limit is

$$\begin{aligned}
 \lim_{C \rightarrow 0} I_1 &= V_0 \lim_{Z_C \rightarrow \infty} \frac{3Z + 3Z_C + Z_p}{3Z^2 + 6ZZ_C + ZZ_p + Z_CZ_p} \\
 &= \frac{3V_0}{6Z + Z_p} \\
 &= \frac{3V_0}{6R + R_p + j\omega L} \\
 &= \frac{3V_0 (6R + R_p - j\omega L)}{(6R + R_p)^2 + (\omega L)^2} \\
 &\propto 6R + R_p - j\omega L,
 \end{aligned}$$

with a power factor

$$\cos \varphi = \frac{6R + R_p}{\sqrt{(6R + R_p)^2 + (\omega L)^2}}.$$

This is the power factor we would get without power factor correction.



## Chapter 6

# Implementation and preliminary results

When we look at bigger circuit problems than those in the previous chapter, we need to move on from analytical solutions to numerics. In this chapter we present the implementation of our numerical solver and validation tests. With the implemented solution, we then solve the circuit model for the full system and compare it with the solutions of the separate models.

### 6.1 Implementation

We implement a numerical solver for our circuit problems as a Python module. The module is organised as a class hierarchy with different circuits making up the different classes, and uses the solution method in Sec. 3.4.2 for harmonic circuit problems. In our numerical solver the solution method is implemented as shown in Algorithm 1, with the use of NumPy [46] for fast numerical computing and array handling. The base class `Circuit` takes any incidence matrix  $\mathcal{A}$  as argument, but to ensure that the solver works properly, we have two rules for numbering nodes and edges of the graph. First, if there are  $M$  connected components, the last  $M$  nodes must be from different connected components, and second, that the edges must be numbered such that the edges constituting a spanning forest come first.

The most important function for this class is `solve`, which takes the impedance matrix  $\mathcal{Z}$ , vector of source voltages  $\tilde{\mathbf{E}}$ , and vector of source currents  $\tilde{\mathbf{\Psi}}$  as input and solves for current and voltage amplitudes  $\tilde{\mathbf{I}}$ ,  $\tilde{\mathbf{V}}$  at all points in the circuit using Algorithm 1. With this implementation, the defining element of the class instance is the circuit geometry as represented by the incidence matrix, and the same circuit can be solved multiple times with different impedance values and different source voltages and currents. After `solve` has been called, we can call the other functions to get more information. We can extract time series of currents, node voltages and voltage drops over components for a specified number of time periods and calculate active, reactive, apparent and total power, as well as power factor. All other functions use the latest current and voltage solutions from `solve`, and calling `solve` again will overwrite the previous solution with a new one.

As we will mostly be working with specific circuit configurations, we have subclasses for those such that we do not need to specify the incidence matrix every time. The subclasses are `Primary`, with incidence matrix describing the graph in Fig. 5.1b, `Secondary` for the graph in Fig. 5.1a, `HVC` for the graph in Fig. 6.3 coming later in

---

**Algorithm 1** Numerical solver for a harmonic circuit problem.

---

**Require:**  $\mathcal{A}$ ,  $\mathcal{D}$ ,  $\tilde{\mathbb{E}}$ ,  $\tilde{\Psi}$

$N \leftarrow$  number of rows in  $\mathcal{A}$

$E \leftarrow$  number of columns in  $\mathcal{A}$

$M \leftarrow N - \text{rank}(\mathcal{A})$

$\mathcal{A}_T \leftarrow \mathcal{A}[0 : N - M, 0 : N - M]$

$\mathcal{A}_C \leftarrow \mathcal{A}[0 : N - M, N - M : ]$

$\mathbf{U} \leftarrow \begin{bmatrix} -\mathcal{A}_T^{-1} \mathcal{A}_C \\ \mathcal{I}_{(E-N+M) \times (E-N+M)} \end{bmatrix}$

$\mathbf{A} \leftarrow \begin{bmatrix} \mathbf{U}^T \mathcal{D} \\ \mathcal{A}[0 : N - M] \end{bmatrix}$

$\mathbf{b} \leftarrow [\mathbf{U}^T \tilde{\mathbb{E}} \quad \tilde{\Psi}[0 : N - M]]^T$

$\tilde{\mathbb{I}} \leftarrow$  solution of  $\mathbf{A}\mathbf{x} = \mathbf{b}$

$\tilde{\mathbf{V}} \leftarrow$  least square solution of  $\mathcal{A}^T \mathbf{x} = \tilde{\mathbb{E}} - \mathcal{D}\tilde{\mathbb{I}}$

**return**  $\tilde{\mathbb{I}}$ ,  $\tilde{\mathbf{V}}$

---

this chapter, and LVC for the graph in Fig. 7.1 that we will be working with in the next chapter. The structure of the impedance matrix for each of those circuits is also supplied, so when calling `solve` we specify the impedance values of each component instead of the entire impedance matrix. Additionally, the classes `Primary` and `HVC` have a function `find_optimal_capacitance`, that returns the capacitance which gives a grid power factor of one.

The other code for this thesis mostly uses the `Circuit` module to solve different variations of the circuit problems. We use the libraries `Matplotlib` [47] and `Seaborn` [48] to generate plots, and `Pandas` [49], [50] for reading data. Most of the code is available in a GitHub repository [51]. The repository does not include data files with measurements since they are confidential, and the same is true for the metamodel code that we will make use of. Therefore, all code for the current and next chapter is available, but some code and data for Chapters 8 and 9 are not.

## 6.2 Validation

We first test the circuit solver on the classes `Primary` and `Secondary` by checking whether it agrees with the analytical solution. For the numerical solution, we want to use somewhat realistic parameter values. Table 6.1 shows the values chosen for the primary side. Voltage supply, angular frequency and capacitance are set to realistic values for a submerged arc furnace, and transformer resistance and reactance are chosen so that they give realistic power output. The conducting resistance is set to be very small, but non-zero. With these values, the generated active power in the transformers is 41.5 MW, the transformer power factor is 0.73 and the grid power factor is 0.83.

Table 6.2 shows the values chosen for the secondary side. Most secondary side values are based on the latest version of the web ferromanganese metamodel [36]. We use

**Table 6.1:** The parameter values used for numerical solutions to the primary side circuit.

Parameter	Value
Voltage supply $V_0$	20 kV
Angular frequency $\omega$	$100\pi$
Conductor resistance $R$	1 n $\Omega$
Capacitance $C$	53 $\mu F$
Transformer resistance $R_p$	23.4 $\Omega$
Transformer reactance $X_p$	21.6 $\Omega$

**Table 6.2:** The parameter values used for numerical solutions to the secondary side circuit.

Parameter	Value
Voltage supply $V_0$	354 V
Angular frequency $\omega$	$100\pi$
Electrode resistance $R_e$	681 $\mu\Omega$
Electrode reactance $X_e$	812 $\mu\Omega$
Voltage source resistance $R_v$	31,6 $\mu\Omega$
Voltage source reactance $X_v$	409 $\mu\Omega$

the ferromanganese model instead of the ferrosilicon one because it is the most updated model, and we do not expect the values to be drastically different. Electrode impedances are read directly from the output and source voltages are  $\sqrt{3}$  times the electrode voltages from the metamodel. For the source voltage impedance, we use an estimate for inner transformer impedance for a ferrosilicon submerged arc furnace [34] to get values in a realistic range. From [34] we find estimates of an inner transformer resistance of 15.7  $\mu\Omega$  and reactance of 78.4  $\mu\Omega$ . But since we have lumped the impedance of the bus bars and flexibles together with the source voltage impedance in our model, and we must add the estimate of these impedances to our voltage source impedance. We therefore add 1/3 of the combined impedance of all bus bars and flexibles to the estimate of each transformer impedance. This gives us a total resistance of  $R_v = 31,6 \mu\Omega$  and a total reactance of  $X_v = 409 \mu\Omega$  for each voltage source.

With these values our numerical circuit model has a peak electrode current of 173.9 kA compared to 193.2 kA from the metamodel, which is 9.9 % smaller. However, the metamodel and numerical circuit model work in fundamentally different ways, and to verify the numerical model we need to check it against analytical solutions.

We solve the primary side circuit model with the parameter values of Tab. 6.1 and insert the same values into the balanced analytical solution for the primary side. For the currents in Eq. (5.9) and reactive powers of transformers and capacitors in Eqs. (5.11) and (5.12) we get relative errors of order  $10^{-16}$  or smaller, meaning the solutions are equal to machine precision. There is zero circulating current in the numerical solution both for the balanced case and when the capacitors are unbalanced, as it should be according to Eqs. (5.10) and (5.13).

We also check that the numerical and analytical solutions give the same circulating currents when the transformers are unbalanced. We calculate the circulating current for a grid of values where the resistance and reactance of one transformer varies from 10 percent below to 10 percent above the other two. Comparing the numerical and analytical results, the largest absolute error is of order  $10^{-13}$ . Figure 6.1 shows the

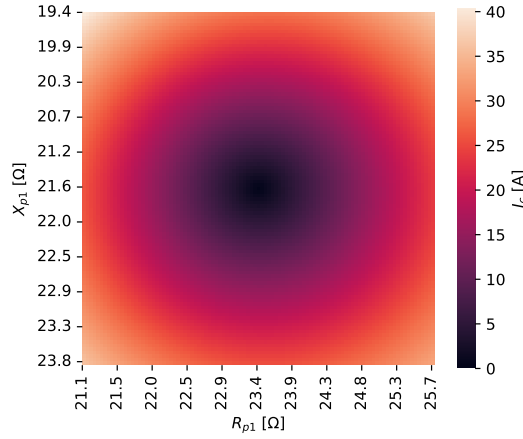


Figure 6.1: Primary side circulating currents for the case where one transformer has a different resistance  $R_{p1}$  and reactance  $X_{p1}$  from the other two transformers, calculated from the primary side circuit model.

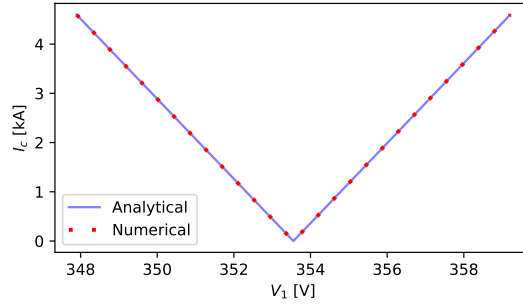


Figure 6.2: Secondary side circulating currents for the case where one voltage source has a different magnitude from the two others, calculated with the secondary side circuit model.

circulating current in this scenario.

We do the same kind of analysis on the secondary side, and here find the relative current error to be of the order  $10^{-15}$  or smaller when the system is balanced. The circulating current in the numerical model is zero both in the balanced case and when the electrodes are unbalanced, as it should be according to Eqs. (5.3) and (5.5). Figure 6.2 shows the circulating current as a function of the peak source voltage  $V_1$ , that varies from about 5.7 V below to 5.7 V above the two others. This is the voltage difference used by [34]. The analytical and numerical solutions agree, with a maximum absolute error of order  $10^{-11}$ . The largest circulating current found above is 4.60 kA, or 3.25 kA as an r.m.s. current. This is 5.8 % lower than the estimated r.m.s. circulating current of 3.45 kA found by Sævarsdóttir *et al.* [34].

We conclude that the analytical and numerical solutions agree with each other, and our implementation of the solver is correct.

### 6.3 Full system preliminary results

We are now ready to look at the whole system, supply and furnace together, using the numerical circuit solver. Comparing the separate circuit models to the full model will serve as a good test both of our model choice and our implementation.

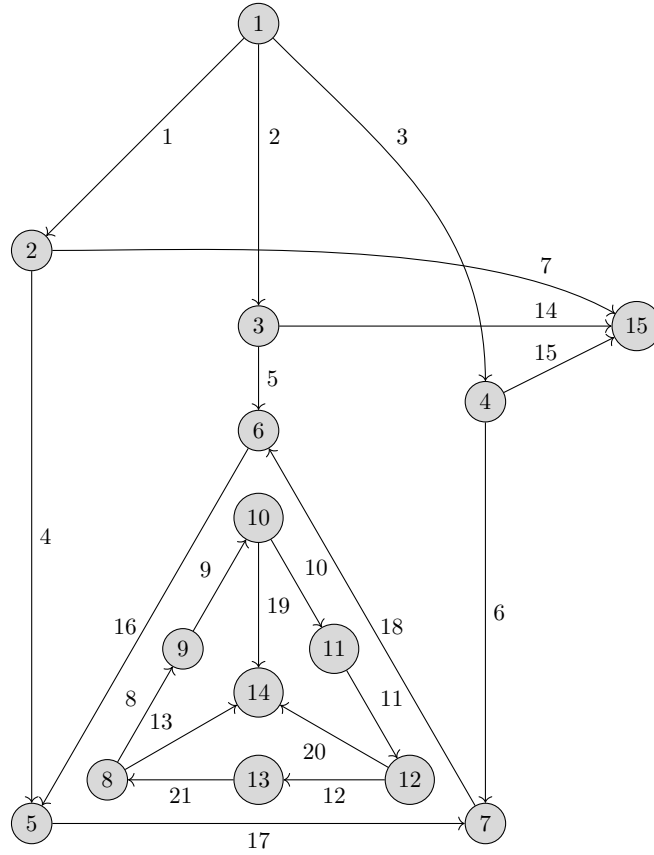


Figure 6.3: Directed graph of the full system.

A graph corresponding to the circuit in Fig. 4.2 is shown in Fig. 6.3, which the circuit class HVC is based on. When solving this system, we use the same values for voltage supply, angular frequency, capacitance, conductor resistance, and electrode impedance as when solving the primary and secondary sides separately. Deciding realistic parameter values for the transformers require more deliberation.

### 6.3.1 Estimating transformer parameters

For the transformer we need self inductances for both the primary and secondary sides, mutual inductance, and the inductance and resistance representing the non-ideal conditions.

Starting with the self and mutual inductances, we use the formula

$$L = \frac{N^2 \mu_r \mu_0 A}{l}, \quad (6.1)$$

for the self inductance  $L$  of a conducting coil wrapped around a core [23] as a starting point for our estimate. Here  $N$  is the total number of windings,  $\mu_r$  is the relative permeability of the core,  $\mu_0$  is magnetic permeability of vacuum,  $A$  is the cross-section area of the core and  $l$  is the core length.  $\mu_0$  is known, all the other values are uncertain.

The relative permeability of a powder iron core typically ranges from 15 to 550 according to Hurley and Wölfe [23]. We arbitrarily choose a value in that range as our starting point, say  $\mu_r = 120$ . We further guess a cross-section area of  $A = 10^{-2} \text{ m}^2$  and core length  $l = 10 \text{ m}$ . We know that the potential is about  $10^4 \text{ V}$  on the primary side

Table 6.3: The parameter values used for numerical solutions to the full system.

Parameter	Value
Voltage supply $V_0$	20 kV
Angular frequency $\omega$	$100\pi$
Conductor resistance $R$	1 n $\Omega$
Capacitance $C$	53 $\mu$ F
Primary side self inductance $L_p$	15 H
Secondary side self inductance $L_s$	1.5 mH
Magnetic leakage flux inductance $L_t$	0.1 $\mu$ H
Winding resistance $R_t$	40 $\mu\Omega$
Electrode resistance $R_e$	681 $\mu\Omega$
Electrode reactance $X_e$	812 $\mu\Omega$

and  $10^2$  V on the secondary side, so we guess  $N_p = 10^2 N_s$  where the subscripts  $p$  and  $s$  denote the primary and secondary sides, respectively. The absolute value is unknown, we make a guess at  $N_s = 10^2$ . With these values we get

$$\begin{aligned} L_p &= 15 \text{ H} \\ L_s &= 1.5 \text{ mH.} \end{aligned}$$

The mutual inductance is then given by Eq. (2.7).

We find reasonable values for the inductance  $L_t$  representing the magnetic leakage flux and the resistance  $R_t$  representing winding resistance by choosing values that give realistic output. Choosing  $L_t = 0.1 \mu\text{H}$  and  $R_t = 40 \mu\Omega$  gives results close to what can be expected from a furnace, namely a grid power factor of 0.74, an electrode peak current of 186 kA, an active delivered power of 35 MW to the electrodes and a 2 percent loss of active power through the transformers due to resistance. We therefore use these values as our first estimate.

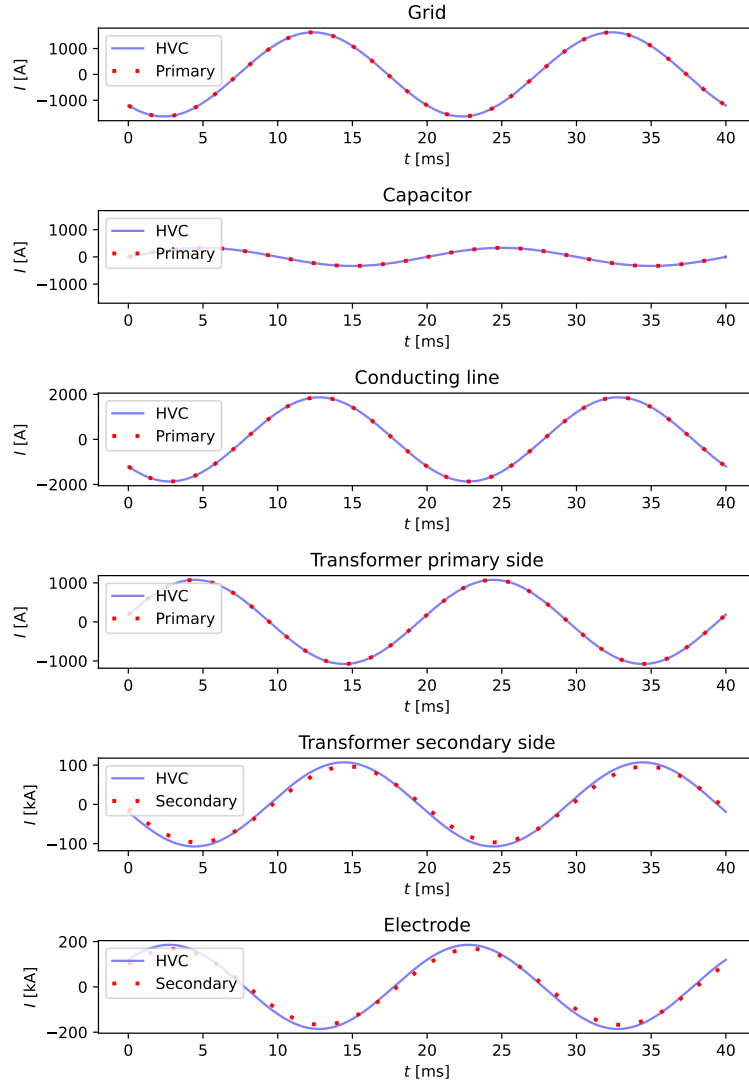
Note that all estimates found here are highly uncertain, and chosen ad hoc to best fit what we expect. While they seem to work well in our estimates here, we will update several of the values in Chapter 9 when we get to comparisons with real measurement data and thus have more information.

### 6.3.2 Comparison with separate models

We can now compare the numerical results of the full model with the separate models of the primary and secondary sides. We expect the two approaches to give similar results and show similar behaviour, and the comparison thus serves as a useful test. The parameter values we use, some known and some estimated as described in the previous section, are listed in Tab. 6.3.

We start by comparing the currents and voltages as found by the full model and by the primary and secondary side models in the balanced case. The parameter values for the primary and secondary side models are chosen to correspond to the values in Tab. 6.3 as far as possible. Therefore, the transformer impedances to be used in the primary side model and the voltage amplitude to be used in the secondary side model are found from the full model. We have however not matched the transformer parameters of the full model to the internal source voltage impedance of the secondary side model, so they are estimated independently.



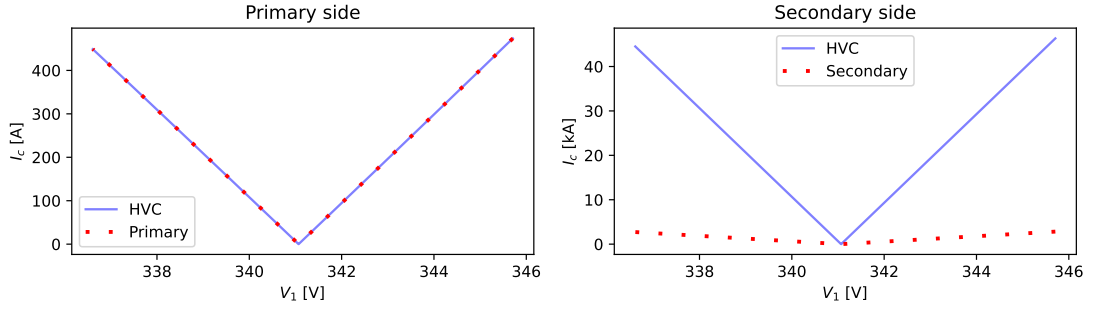


**Figure 6.4:** Time series of currents covering two periods, calculated both with the full circuit model *HVC* and with the separate models *Primary* and *Secondary*. Note that the y axes have different units and ranges.

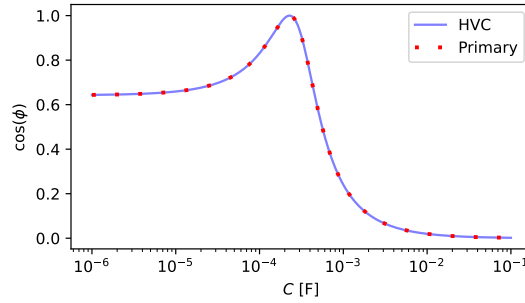
Figure 6.4 shows the result for currents. The full model and the primary side model give exactly the same results, with relative errors of order  $10^{-13}$  or smaller for the complex amplitudes. For the secondary side there are visible differences between the two models, with the complex amplitudes having a relative error of 0.117 in absolute value. The situation is exactly the same for voltages, with the primary side matching perfectly and the secondary side having a relative error of 0.117 in absolute value.

The full numerical model has no circulating current when either the electrodes or the capacitors are unbalanced, in agreement with the secondary and primary side analytical solutions. We need to take more care when it comes to comparing circulating current effects due to unbalanced transformers. As we have seen, the secondary side model does not fully agree with the full model, and additionally changes on either the primary or secondary side affects the other side.

Figure 6.5 shows the circulating currents in the primary and secondary side deltas as the windings ratio of one transformer changes, thus changing the voltage supply on



**Figure 6.5:** Circulating currents in primary and secondary side deltas when one transformer has a different windings ratio from the other two, calculated with the circuit models *HVC*, *Primary*, and *Secondary*. The circulating current is shown as a function of the voltage supply provided from the transformer that has a different windings ratio from the other two.



**Figure 6.6:** The power factor seen from the grid as a function of capacitance, calculated both with the circuit model *HVC* and the circuit model *Primary*.

the secondary side and the transformer impedance as seen from the primary side. The circulating currents are calculated with both the full model and with the primary and secondary side models, and shown as a function of the secondary side voltage supply  $V_1$  from the transformer with changing windings ratio. We see that the full circuit model and primary side model give exactly the same circulating current in the primary side delta connection. For the secondary side there is a huge difference, with the full model giving circulating currents that are 16.4 times greater than those found with the secondary side model. The circulating currents on the primary side are about 100 times smaller than those found with the full model on the secondary side, corresponding to the transformer windings ratios of about 100.

Figure 6.6 shows the power factor as seen from the grid as a function of capacitance, calculated both with the full model and with the primary side model. The models give the exact same behaviour, having one peak where the power factor is one, approaching zero as the capacitance increases and approaching a limit value between zero and one when the capacitance approaches zero. This limit is the power factor we would have if there were no power factor correction.

## 6.4 Discussion

The full circuit model and the separate models yield the same currents and voltages on the primary side, but differ somewhat on the secondary side. This is probably because

we have chosen the source voltage impedance of the secondary side model and the values for the transformers in the full model independently of each other. We found no way of choosing one set of values exactly given the other set, which indicates that the transformer model we have chosen for the full model cannot be fully represented by a simple voltage source with internal impedance as we have done for the secondary side model.

The models show existence of circulating currents in the same scenarios, but for the secondary side there is a huge difference in the magnitude of the circulating currents found by the full model and the secondary side model. This is again probably due to the different choice of impedances, and we know from Eq. 5.7 that voltage source impedance in the secondary side model is inversely proportional to the circulating current.

As the power factor of the grid as a function of capacitance is the same whether we use the primary or full numerical model, it is possible to calculate the optimal capacitance using Eq. (5.14) that we found analytically for the primary side. For a real furnace supply system,  $R_p$  and  $L$  will be found from the impedance viewed from the primary side of the transformer. That is, we can measure the primary side current and voltage and use Eq. (2.10) for finding the impedance, and insert this impedance into Eq. (5.14).

When it comes to parameter estimation for the full model, we are most uncertain about the transformer values. We have also lumped the magnetic flux leakage and winding losses together on the secondary side, so we cannot distinguish between what happens internally on the primary and secondary sides of the transformers. This is a weakness of our modelling choice, but on the other hand it would only make sense not to lump them together if we had a reliable way of measuring the effects separately. However, even if our specific estimates and therefore the exact output values of our model are uncertain, we still capture the behaviour of the system. We will also adjust the parameter values of the full circuit model when we come to comparisons with real measurements, since we will then have more information.

We conclude that the models agree to the degree we could expect, and we have confirmed that the analytical solutions agree with the primary and secondary side numerical models. The agreement between the full model and the separate numerical models serves as a good validation of the full model. Having a fast, numerical model that combines the primary and secondary sides is useful since we can study how changes on one side affect the other side. Most modelling efforts to date focus on the secondary side, so the combined model might offer new insight.



## Chapter 7

# Low-voltage compensation

With the framework we have in place, we can easily explore how the system behaves differently if we use low-voltage compensation instead of high-voltage compensation. A graph corresponding to the LVC circuit of Fig. 4.3 is shown in Fig. 7.1, where the edges and nodes are numbered according to the rules of the numerical solver. We solve both this system and the system with primary side power factor correction for capacitor values in the range  $10^{-5}$  F to  $10^3$  F. All other parameters are kept constant and equal between the two systems. The results are depicted in Fig. 7.2, where we can see the behaviour of different quantities as a function of capacitance.

The uppermost left subplot shows the power factor observed by the grid. Notably, with LVC there are two maxima where the power factor reaches 1, compared to a single maximum for HVC. The maximum corresponding to the largest capacitance results in several unwanted values for example a current drawn from the grid of almost 150 kA, delivered apparent power in the range of GVA for the transformer and a current of over 8 MA through the secondary side of transformer. We therefore consider the left maximum, corresponding to the lower capacitance, to be the realistic operating point.

The optimal capacitance as found above are presented in the top row of Tab. 7.1. The table also lists values for all other quantities shown in Fig. 7.2 at this capacitance. We see that the optimal capacitance for low-voltage compensation is about 3400 times larger than the optimal capacitance for normal primary side setup.

From the uppermost right plot, we see that the chosen maximum for low-voltage compensation is also optimal in the sense that it achieves a maximum power factor for the secondary side of the transformer. The power factor here is 0.9999. Choosing the other LVC maximum would have given a terribly low power factor for the transformer. With high-voltage compensation the transformer power factor is constant at 0.6430, a good deal below the best we achieve with low-voltage compensation.

Plots of the delivered active and apparent power from the transformer, as seen in the second row of Fig. 7.2, show that for the optimal capacitance in LVC there is a minimum for the apparent power without a dip in active power. This is possible due to the maximum in transformer power factor. Both active and apparent power in the transformer is constant for HVC.

In the middle row, we see the current from the grid and through the secondary side of the transformer. The grid current changes as a function of capacitance for both setups, and both setups have a minimum current for the optimal capacitance. The current on the secondary side of the transformer is constant for high-voltage compensation, but varies for the low-voltage compensation. Here too we have a current minimum for the optimal capacitance.

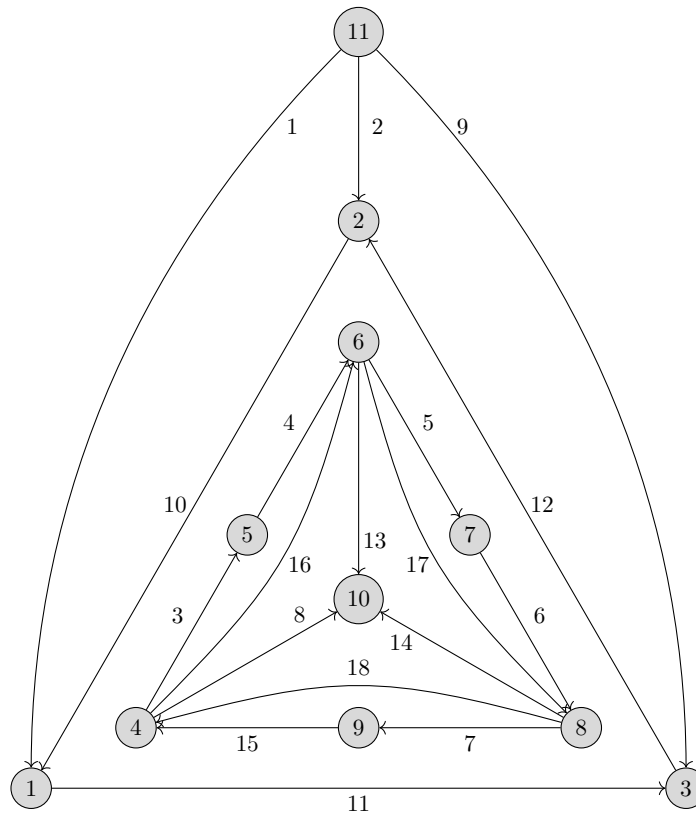


Figure 7.1: Directed graph of the full system circuit model with low-voltage compensation.

**Table 7.1:** Optimal capacitance and other circuit values at this optimal capacitance, for both high-voltage and low-voltage compensation. All transformer values are given for the secondary side.

	High-voltage compensation	Low-voltage compensation
Capacitance [mF]	0.2279	777.8
Transformer power factor	0.6430	0.9999
Transformer active power [MW]	11.76	11.94
Transformer apparent power [MVA]	18.30	11.95
Grid current [kA]	1.199	1.204
Transformer current [kA]	107.3	69.52
Electrode current [kA]	185.8	187.2
Electrode power [MW]	11.76	11.94
Capacitor current [kA]	1.432	83.98
Capacitor voltage [kV]	20.00	0.3437

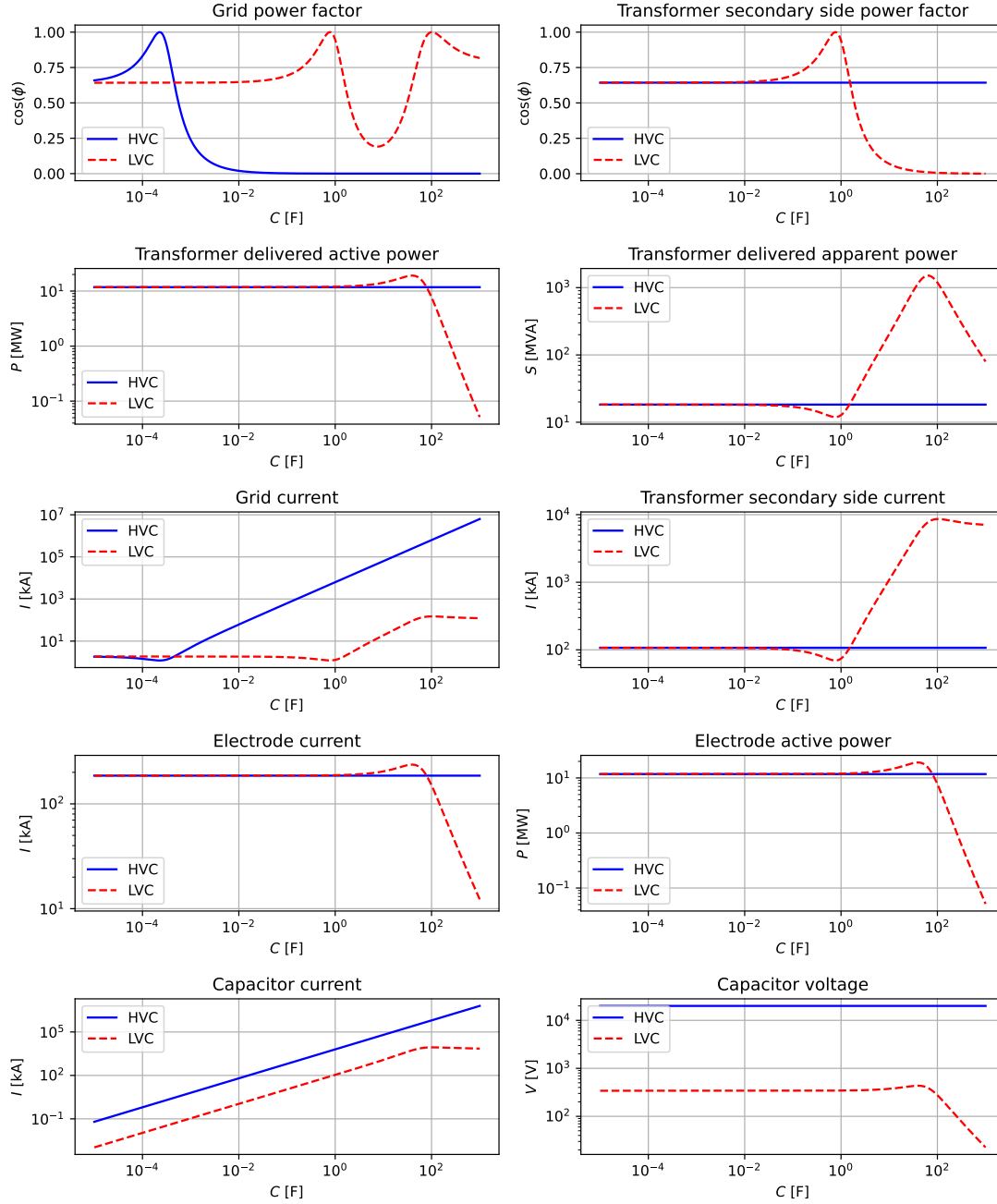


Figure 7.2: Behaviour of some power factors, powers, currents and voltages in different parts of the system as a function of capacitance, for both low-voltage compensation and high-voltage compensation.

**Table 7.2:** Slope and intercept of a first-order linear regression done on logarithmic data of transformer winding ratio versus ratio of LVC values to HVC values for several quantities.

	Slope	Intercept
Optimal capacitance ratio	2.002	-1.084
Capacitor current ratio	1.002	-0.5430
Capacitor voltage ratio	-0.9999	0.5407

The second to last row shows the current and power in an electrode. The LVC setup has peaks for electrode current and electrode power, but it is unrealistic to achieve those values since the capacitance needed is too large and would result in unwanted values in other parts of the system. But even at the desired capacitance, the current and power are slightly larger for the LVC setup than for the normal setup, as can be seen in Tab. 7.1.

Lastly, the two bottom plots show that the capacitors will be subject to currents and voltages of varying magnitude, depending both on the setup used and on the capacitance. The currents and voltages that the capacitors will be subject to when the capacitance is chosen to get a grid power factor of 1, are presented in the last rows of Tab. 7.1. A capacitor in an LVC setup will at this optimal point experience currents that are almost two orders of magnitude larger and voltages that are almost two orders of magnitude smaller than a capacitor at the optimal point for the normal setup. It is also worth noting that within the realistic range of capacitor values, the current increases with increasing capacitance and the voltage is almost constant.

We know that the optimal capacitance, and the current and voltages the capacitors will be subject to, change if the transformers change. We want to investigate how they might change differently for low-voltage and high-voltage compensation. To do that, we therefore investigate the relationship between the transformer windings ratio  $N_p/N_s$  and the ratio  $C_{opt,LVC}/C_{opt,HVC}$  of optimal capacitance value for LVC and HVC. We do the same for current through the capacitor,  $I_{C,LVC}/I_{C,HVC}$ , and voltage over the capacitor,  $V_{C,LVC}/V_{C,HVC}$ , as well.

If there is a polynomial relationship between two quantities  $x$  and  $y$  such that  $y \propto x^a$ , we have

$$y = bx^a \implies \ln y = a \ln x + \ln b. \quad (7.1)$$

Then a log-log plot of  $y$  as a function of  $x$  should result in a straight line with slope  $a$  and intercept  $\ln b$ . We use this to investigate if there is a polynomial relationship between the ratios presented above.

Figure 7.3 shows log-log plots of the ratios together with a fitted linear line. We see from the graph that the points follow the line closely, showing that there is in fact a polynomial relationship between the quantities within this range of windings ratios. Table 7.2 show the slopes and intercepts of the linear fit. We see that optimal capacitance has a slope close to 2 and current and voltage has a slope close to plus and minus 1, respectively. This means that there is a quadratic relationship between windings ratio and ratio of optimal capacitance, a linear relationship between windings ratio and ratio of current through the capacitor, and an inverse linear relationship between windings ratio and ratio of voltage over the capacitor.



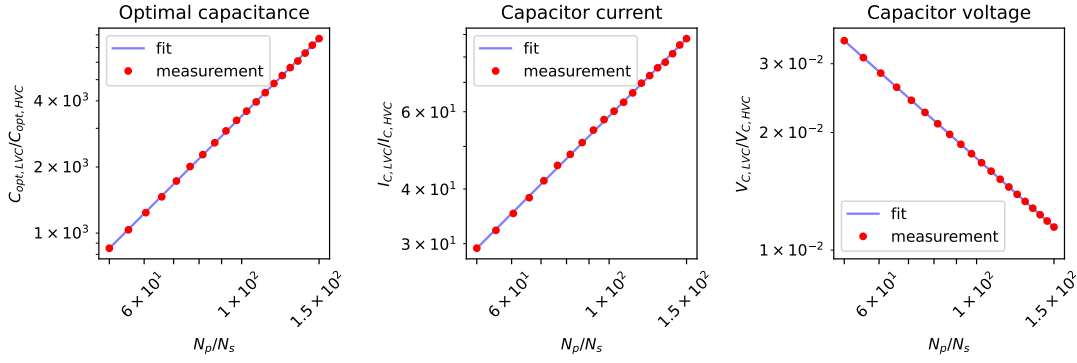


Figure 7.3: LVC to HVC ratio of optimal capacitance, capacitor current and capacitor voltage as a function of transformer windings ratio. The axes are logarithmic.

## 7.1 Discussion

Our results on low-voltage compensation show that this setup can indeed improve the power factor of the transformer, as reported by Li *et al.* [33]. Connected to this, in the transformer we see a minimum apparent power without a decrease in active power at the optimal capacitance. This means that with LVC we can deliver the same power with a smaller load on the transformer, meaning we can use a smaller transformer. A minimum for the current at this optimal point also means that we reduce the losses in the transformers and bus bars of the secondary side.

However, there are also disadvantages to LVC when compared to HVC. The capacitors are placed in a more critical area when on the secondary side, and the LVC arrangement could also complicate current measurements in the electrodes, as it would no longer be possible to calculate electrode currents directly from secondary side transformer currents. We also see that the capacitors would have to withstand currents that are 59 times higher when placed on the secondary side and set to the optimal capacitance. But the voltages will be 58 times lower in the same scenario.

We can use the relationships found in this chapter to calculate optimal capacitance, capacitor current, and capacitor voltage for LVC if we know the same values for HVC. We can use Eq. (5.14) to find the optimal capacitance for HVC and the relationship in Eq. (7.1) together with the windings ratio and the slope and intercept of Tab. 7.2 to find the optimal capacitance for LVC. The same approach can also be used to find the current and voltage the capacitors will be subjected to when placed on the secondary side and when the windings ratio changes. Note however that all the above calculations are based on a balanced system. We have not studied how much variation is introduced if the system becomes unbalanced, as all real systems are.

It is not within the scope of this thesis to answer whether LVC or the traditional HVC is the best method, but calculated estimates like the ones provided by our circuit models might help experts in the decision.



## Chapter 8

# Metamodel simulations

In this chapter we take a detour from the circuit model to do some simulations with the ferromanganese metamodel [35], [36] described in Sec. 4.3. We do this because the metamodel is revealed to display behaviour that ties into our later results for measurement data.

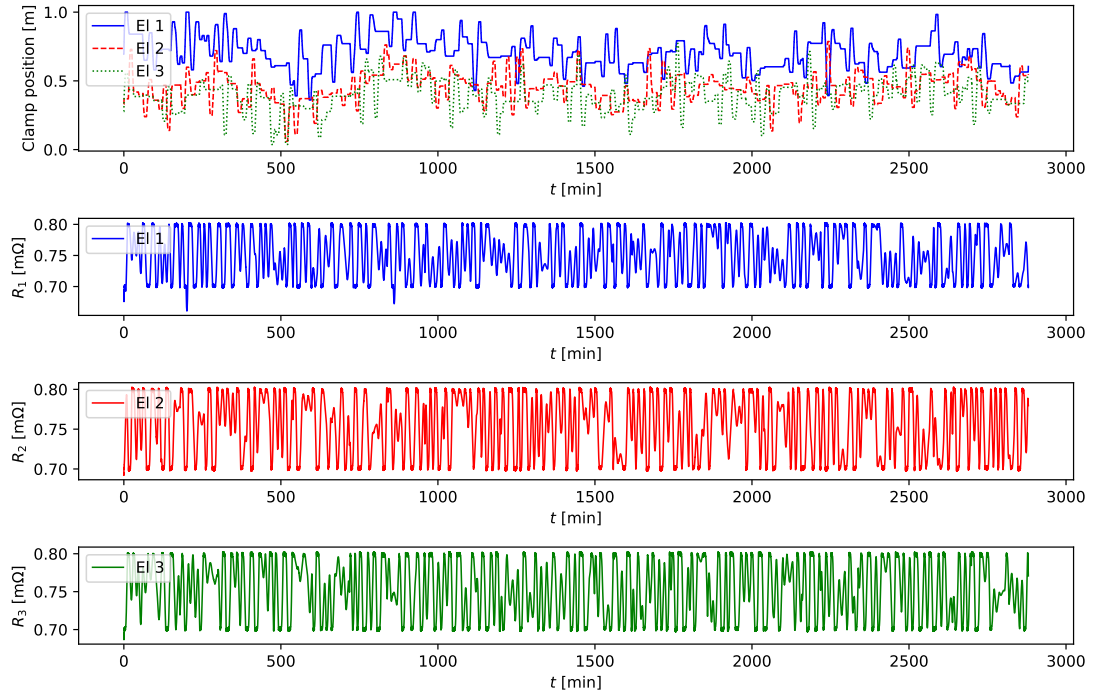
We begin by implementing a resistance control algorithm as described in Sec. 4.4 in the metamodel code, and simulate 48 hours of operation with one second time resolution from a random but realistic starting point. The electrode impedances given as output from this metamodel simulation can be used as input for the circuit model. Figure 8.1 shows the movement of the clamp holders and the resistance of the electrodes during operation, with Fig. 8.1a showing the entire 48 hours of the simulation and Fig. 8.1b zoomed in on the first five hours. The clamp positions often make minor adjustments, and sometimes move in one direction for a longer period of time. The electrodes resistances are mostly kept within their deadband. We see that the times the resistances move significantly outside their deadband is when the clamp holders are already at maximum or minimum height, and therefore cannot move further to bring the resistances inside again.

### 8.1 Interaction effect

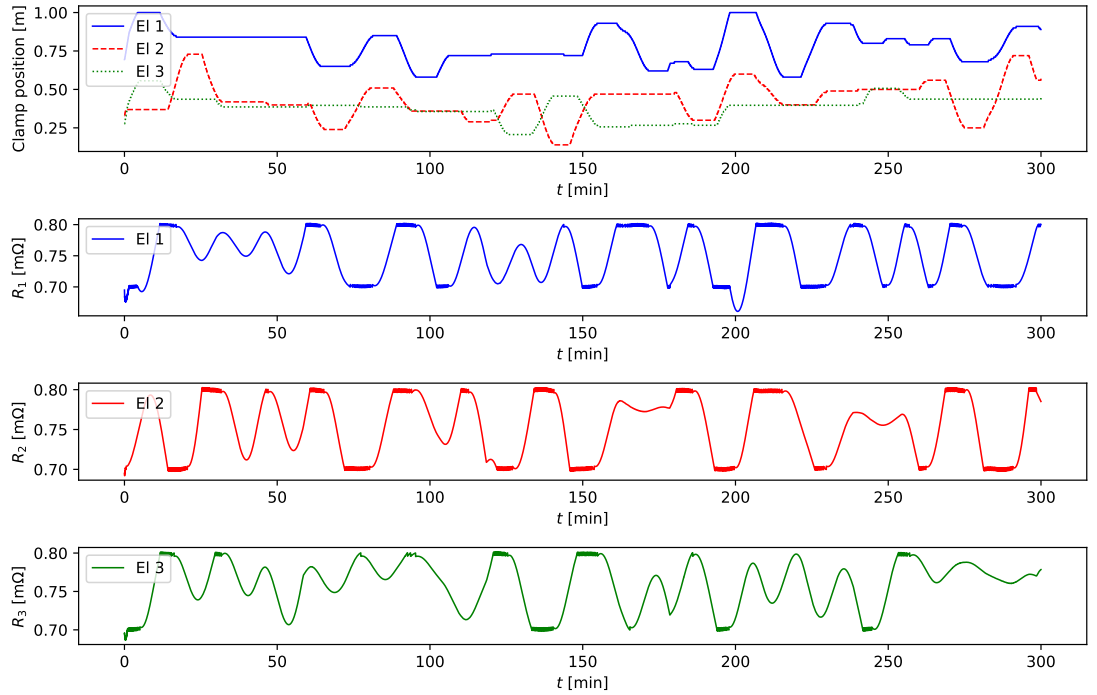
We observe interaction with the resistance controller implemented in the metamodel. Figure 8.2 shows an artificial example where the interaction becomes apparent. We start with balanced conditions and all three electrodes having the same clamp position of  $0.2\text{ m}$ . Then we move electrodes 1 and 2 in steps of  $0.05\text{ m}$ , keep the third electrode stationary, and calculate the resulting resistances. An increased clamp position means that the electrode tip is physically lifted further up in the furnace, as can also be seen by the fact that the resistance increases.

We see that the resistance of the stationary electrode changes when the positions of the other two electrodes change, albeit much less than the resistance of the other two. Note that the resistance of the two moving electrodes differ as well, with electrode 2 having a slightly larger increase in resistance than electrode 1. The slope of each electrode is presented in Tab. 8.1. The stationary electrode has a slope that is 9.2 percent and 8.7 percent that of electrode 1 and 2, respectively. Electrode 1 has a slope that is 94 percent that of electrode 2.

Figure 8.3 shows how the zero sequence component of the electrode voltages changes in this scenario, plotted in the complex plane and with the phase angles of the three electrode voltages marked as well. The calculations are done with voltage phasors found

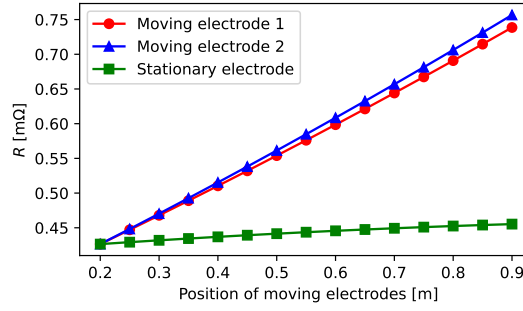


(a) Full 48 hours of simulation.



(b) First five hours of simulation.

Figure 8.1: Clamp positions and electrode resistances from a ferromanganese metamodel simulation of operation with resistance control. The resistance dead-zone is  $0.75 \text{ m}\Omega \pm 0.05 \text{ m}\Omega$  and the clamp positions are limited to between 0 and 1.



**Figure 8.2:** An example of the resistance interaction effect in the metamodel. We move two electrodes together and keep the third electrode stationary. If there was no interaction the resistance of the stationary electrode would be constant.

**Table 8.1:** The slope of the lines in Fig. 8.2, where we move two electrodes in sync and observe the change in resistance for all three electrodes.

	Slope [mΩ/m]
Moving electrode 1	0.446
Moving electrode 2	0.472
Stationary electrode	0.0412

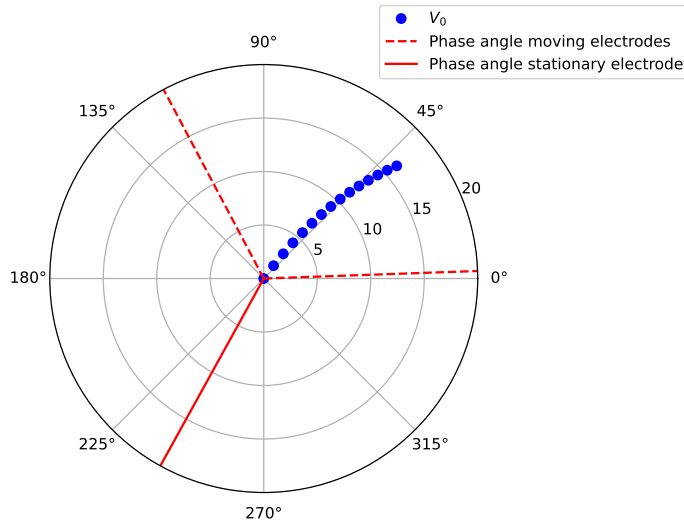
with the circuit model, from calculations using electrode resistance and reactance from the metamodel simulations as input. The innermost point of  $V_0$  is the balanced case, and the absolute value increases as the two electrodes are moved up. The phase angle of the  $V_0$  component is somewhere in between the phase angles of the two moving electrodes, skewed towards the moving electrode with the highest resistance.

## 8.2 Discussion

We must be careful about inferring too much from the behaviour of the control simulation itself over time. This is because the metallurgical effects in the furnace are modelled as random noise in the metamodel. The metamodel simulation therefore does not capture the effect of the electrical conditions on the metallurgical conditions.

As stated by Barker *et al.* [39], the resistance controller should in theory not have an interaction effect, as changing the height of one electrode does not affect the resistance of the other two electrodes. We do however find a resistance interaction in the metamodel. In our example scenario the resistance change in the stationary electrode is slightly below 10 percent the change in the two moving electrodes, and the resistance in the moving electrodes do not change by exactly the same amount. If the model were non-interacting, the stationary electrode would have constant resistance and the two moving electrodes would have exactly the same resistance. Although no efforts have been made at this point to quantify the interaction effect more generally, the example shows that the effect can be large enough to warrant consideration. The resistance of the stationary electrode changes about 0.03 mΩ in total, and given that the width of our dead-zone is 0.1 mΩ, this change represents a realistic possibility of moving the electrode resistance outside of the dead-zone.

One possible explanation for the interaction effect is that it is an artefact of the metamodel. It could be that the metamodel, due to some statistical error, has introduced



**Figure 8.3:** The zero sequence component  $V_0$  of the electrode voltages from the interaction example plotted in the complex plane. The dot in the origin corresponds to the balanced case where  $V_0 = 0$ , and  $V_0$  moves further away from the origin as the two moving electrodes get further away from the stationary electrode. The phase angles of the three electrode voltages are marked with red lines.

the resistance interaction even though it is an unphysical element. There is however a possible physical interpretation. The resistance is calculated based on current and voltage measurements. As explained earlier, the current measurement is straightforward and the voltage measurement, done with the Bøckman technique, is more complicated and prone to errors. The voltage measurement is done with an attachment point at the furnace bottom, thought to be the neutral point or point defined to have zero potential. But as the furnace has a three-dimensional and changing electrical field, the “true” neutral might not be at the measure point. It might on the contrary move around as the furnace geometry changes, for example when electrodes move. This then affects the resistance as we calculate it, and could result in an observed change in electrode resistance, even if the physical resistance in the electrode does not change.

Therefore a possible interpretation of the zero sequence component  $V_0$  is as the deviation from the true neutral. If this is correct, we could subtract  $V_0$  from the electrode voltages to get the true neutral. This means that the true neutral moves further away from the stationary electrode and closer to the moving electrodes when they are lifted higher up in the furnace.

We have made no effort at this point to develop an interaction-free resistance control algorithm, but we here present a suggested route. As seen in Fig. 8.3, and later in Fig. 9.4 for real measurements, there is a significant and changing zero sequence for the symmetrical components of electrode voltage. If we interpret  $V_0$  as an expression of the deviation from the true neutral, we can find the voltage as it would be measured from the true neutral by subtracting  $V_0$  from the real measurements. Our suggestion is that using this corrected voltage to calculate electrode resistance might get rid of the interaction effect, but this would need to be properly tested. For the metamodel, this would probably look like training the model on a data set where the underlying physical model has been corrected for the true neutral.

## Chapter 9

# Measurement comparison

We lastly compare the circuit model to measurement data from a ferrosilicon submerged arc furnace in operation. We have two measurement sets from the same furnace taken several weeks apart. The first set is 3.75 minutes long and the second set is 20 minutes long.

For each set there are two kinds of data. The first is what we will call process data, which contains one second resolution measurements of r.m.s. line to line voltages, r.m.s. electrode voltages, r.m.s. electrode currents, electrode power factors, electrode resistances, total active power, and total reactive power. These measurements are fairly standard. The other kind of data is high-resolution measurement data. It contains instantaneous values for electrode voltages measured with the Bøckman technique, secondary side transformer currents measured with Rogowski spoles, and secondary side transformer voltages. From the transformer currents we can also calculate electrode currents. The sample frequency of these data are 10 kHz, meaning that we have 200 measurements per period when the angular frequency is  $100\pi$ .

### 9.1 Data preprocessing

The high-resolution measurement data has been cleaned before we receive them, so we know that these data sets do not have missing data, but we still need to do some processing before we can compare them to process data and the circuit model. Namely, we need to extract phases and amplitudes from instantaneous measurements, find and apply scaling factors, and choose between sets of overlapping measurements.

#### 9.1.1 Phase and amplitude estimation

We want to extract time series of phases and r.m.s. values from the instantaneous signals. For this we use the Fourier transform, specifically a discrete Fourier transform (DFT) algorithm from `SciPy` [52]. For more details on the Fourier and discrete Fourier transforms, see Appendix C. Given a time signal  $f(t)$ , we denote the complex valued Fourier transform by  $\hat{f}(\omega)$ , where  $\omega$  are angular frequencies. For each  $\omega$  we find the amplitude  $A$  of this frequency by

$$A = |\hat{f}(\omega)| \quad (9.1)$$

and the phase angle  $\phi$  by

$$\phi = \arctan \left( \frac{\text{Im}(\hat{f}(\omega))}{\text{Re}(\hat{f}(\omega))} \right), \quad (9.2)$$

being careful to choose the angle in the correct quadrant. Similarly for the discrete case, let  $\{x_n\}$  be a sequence of points and let  $X_k$  be the discrete Fourier transform of the sequence. The amplitude  $A$  of the frequency  $\omega_k = \frac{2\pi}{T}k$  is then found as

$$A_k = |X_k| \quad (9.3)$$

and the phase angle  $\phi$  is

$$\phi_k = \arctan\left(\frac{\text{Im}(X_k)}{\text{Re}(X_k)}\right). \quad (9.4)$$

We assume that our signal consists of one sinusoidal when seen over a short period of time. Therefore we should have one dominant angular frequency, that is one frequency for which the amplitude is much higher than for all the rest. Even for our discrete signal, the resolution is large enough that we assume we can find the exact frequency with DFT. Let  $k_{\max}$  be the index for which we obtain the maximum amplitude. The amplitude and phase we are looking for are then found by Eqs. (9.3) and (9.4) evaluated at  $k_{\max}$ .

As we want to compare the high-resolution measurement data with measurements that have one second resolution, we divide the whole time series of measurements into one second long sections and do the Fourier transform on each section. This gives us phase and amplitude time series with one second resolution.

### 9.1.2 Scaling

The high-resolution measurements also need scaling. Most scaling factors are provided by the furnace company, but we still need to scale the Rogowski coil currents and the directly measured transformer voltages.

We have two kinds of measurements for the transformer voltages. The first is a direct measurement, the second is transformer voltages calculated from the electrode voltages measured with the Bøckman technique. As the direct measurements have an unknown scaling factor, we use the Bøckman voltage calculations to scale them. The secondary transformer voltages are therefore scaled so that the r.m.s. time series of each transformer has same mean as the r.m.s. voltage time series calculated from Bøckman voltages.

The high-resolution measurements of transformer currents are scaled such that the calculated electrode currents fit the electrode currents from process data. This turns out to be equivalent to scaling the measurements to fit the transformer currents as calculated by the circuit model with process data impedance as input. The scaling factor is thought to be a geometric factor, and should be constant across data sets. Choosing factors based on a few minutes of measurements might therefore lead to overfitting. We choose scaling factors that seem to be a compromise between the two sets of measurements. The approximate range of scaling factors is from 0.7 to 1.2.

### 9.1.3 Choosing which measurements to use

For the Rogowski coils there are two sets of three coils, meaning there are two coils at each transformer that should measure the same current. They are called A1, A2, B1, B2, C1, and C2. We see however that the two options for each transformer follow the same trends, but have different amplitudes and phases. The different amplitudes do not matter, as the measurements need to be scaled to fit process data anyway. C1 is broken. That leaves the combinations A1 B1 C2, A1 B2 C2, A2 B1 C2, and A2 B2 C2. Only the combination A2, B2, C2 gives the correct relative phases, approximately 120° apart from each other. We therefore proceed with this combination.



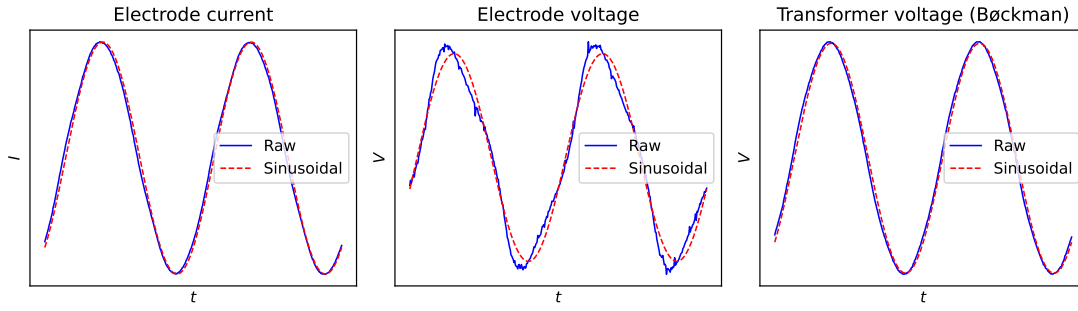


Figure 9.1: Time series of two periods of high-resolution measurement data for current in electrode 1, voltage over electrode 1, and voltage over transformer A calculated from electrode voltages. Both axes are linear.

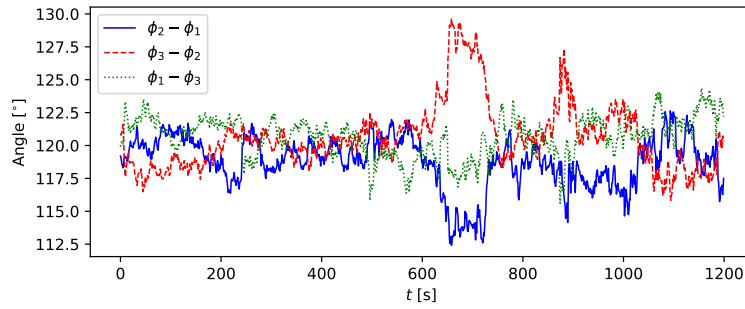


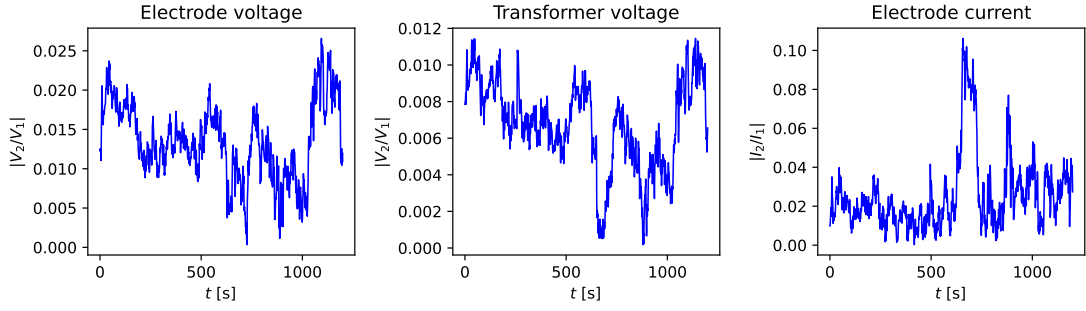
Figure 9.2: Phase differences between the three electrode currents. The phases  $\phi_1$ ,  $\phi_2$ , and  $\phi_3$  are extracted from high-resolution measurement data.

## 9.2 Data exploration

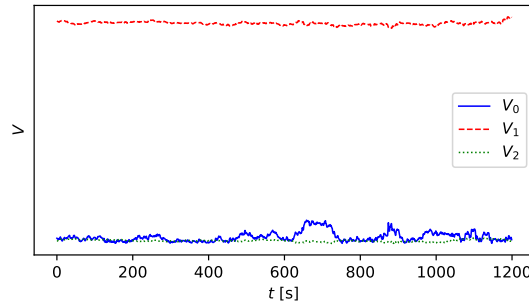
Figure 9.1 shows the two first periods of the current in electrode 1, the voltage in electrode 1, and the voltage in transformer A as calculated from the voltages in electrode 1 and 2, both as measured raw data and as a pure sinusoidal with the r.m.s. value and phase found as described in Sec. 9.1.1. In the left plot of Fig. 9.1 we see that the electrode current is close to a perfect sinusoidal. The electrode voltage however, as seen in the middle plot, has regular oscillations but is clearly not sinusoidal. Interestingly, the voltage over transformer A, calculated as  $V_1 - V_2$  and shown to the right in Fig. 9.1, is close to a perfect sinusoidal even though  $V_1$  and  $V_2$  are not. All quantities except the electrode voltages are close to perfect sinusoids, and we see that our method of extracting phases and amplitudes give sinusoids that line up well with the true signal.

As we can extract phases from high-resolution measurements, we can also look at phase shifts between different parts of the furnace. For example, Fig. 9.2 shows the phase differences between the electrode currents in the data set of 20 minutes. We see that the phase difference varies around  $120^\circ$ , deviating as far as up to  $130^\circ$  or down to  $112^\circ$  at most.

Plots of imbalance calculated as in Eq. (2.28) are shown in Fig. 9.3. The imbalance of the electrode voltage ranges from 0 to 2.5 percent and the imbalance of the transformer voltage ranges from 0 to 1.2 percent. The imbalance of the currents in the electrodes and in the transformers are equal, and higher than the voltage imbalances. It stays between 0 and at most just over 10 percent. The time with the highest current imbalance is the



**Figure 9.3:** Imbalance in high-resolution measurement data, calculated from symmetrical components. The transformer current has exactly the same imbalance as the electrode current and is therefore not shown. Note that the y axes are different for each subplot.



**Figure 9.4:** The absolute value of the symmetrical components for high-resolution electrode voltage measurements. The y axis is linear and starts at 0.

same time for which we see the largest deviation from a phase shift of  $120^\circ$  in Fig. 9.2.

Looking at the absolute values of the zero sequence of symmetrical components gives us interesting information. We recall that the voltage zero sequence component  $V_0$  is defined as

$$V_0 = \frac{1}{3} (V_a + V_b + V_c)$$

and is the constant part of the three phasors  $V_a$ ,  $V_b$ , and  $V_c$ . The same is true for the current zero component  $I_0$ . For the secondary side transformers, this corresponds to the definition of circulating current given in Eq. 4.1. The measurement data has a non-zero  $I_0$  component for transformer currents, with a constant value roughly 4 percent that of the total current. For the electrode currents  $I_0 = 0$ .

There is also a small non-zero zero sequence for the secondary side transformer voltages, with a constant value roughly 0.5 percent that of the total voltage. And lastly, Fig. 9.4 shows the absolute value of the symmetrical components for the electrode voltages. There is a non-zero, varying  $V_0$  component of considerable size, meaning the electrode voltages have a common part that changes over time. The  $V_0$  component is plotted in the complex plane in Fig. 9.5 with the phase angles of the electrode voltages drawn as well, in the same manner as the interaction example in Fig. 8.3. We see that the  $V_0$  phase varies, reaching all angles during the 20 minutes. The absolute value varies as well, with a few notable periods where it is farther from zero.

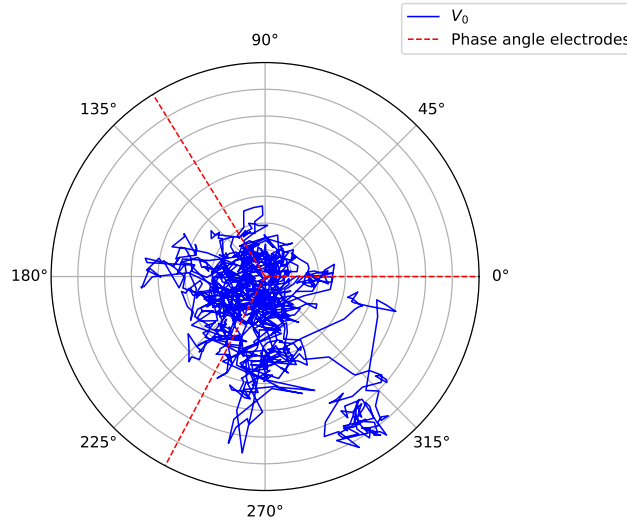


Figure 9.5: The zero sequence component  $V_0$  of electrode voltage from 20 minutes of high-resolution measurement data plotted in the complex plane. The phase angles of the three electrode voltages are marked with red lines. The radial axis is linear.

### 9.3 Comparison

Here we present results for the data set containing 20 minutes of measurements. Results with comparisons of the data set containing 3.75 minutes can be found in Appendix D, but will not be discussed as the general trends are the same.

With the preprocessing done as described above, the high-resolution measurement data and the process data line up well. This can be seen in Fig. 9.6, where we have plotted the r.m.s. values obtained from the high-resolution measurement data and process data together, for current, voltage, and power factor of each electrode. Currents and voltages are scaled to stay between 0 and 1 before plotting, with all currents having the same scaling and all voltages having the same scaling. Both the trends and the absolute values match for electrode voltage and electrode power factor. The trends also match well for electrode currents as seen in the first row, but with a slight difference in absolute value.

Next we compare the high-resolution measurement data with the full circuit model. We solve the circuit model with the electrode resistances from process data and with electrode reactance calculated from resistance and power factor in process data as input. The parameter values from Tab. 6.3 are adjusted to better fit the measurements. We can then compare currents, voltages, and power factors in both the electrodes and the secondary side of the transformers. When presenting the results, all currents and voltages are scaled to lie between 0 and 1, with all currents having the same scaling and all voltages having the same scaling. This is done because the exact measurement data are confidential.

Figure 9.7 shows the results for currents. We see that the circuit model matches the pattern of the measurements very well, but with varying degrees of accuracy in absolute value. The difference is largest in transformer A, followed by electrode 1. Transformer B is the one with a closest match.

The voltage comparison is shown in Fig. 9.8. There are two different measurements for secondary side transformer voltage, direct and calculated based on Bøckman

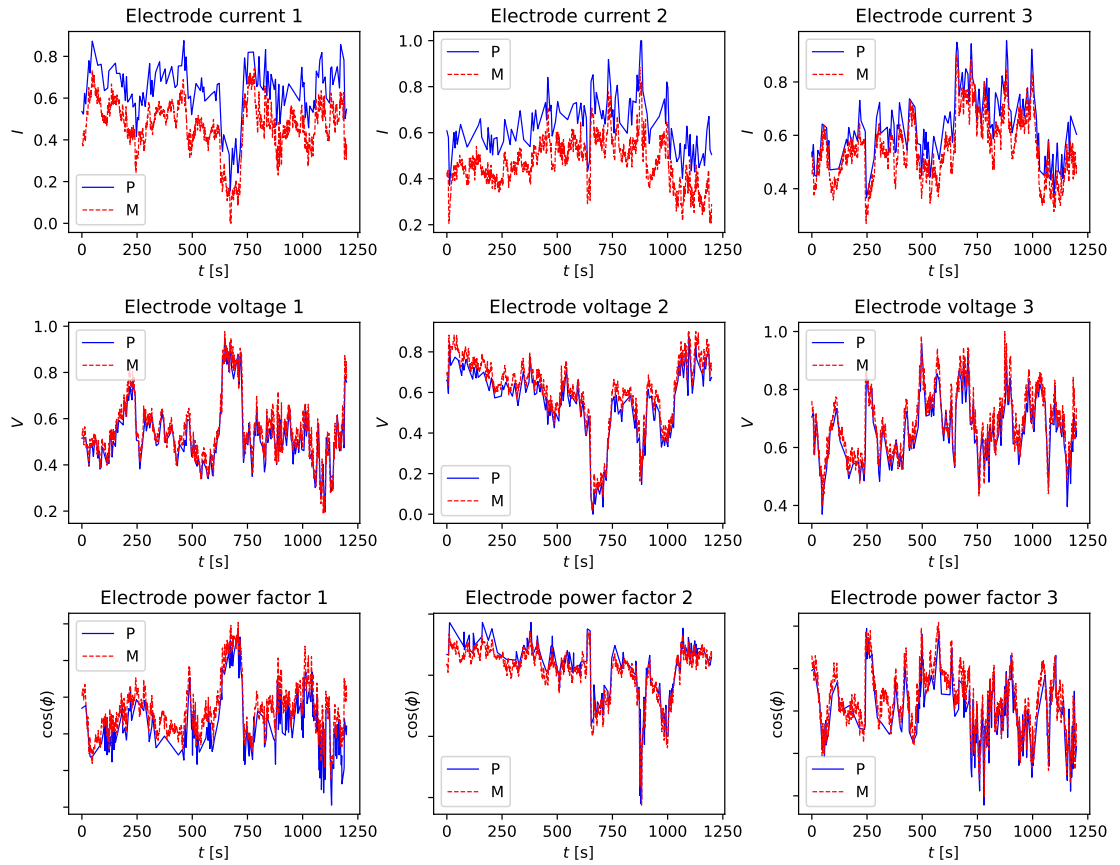


Figure 9.6: Comparison of r.m.s. values from process data and r.m.s. values calculated from high-resolution measurement data for the data set of 20 minutes. Currents and voltages are scaled to lie between 0 and 1, and the y axes of the power factor plots are linear. P stands for process data and M stands for high-resolution measurement data.

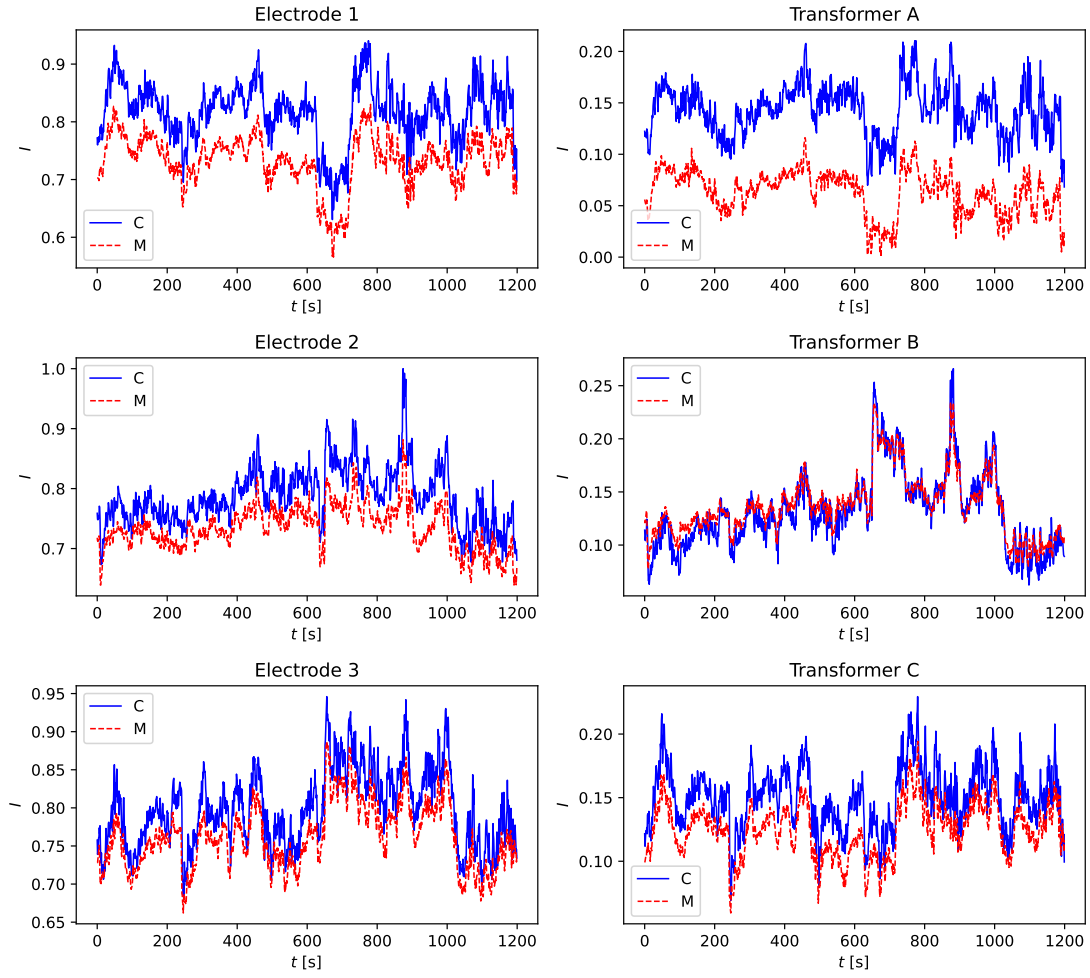
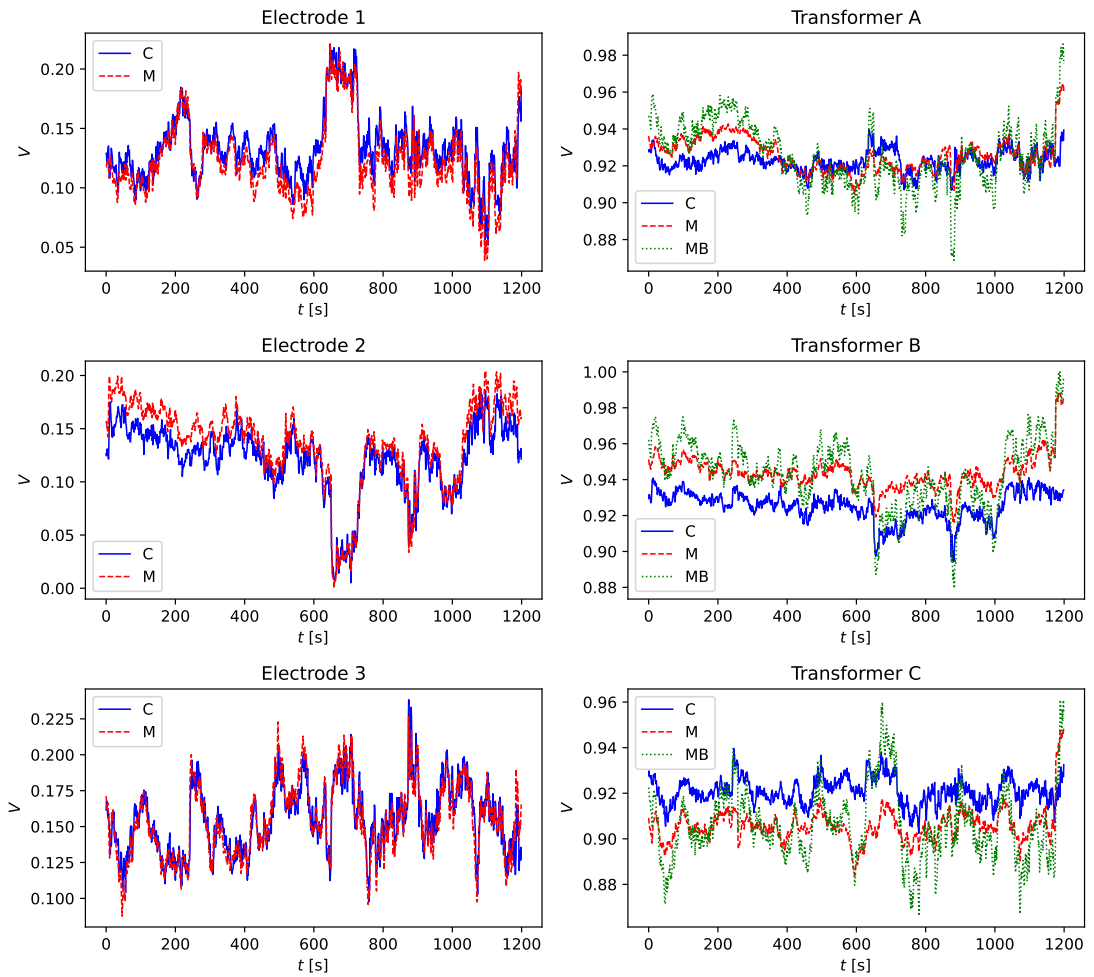


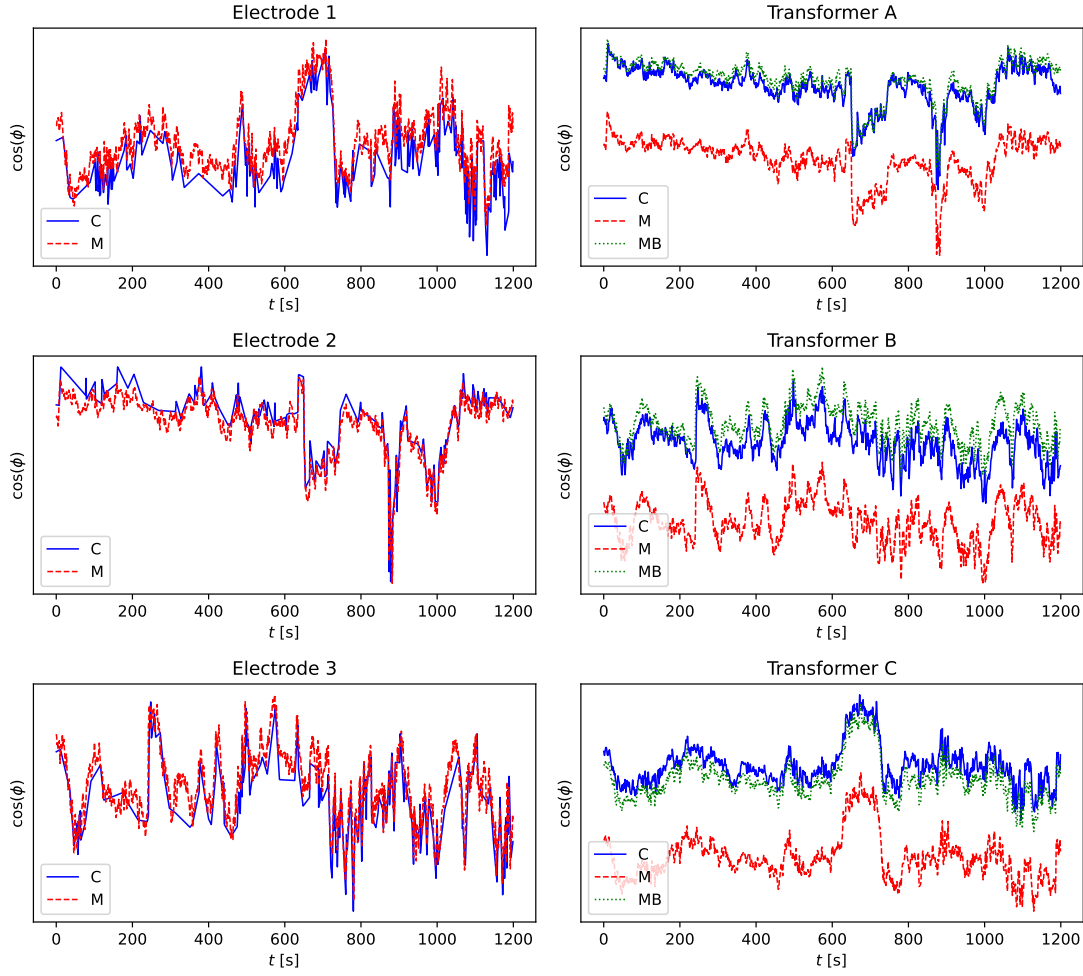
Figure 9.7: Comparison of r.m.s. current values from the full equivalent circuit model *HVC* and r.m.s. current values from high-resolution measurement data for the data set of 20 minutes. The currents are scaled to lie between 0 and 1. C stands for circuit model and M stands for measurement data.



**Figure 9.8:** Comparison of r.m.s. voltage values from the full equivalent circuit model *HVC* and r.m.s. voltage values from high-resolution measurement data for the data set of 20 minutes. The voltages are scaled to lie between 0 and 1. C stands for circuit model, M stands for measurement data, and MB stands for measurement data calculated from Bøckman measurements.

measurements. The electrode voltages match very well, both in pattern and value. For the transformers, we note that the two ways of measuring voltages do not agree with each other. We see that the circuit model does not perfectly match either the direct measurement or the one calculated from electrode voltages, but is closest to the direct measurements. The transformer voltages as calculated from Bøckman measurements jump more up and down than the other two, covering the widest range of values. Both transformer voltage measurements make a jump up at the end of the time series that the circuit model does not capture.

Lastly, Fig. 9.9 shows a comparison of power factors. Here we also have two different ways of measuring secondary side transformer power factors, due to the two different ways of measuring transformer voltages. We see that the electrode power factor from the circuit model has a lower resolution than all the others, but this is a direct consequence of the power factor resolution from the process data. It seems however that the power factor in the electrodes agree well when we take this lower resolution into account, both in pattern and absolute value. For transformers, the pattern of all three power factor time series agree. The power factor as found from Bøckman measurements and



**Figure 9.9:** Comparison of power factor from the full equivalent circuit model *HVC* and power factor from high-resolution measurement data for the data set of 20 minutes. The y axes are linear. C stands for circuit model, M stands for measurement data, and MB stands for measurement data calculated from Bøckman measurements.

calculated with the circuit model additionally agree in absolute value, making Bøckman measurements and the circuit model a very good match overall. The direct measurement power factor is shifted to be lower for all three transformers.

Table 9.1 shows the r.m.s. errors of the circuit model compared to the high-resolution measurement data after we have applied scaling to currents and voltages such that they range from 0 to 1. That is, the error is calculated as

$$\frac{1}{n} \sqrt{\sum_{i=1}^n (x_i - y_i)^2} \quad (9.5)$$

where  $x_i$  are the points from the scaled high-resolution measurements,  $y_i$  are the points from the scaled circuit model calculations, and  $n$  is the number of points. We see that  $I_1$ ,  $I_2$ ,  $I_3$ ,  $I_A$ ,  $\cos \phi_A$ ,  $\cos \phi_B$ , and  $\cos \phi_C$  have errors of order  $10^{-3}$  and the rest of the quantities have errors of order  $10^{-4}$ .

**Table 9.1:** R.m.s. error of values calculated with the full circuit model compared to high-resolution measurement data. All currents and voltages have been scaled to lie between 0 and 1 before calculating the error.

Electrodes		Transformers		Transformers (Bøckman)	
Quantity	Error	Quantity	Error	Quantity	Error
$I_1$	$2.486 \cdot 10^{-3}$	$I_A$	$2.330 \cdot 10^{-3}$	—	—
$I_2$	$1.641 \cdot 10^{-3}$	$I_B$	$3.555 \cdot 10^{-4}$	—	—
$I_3$	$1.171 \cdot 10^{-3}$	$I_C$	$7.758 \cdot 10^{-4}$	—	—
$V_1$	$4.258 \cdot 10^{-4}$	$V_A$	$2.515 \cdot 10^{-4}$	$V_{A,Bok}$	$4.251 \cdot 10^{-4}$
$V_2$	$5.312 \cdot 10^{-4}$	$V_B$	$5.710 \cdot 10^{-4}$	$V_{B,Bok}$	$6.383 \cdot 10^{-4}$
$V_3$	$2.871 \cdot 10^{-4}$	$V_C$	$4.888 \cdot 10^{-4}$	$V_{C,Bok}$	$5.531 \cdot 10^{-4}$
$\cos \phi_1$	$2.947 \cdot 10^{-4}$	$\cos \phi_A$	$1.979 \cdot 10^{-3}$	$\cos \phi_{A,Bok}$	$2.398 \cdot 10^{-4}$
$\cos \phi_2$	$2.336 \cdot 10^{-4}$	$\cos \phi_B$	$1.518 \cdot 10^{-3}$	$\cos \phi_{B,Bok}$	$4.013 \cdot 10^{-4}$
$\cos \phi_3$	$2.169 \cdot 10^{-4}$	$\cos \phi_C$	$2.322 \cdot 10^{-3}$	$\cos \phi_{C,Bok}$	$3.847 \cdot 10^{-4}$

## 9.4 Discussion

The process data and the high-resolution measurement data are shown to be in good agreement, as seen in Fig. 9.6. Together with the comparison in Fig. 9.1, this shows us that our chosen method of extracting phases and amplitudes from the high-resolution measurement data works well. The internal consistency between the two types of measurements also serves as a good test for both of them. There are however still some unanswered questions regarding the measurements.

First, the three sets of two Rogowski coils should give the same measurements. We were able to resolve the issue by choosing a set of internally consistent coils, but the question still remains of why they give different measurements in the first place. We also see that we need slightly different scaling factors for the Rogowski coil measurements to perfectly fit with the two data sets. The scaling factor is believed to be a geometric factor and therefore should be constant even for measurements made weeks or months apart. As our data sets cover only a short period of time, 3.75 and 20 minutes, one possible explanation is that there are slight disagreements between the high-resolution measurements and the process data, and that choosing scaling factors so that they perfectly match for one short time periods is a type of overfitting.

For this thesis we have simply guessed Rogowski coil scaling factors that compromise between the data sets as well as possible. However, to better understand the effect of scaling factors we should preferably compare more and longer data sets. Choosing scaling factors can probably be done more rigorously, by some optimisation process that balances the fit of each data set. We could probably do such an optimisation on enough data sets to arrive at a standard scaling factor we believe to be as close to the true geometric factor as possible, but have not done so at this stage.

From the symmetrical components we find that there is a circulating current in the transformer delta. This is about the same fraction as the estimate from [34], where they found a circulating current of about 4 percent of the total current. According to the analytical solutions in Sec. 5.1, there should only be a non-zero circulating current on the secondary side delta if the transformers are unbalanced, and specifically unbalanced electrodes do not lead to a circulating current. So in order to be in agreement with our theoretical results, either the voltage supply or the transformers themselves must be



unbalanced. All real systems are unbalanced, and it is plausible that the effect should be noticeable. However, our theoretical results are based on a very simplified secondary side circuit model, and it might also be that the theoretical results would be different if we had a more complex model. The fact that  $V_0 = 0$  for the electrode currents is as it should be, since the sum of the electrode currents entering the wye connection must be zero due to charge conservation.

We can interpret the zero sequence component of the electrode voltage as a deviation from the “true” neutral point as discussed in Sec. 8.2. If desired, we can therefore use the  $V_0$  component to adjust the electrode voltage measurements to be taken from this changing true neutral. However, we know that Bøckman measurements are prone to errors and must therefore be careful about trusting these measurements too much.

It is important to note that we in general do not know much about the uncertainties in the measurements themselves. It is a good sign that the process data and high-frequency measurements agree as well as they do, but ideally we would like to be able to say something more precise about the measurement errors. For now however, we can only say that this is an unknown source of error.

From our comparison of high-resolution measurement data to the circuit model, the general picture is that they fit well in both patterns and absolute value, as seen in Figs. 9.7, 9.8, and 9.9, and in Tab. 9.1. In Fig. 9.7 we see that  $I_A$  has larger error than  $I_C$ , which in turn has larger error than  $I_B$  due to the choice of scaling factor. Choosing a better scaling factor for the data set shown would have resulted in larger errors for the other data set. We note that this affects the errors of electrode current as well, with  $I_1 = I_C - I_A$  having the largest error of the three, and  $I_3 = I_B - I_C$  having the smallest error. But even with the differing scaling factors, the pattern of all currents fit well.

We see the poorest pattern match for transformer voltages in Fig. 9.8, both between measurements and the circuit model, but also between the direct measurement and the voltage calculated from Bøckman measurements. We do not have a good explanation for the differences between the two measurement methods. The poorer fit with the circuit model might possibly have something to do with how we model the transformer, by lumping all the resistance and leakage flux on the secondary side. But as we have not tested other transformer models, we cannot conclude at this stage. The jump at the end of the measured transformer voltages could be due to the operators changing the transformer windings ratio, but this have not been confirmed either way.

For transformer power factor in Fig. 9.9, we see a good pattern match between both measurements and the circuit model, but the direct measurements are shifted to lower values. This is due to a phase shift of roughly  $5^\circ$  to  $7^\circ$  between the direct voltage measurement and the voltage as calculated from Bøckman measurements. The fact that Bøckman measurements give the best fit here is probably because we use electrode impedance from process data, which are calculated based on Bøckman measurements of electrode voltage, as input to the circuit model. That the circuit model therefore most closely resembles calculations based on Bøckman voltage measurements in other parts of the system is not surprising.

We see in the middle plot in Fig. 9.1 that the electrode voltage is periodic but non-sinusoidal. This is the effect of arcing, and means that this part of the circuit is non-linear. Our circuit model works under the assumption that everything is linear, so this is a source of error in our model, but as seen in Tab. 9.1 the errors in r.m.s. value and power factor are still small. For the furnace under consideration it therefore seems like a linear system is a good approximation, able to capture most of the system’s behaviour.

The fact that the circuit model fits measurement data as well as it does, especially the patterns, indicates that it is mostly a good representation of the electrical behaviour of the furnace and supply system. This in turn gives more credibility to the other results we have found by use of the circuit model, as agreement in the case we can check makes the numerical experiments we cannot easily check more trustworthy as well. There are however specific areas where the circuit model performs worse, particularly it cannot capture the non-linear behaviour of the electrode voltages and is a poorer match for secondary side transformer voltages than for the other measurements. We must also remember that we treat the measurements as the truth to which the circuit model is compared, but the measurements themselves can contain errors.

## Chapter 10

# Conclusion

### 10.1 Summary

In this thesis we have set up circuit models of the primary side representing the supply system, the secondary side representing the furnace, and a full circuit model of the entire system, the last of which is a new approach. We have implemented and verified a numerical solver for harmonic circuit problems in general and the circuits under consideration in particular. The numerical solver was then used as a tool to study the combined supply and furnace system.

We used an equivalent circuit model of a furnace system with the fairly novel setup of low-voltage compensation to study the behaviour of the circuit as a function of capacitance, and compared it to the more standard setup of high-voltage compensation. Our results agree with previous literature on LVC, showing that LVC has the advantage of improving the power factor of the transformers in addition to the grid power factor. This means that with low-voltage compensation, the transformers can deliver the same amount of active power with a lower apparent power and lower currents running in the grid connection and through the transformers. We also estimated the currents and voltages that the capacitors would be subjected to, hopefully providing a better foundation for experts to evaluate the method's potential usefulness and effectiveness. We found the ratio between several HVC and LVC values as a function of winding ratios in the transformers to be polynomial functions, and we thus have a method for calculating LVC values if we know the corresponding HVC values.

When using the previously developed metamodel to simulate a furnace running with resistance control, we observed that the model has an interaction effect on the resistances, even though literature reports that there should not be one. In our example the resistance of the stationary electrode changed about 9 percent as much as the resistance of the two moving electrodes, which is a considerable amount. We suggested that the uncertain measurements of electrode voltage due to a moving neutral point might be the cause of the observed interaction. More research is however needed to conclusively find the source of and properly quantify the interaction effect.

Lastly, we compared the numerical circuit model with high-resolution measurements from a real ferrosilicon furnace in operation. Our circuit model agreed well with the measurements, with transformer voltages being a slight exception. The r.m.s. errors are order  $10^{-3}$  and  $10^{-4}$  after scaling, showing that we are able to capture both the patterns and absolute value of the system to a good degree even with this simplified model where we have disregarded non-linear elements and higher harmonics. We conclude that for this ferrosilicon furnace the circuit model is correct enough to be a useful tool, and

the nonlinearity of the arcs do not distort the system enough to pose a serious error. This also gives credibility to our other results. Building on the results presented in this thesis, the circuit models and numerical solver can be used for looking at the overarching electrical behaviour of the system, either in real time or by carrying out experiments we are unable or unwilling to conduct on a real furnace.

### 10.2 Future work


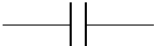
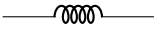
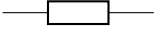

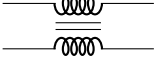
As there are aspects of the furnace and supply system our model did not capture well, notably the secondary side transformer voltage, we could try to develop and implement more complicated circuit models to improve the accuracy. One possibility is to use more sophisticated circuit models to represent the transformers. Another approach is to create a model with non-linear elements to include arcing, which would also require implementation of a non-harmonic numerical solver. However, for the ferrosilicon furnace we get good electrode results even with a linear model. Perhaps more interesting would be to develop a non-harmonic solver for use on transient signals, signals that vary over time. That way we could use the circuit model to simulate what happens during startup and shutdown of the furnace. We could also use the circuit model to study higher harmonics, even without introducing a non-linear element, as that would still fit within the constraints of our harmonic solver.

Given access to measurements from other submerged arc furnaces, we could find out how well the simplified equivalent circuit model works for those as well. We should do this before using the circuit model to draw conclusions about other types of furnaces, as for example the effect of arcing will be different for different materials. There are also unanswered questions about the measurements themselves, that could be investigated further. For example making a more informed choice of Rogowski measurements and scaling factors, and investigating whether the direct measurements or calculated measurements for transformers are more correct.

Lastly it would be interesting to follow up on the resistance interaction effect, investigating why it appears, how large it is, in which scenarios it is most prominent, and to what degree it is harmful by for example causing excessive electrode movement. We could also try to implement a non-interacting resistance controller, for instance by adjusting the Bøckman voltage measurements to the true neutral point using symmetrical components.

## Appendix A

# Circuit diagram symbols

	Resistor
	Capacitor
	Inductor
	General component with impedance
	Sinusoidal voltage source
	Ideal transformer



## Appendix B

### Analytical current solutions

We here present current solutions for the primary side equation (5.8) with different unbalanced elements. The current solutions for the primary side with unbalanced capacitors are presented in Eq. B.1, where we have defined  $Z_{xy} = Z_{C1}Z_{C2} + Z_{C1}Z_{C3} + Z_{C2}Z_{C3}$ ,  $Z_x = Z_{C1} + Z_{C2} + Z_{C3}$ , and

$$\alpha = 27Z^4 + 18Z^3(2Z_x + Z_t) + 3Z^2(12Z_{xy} + 6Z_tZ_x + Z_t^2) + 2ZZ_t(6Z_{xy} + Z_tZ_x) + Z_t^2Z_{xy}.$$

The current solutions of the primary side with unbalanced transformers are presented in Eq. B.2, where we have defined  $Z_{xy} = Z_{p1}Z_{p3} + Z_{p1}Z_{p2} + Z_{p3}Z_{p2}$ ,  $Z_x = Z_{p1} + Z_{p3} + Z_{p2}$ , and

$$\begin{aligned} \alpha = & 3Z^4Z_x + 2Z^3(Z_{xy} + 6Z_CZ_x) + Z^2(Z_{p1}Z_{p3}Z_{p2} + 6Z_CZ_{xy} + 12Z_C^2Z_x) \\ & + 2ZZ_C(Z_{p1}Z_{p3}Z_{p2} + 2Z_CZ_{xy}) + Z_{p1}Z_{p3}Z_{p2}Z_C^2. \end{aligned}$$

$$\begin{aligned}
 & \begin{bmatrix} I_1 \\ I_2 \\ I_3 \\ I_4 \\ I_5 \\ I_6 \\ I_7 \\ I_8 \\ I_9 \\ I_{10} \\ I_{11} \\ I_{12} \end{bmatrix} = \frac{1}{\alpha} \begin{bmatrix} V_1(27Z^3 + 9Z^2(3Z_x - Z_{C1} + 2Z_t) + Z(18Z_{xy} + 6Z_t(2Z_x - Z_{C1}) + 3Z_t^2) + 3Z_tZ_{xy} + Z_t^2(Z_{C2} + Z_{C3})) - (V_2Z_{C3} + V_3Z_{C2})(3Z + Z_t)^2 \\ V_2(27Z^3 + 9Z^2(3Z_x - Z_{C2} + 2Z_t) + Z(18Z_{xy} + 6Z_t(2Z_x - Z_{C2}) + 3Z_t^2) + 3Z_tZ_{xy} + Z_t^2(Z_{C1} + Z_{C3})) - (V_1Z_{C3} + V_3Z_{C1})(3Z + Z_t)^2 \\ V_3(27Z^3 + 9Z^2(3Z_x - Z_{C3} + 2Z_t) + Z(18Z_{xy} + 6Z_t(2Z_x - Z_{C3}) + 3Z_t^2) + 3Z_tZ_{xy} + Z_t^2(Z_{C1} + Z_{C2})) - (V_1Z_{C2} + V_2Z_{C1})(3Z + Z_t)^2 \\ 3V_1(6Z^2Z_{C1} + 2Z(3Z_{xy} + Z_{C1}Z_t) + Z_tZ_{xy}) - 3Z(V_2Z_{C2} + V_3Z_{C3})(3Z + Z_t) \\ 3V_2(6Z^2Z_{C2} + 2Z(3Z_{xy} + Z_{C2}Z_t) + Z_tZ_{xy}) - 3Z(V_1Z_{C1} + V_3Z_{C3})(3Z + Z_t) \\ 3V_3(6Z^2Z_{C3} + 2Z(3Z_{xy} + Z_{C3}Z_t) + Z_tZ_{xy}) - 3Z(V_1Z_{C1} + V_2Z_{C2})(3Z + Z_t) \\ V_1(27Z^3 + 18Z^2(Z_{C2} + Z_{C3} + Z_t) + 3ZZ_t(3Z_{C2} + 3Z_{C3} + Z_t) + Z_t^2(Z_{C2} + Z_{C3})) - (V_2Z_{C3} + V_3Z_{C2})(18Z^2 + 9ZZ_t + Z_t^2) \\ V_2(27Z^3 + 18Z^2(Z_{C1} + Z_{C3} + Z_t) + 3ZZ_t(3Z_{C1} + 3Z_{C3} + Z_t) + Z_t^2(Z_{C1} + Z_{C3})) - (V_1Z_{C3} + V_3Z_{C1})(18Z^2 + 9ZZ_t + Z_t^2) \\ V_3(27Z^3 + 18Z^2(Z_{C1} + Z_{C2} + Z_t) + 3ZZ_t(3Z_{C1} + 3Z_{C2} + Z_t) + Z_t^2(Z_{C1} + Z_{C2})) - (V_1Z_{C2} + V_2Z_{C1})(18Z^2 + 9ZZ_t + Z_t^2) \\ -V_1(9Z^2Z_{C1} + Z_{xy}(6Z + Z_t) + 3ZZ_{C1}Z_t) + V_2(9Z^2Z_{C2} + Z_{xy}(6Z + Z_t) + 3ZZ_{C2}Z_t) \\ V_1(9Z^2Z_{C1} + Z_{xy}(6Z + Z_t) + 3ZZ_{C1}Z_t) - V_3(9Z^2Z_{C3} + Z_{xy}(6Z + Z_t) + 3ZZ_{C3}Z_t) \\ -V_2(9Z^2Z_{C2} + Z_{xy}(6Z + Z_t) + 3ZZ_{C2}Z_t) + V_3(9Z^2Z_{C3} + Z_{xy}(6Z + Z_t) + 3ZZ_{C3}Z_t) \end{bmatrix} \quad (\text{B.1}) \\
 \\
 & \begin{bmatrix} I_1 \\ I_2 \\ I_3 \\ I_4 \\ I_5 \\ I_6 \\ I_7 \\ I_8 \\ I_9 \\ I_{10} \\ I_{11} \\ I_{12} \end{bmatrix} = \frac{1}{\alpha} \begin{bmatrix} V_1(3ZZ_x(Z^2 + 3ZZ_C + 2Z_t^2) + 2ZZ_{xy}(Z + 2Z_C) + Z_{p1}Z_{p3}Z_{p2}(Z + Z_C) + Z_{p1}Z_{p2}Z_C^2 + Z_{p3}Z_{p2}Z_C^2) - (V_2Z_{p3} + V_3Z_{p1})Z_{p2}Z_C^2 \\ V_1(3ZZ_x(Z^2 + 3ZZ_C + 2Z_t^2) + 2ZZ_{xy}(Z + 2Z_C) + Z_{p1}Z_{p3}Z_{p2}(Z + Z_C) + Z_{p1}Z_{p2}Z_C^2 + Z_{p3}Z_{p2}Z_C^2) - (V_1Z_{p2} + V_3Z_{p1})Z_{p3}Z_C^2 \\ V_3(3ZZ_x(Z^2 + 3ZZ_C + 2Z_t^2) + 2ZZ_{xy}(Z + 2Z_C) + Z_{p1}Z_{p3}Z_{p2}(Z + Z_C) + Z_{p1}Z_{p2}Z_C^2 + Z_{p3}Z_{p2}Z_C^2) - (V_1Z_{p2} + V_2Z_{p3})Z_{p1}Z_C^2 \\ V_1(3ZZ_CZ_x(Z + 2Z_C) + ZZ_{p1}Z_{p2}Z_C + ZZ_{p3}Z_{p2}Z_C + Z_{p1}Z_{p2}Z_C^2 + Z_{p3}Z_{p2}Z_C^2) - (V_2Z_{p3} + V_3Z_{p1})Z_{p2}Z_C(Z + Z_C) \\ V_2(3ZZ_CZ_x(Z + 2Z_C) + ZZ_{p1}Z_{p3}Z_C + ZZ_{p3}Z_{p2}Z_C + Z_{p1}Z_{p3}Z_C^2 + Z_{p3}Z_{p2}Z_C^2) - (V_1Z_{p2} + V_3Z_{p1})Z_{p3}Z_C(Z + Z_C) \\ V_3(3ZZ_CZ_x(Z + 2Z_C) + ZZ_{p1}Z_{p3}Z_C + ZZ_{p3}Z_{p2}Z_C + Z_{p1}Z_{p3}Z_C^2 + Z_{p1}Z_{p2}Z_C^2) - (V_1Z_{p2} + V_2Z_{p3})Z_{p1}Z_C(Z + Z_C) \\ V_1(3Z^2Z_x(Z + 2Z_C) + 2Z^2Z_{xy} + ZZ_{p1}Z_{p3}Z_{p2} + Z_{p1}Z_{p3}Z_{p2}Z_C + 2ZZ_C(Z_{p1}Z_{p3} + Z_{xy})) - (V_2Z_{p1} + V_3Z_{p3})ZZ_{p2}Z_C \\ V_2(3Z^2Z_x(Z + 2Z_C) + 2Z^2Z_{xy} + ZZ_{p1}Z_{p3}Z_{p2} + Z_{p1}Z_{p3}Z_{p2}Z_C + 2ZZ_C(Z_{p1}Z_{p2} + Z_{xy})) - (V_1Z_{p1} + V_3Z_{p2})ZZ_{p3}Z_C \\ V_3(3Z^2Z_x(Z + 2Z_C) + 2Z^2Z_{xy} + ZZ_{p1}Z_{p3}Z_{p2} + Z_{p1}Z_{p3}Z_{p2}Z_C + 2ZZ_C(Z_{p3}Z_{p2} + Z_{xy})) - (V_1Z_{p3} + V_2Z_{p2})ZZ_{p1}Z_C \\ -V_1Z_C(3Z^2Z_{p3} + ZZ_{p3}Z_{p2} + 6ZZ_{p3}Z_C + Z_{p3}Z_{p2}Z_C) + V_2Z_C(3Z^2Z_{p2} + ZZ_{p3}Z_{p2} + 6ZZ_{p2}Z_C + Z_{p3}Z_{p2}Z_C) \\ V_1Z_C(3Z^2Z_{p1} + ZZ_{p1}Z_{p2} + 6ZZ_{p1}Z_C + Z_{p1}Z_{p2}Z_C) - V_3Z_C(3Z^2Z_{p2} + ZZ_{p1}Z_{p2} + 6ZZ_{p2}Z_C + Z_{p1}Z_{p2}Z_C) \\ -V_2Z_C(3Z^2Z_{p1} + ZZ_{p1}Z_{p3} + 6ZZ_{p1}Z_C + Z_{p1}Z_{p3}Z_C) + V_3Z_C(3Z^2Z_{p3} + ZZ_{p1}Z_{p3} + 6ZZ_{p3}Z_C + Z_{p1}Z_{p3}Z_C) \end{bmatrix} \quad (\text{B.2})
 \end{aligned}$$



## Appendix C

# The Fourier and discrete Fourier transforms

Any integrable continuous function can, for our purposes, be represented as a sum or integral of complex harmonic functions [53]. The Fourier transform takes an integrable function as argument and returns this alternative representation. Consider an integrable, continuous complex-valued function  $f(t)$  with domain in the real numbers,  $t \in \mathbb{R}$ . The Fourier transform  $\hat{f}(\omega)$  of this function is

$$\hat{f}(\omega) = \frac{1}{2\pi} \int_{-\infty}^{\infty} f(t) e^{-j\omega t} dt, \quad \omega \in \mathbb{R}, \quad (\text{C.1})$$

where  $j$  is the imaginary unit [53]. If the function argument  $t$  is time,  $\omega$  represents the angular frequency. We can say that the Fourier transform takes us from the time domain to the angular frequency domain. The Fourier transform  $\hat{f}(\omega)$  tells us how much of a harmonic signal with angular frequency  $\omega$  is present in the original signal  $f(t)$ . The inverse Fourier transform is given by [53]

$$f(t) = \int_{-\infty}^{\infty} \hat{f}(\omega) e^{j\omega t} d\omega, \quad t \in \mathbb{R}. \quad (\text{C.2})$$

Note that both  $f(t)$  and  $\hat{f}(\omega)$  can be complex.

When we only have a finite number of sample points to describe our function, we instead use a discrete Fourier transform (DFT). The basic DFT assumes that the sample points are evenly spaced. Given a sequence  $\{x_n\}_{n=0}^{N-1}$  of  $N$  sample points, the DFT is

$$X_k = \frac{1}{N} \sum_{n=0}^{N-1} x_n e^{-2\pi jkn/N}, \quad k = 0, 1, \dots, N-1. \quad (\text{C.3})$$

The frequency corresponding to the Fourier coefficient  $X_k$  is  $\omega_k = \frac{2\pi}{T}k$  [53]. We note that for a sample of size  $N$ , we only get Fourier coefficients for  $N$  discrete frequencies. The inverse discrete Fourier transform is [53]

$$x_n = \sum_{k=0}^{N-1} X_k e^{2\pi jkn/N}, \quad n = 0, 1, \dots, N-1. \quad (\text{C.4})$$

In practice a discrete Fourier transform is always used when working with numerics, as computers work with a finite amount of discrete points and not symbolic representations of a function. Implementations commonly use variations of an algorithm called the fast Fourier transform (FFT) for computing the DFT of a sequence, and this is true for SciPy as well [54].



## Appendix D

### Results for second data set

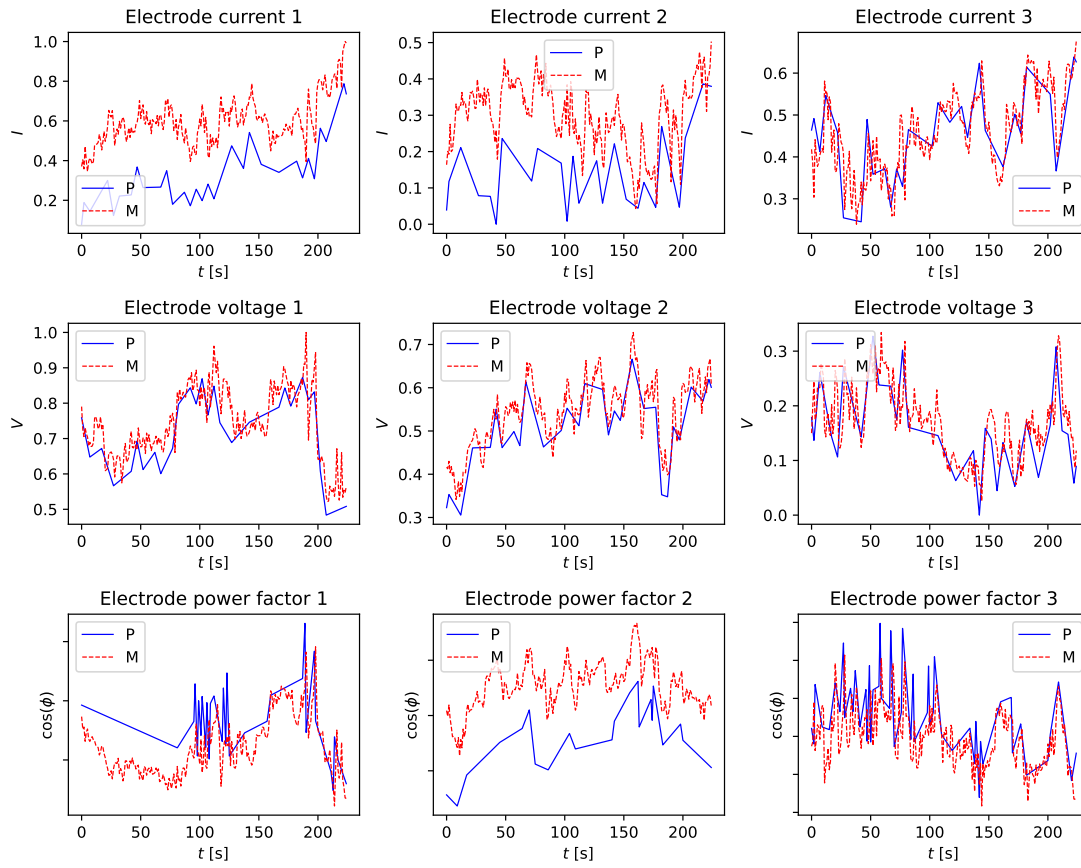


Figure D.1: Comparison of r.m.s. values from process data and r.m.s. values calculated from high-resolution measurement data for the data set of 3.75 minutes. Currents and voltages are scaled to lie between 0 and 1, and the y axes of the power factor plots are linear. P stands for process data and M stands for high-resolution measurement data.

## Appendix D. Results for second data set

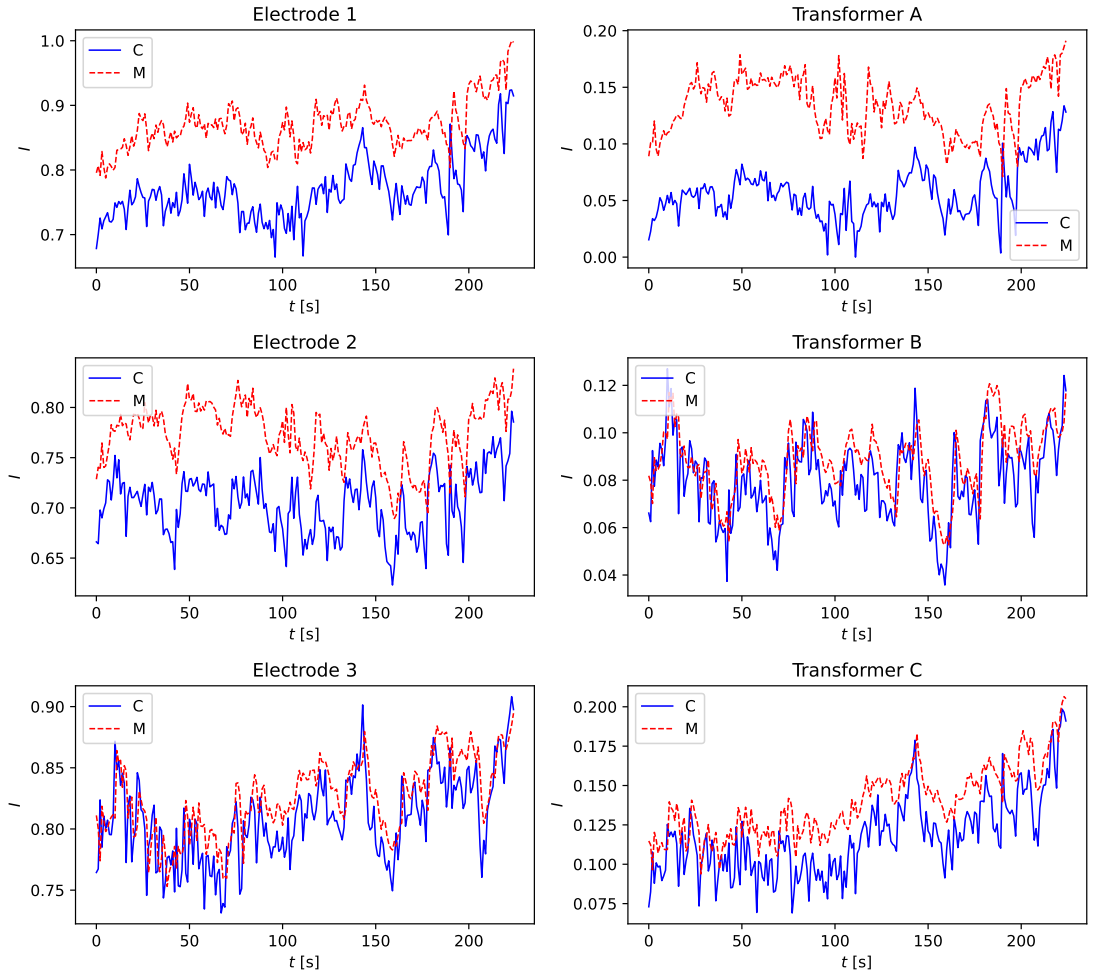


Figure D.2: Comparison of r.m.s. current values from the full equivalent circuit model *HVC* and r.m.s. current values from high-resolution measurement data for the data set of 3.75 minutes. The currents are scaled to lie between 0 and 1. C stands for circuit model and M stands for measurement data.

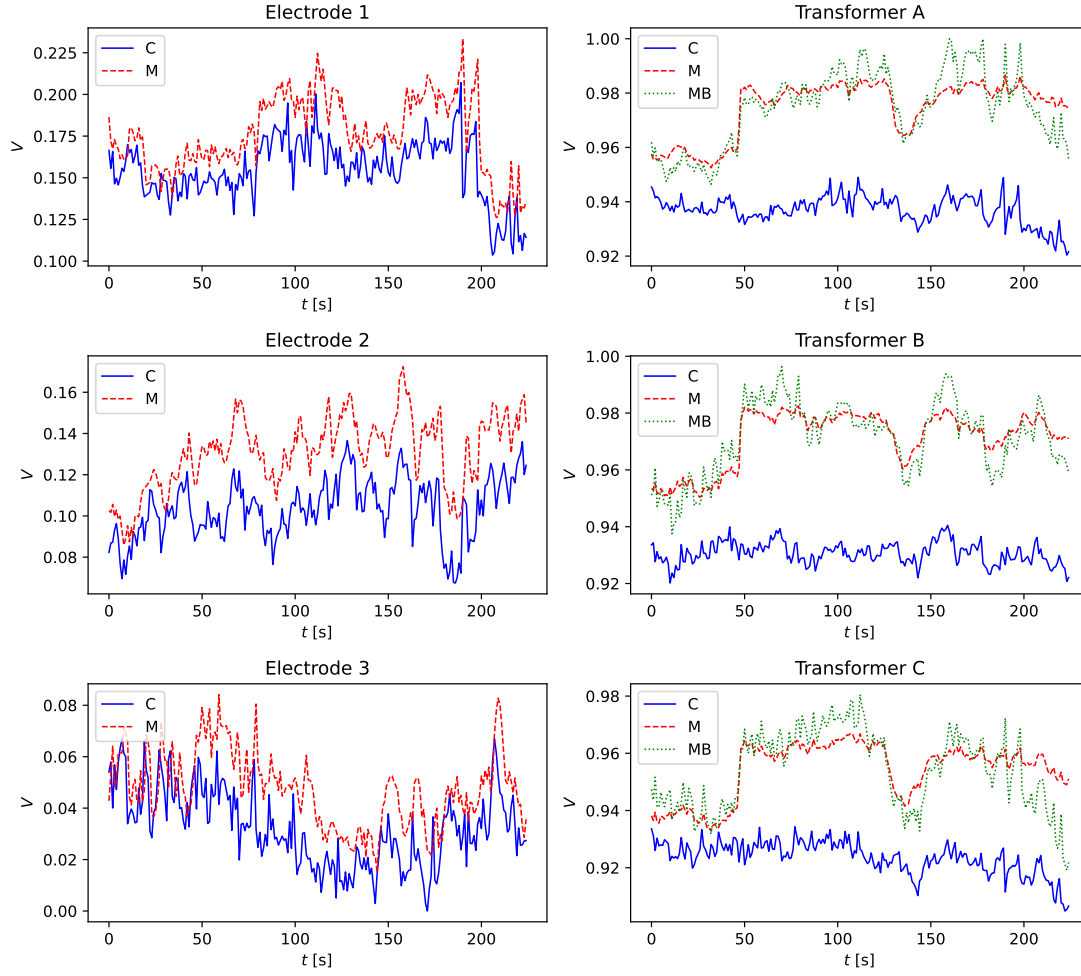


Figure D.3: Comparison of r.m.s. voltage values from the full equivalent circuit model *HVC* and r.m.s. voltage values from high-resolution measurement data for the data set of 3.75 minutes. The voltages are scaled to lie between 0 and 1. *C* stands for circuit model, *M* stands for measurement data, and *MB* stands for measurement data calculated from Bøckman measurements.

## Appendix D. Results for second data set

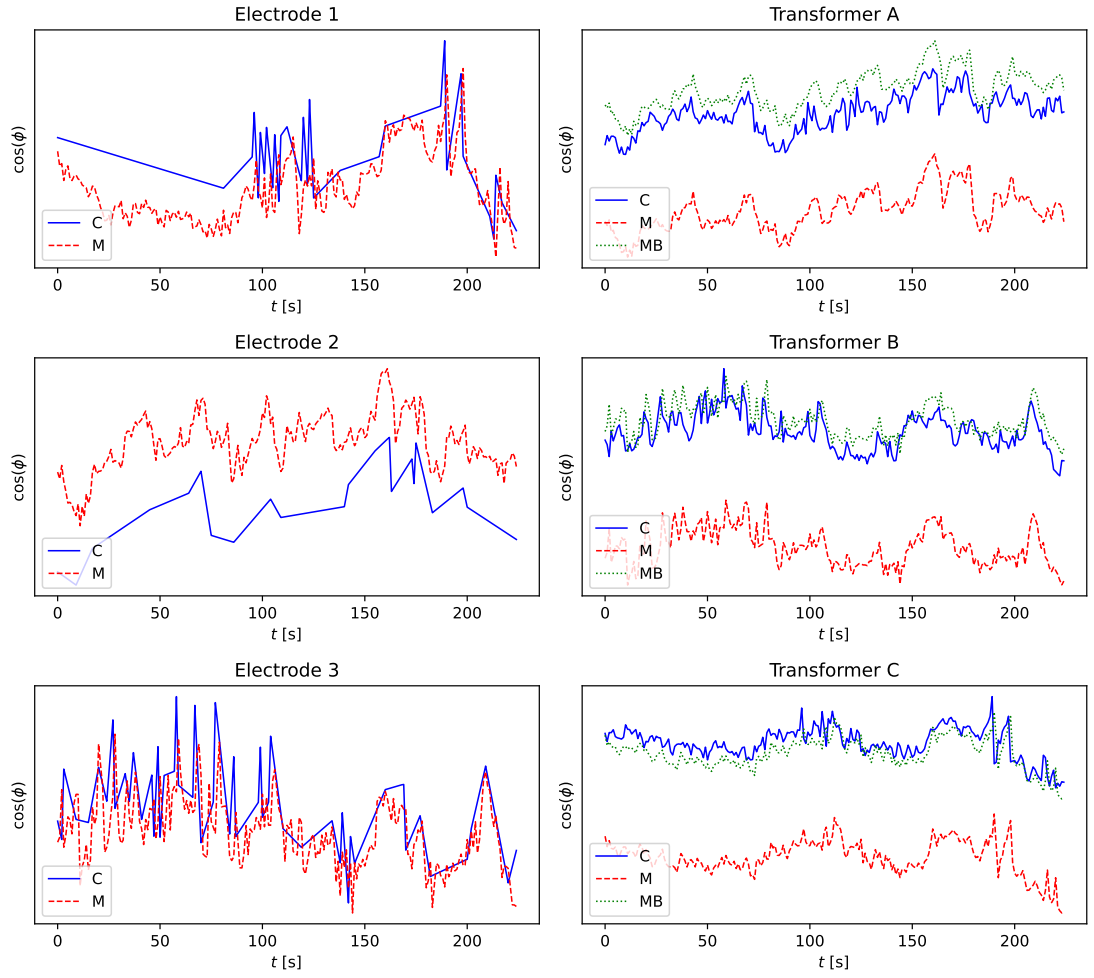


Figure D.4: Comparison of power factor from the full equivalent circuit model *HVC* and power factor from high-resolution measurement data for the data set of 3.75 minutes. The y axes are linear. C stands for circuit model, M stands for measurement data, and MB stands for measurement data calculated from Bøckman measurements.

**Table D.1:** R.m.s. error of values calculated with the full circuit model compared to high-resolution measurement data for the data set of 3.75 minutes. All currents and voltages have been scaled to lie between 0 and 1 before calculating the error.

Electrodes		Transformers		Transformers (Bøckman)	
Quantity	Error	Quantity	Error	Quantity	Error
$I_1$	$6.942 \cdot 10^{-3}$	$I_A$	$5.372 \cdot 10^{-3}$	—	—
$I_2$	$4.866 \cdot 10^{-3}$	$I_B$	$9.844 \cdot 10^{-4}$	—	—
$I_3$	$1.931 \cdot 10^{-3}$	$I_C$	$1.733 \cdot 10^{-3}$	—	—
$V_1$	$1.686 \cdot 10^{-3}$	$V_A$	$2.626 \cdot 10^{-3}$	$V_{A,\text{Bok}}$	$2.663 \cdot 10^{-3}$
$V_2$	$1.978 \cdot 10^{-3}$	$V_B$	$2.786 \cdot 10^{-3}$	$V_{B,\text{Bok}}$	$2.813 \cdot 10^{-3}$
$V_3$	$1.274 \cdot 10^{-3}$	$V_C$	$2.169 \cdot 10^{-3}$	$V_{C,\text{Bok}}$	$2.185 \cdot 10^{-3}$
$\cos \phi_1$	$7.315 \cdot 10^{-4}$	$\cos \phi_A$	$3.422 \cdot 10^{-3}$	$\cos \phi_{A,\text{Bok}}$	$8.581 \cdot 10^{-4}$
$\cos \phi_2$	$1.455 \cdot 10^{-3}$	$\cos \phi_B$	$3.682 \cdot 10^{-3}$	$\cos \phi_{B,\text{Bok}}$	$5.573 \cdot 10^{-4}$
$\cos \phi_3$	$4.960 \cdot 10^{-4}$	$\cos \phi_C$	$4.795 \cdot 10^{-3}$	$\cos \phi_{C,\text{Bok}}$	$6.146 \cdot 10^{-4}$

## Appendix D. Results for second data set



# Bibliography

- [1] M. Gasik, 'Introduction,' in *Handbook of Ferroalloys: Theory and Technology*, M. Gasik, Ed., Oxford, U.K.: Butterworth-Heinemann, 2013, pp. 3–7.
- [2] A. B. Stewart, 'An analysis of the electrical circuit of submerged-arc furnaces,' Ph.D. thesis, Dept. Elect. Eng., Univ. Cape Town, Cape Town, South Africa, 1980. [Online]. Available: <http://hdl.handle.net/11427/14048>
- [3] M. Tangstad, 'Ferrosilicon and silicon technology,' in *Handbook of Ferroalloys: Theory and Technology*, M. Gasik, Ed., Oxford, U.K.: Butterworth-Heinemann, 2013, ch. 6, pp. 179–220.
- [4] A. M. Valderhaug, 'Modelling and control of submerged-arc ferrosilicon furnaces,' Ph.D. thesis, Dept. Eng. Cybern., Norwegian Univ. Sci. Technol., Trondheim, Norway, 1992. [Online]. Available: <http://hdl.handle.net/11250/260770>
- [5] M. Gasik, Ed., *Handbook of Ferroalloys: Theory and Technology*, Oxford, U.K.: Butterworth-Heinemann, 2013.
- [6] I. Mc Dougall, 'Ferroalloys processing equipment,' in *Handbook of Ferroalloys: Theory and Technology*, M. Gasik, Ed., Oxford, U.K.: Butterworth-Heinemann, 2013, ch. 4, pp. 83–138.
- [7] P. Hannesson. 'Drawings - si-process.pdf,' elkem.com, Accessed: Apr. 23, 2025. [Online]. Available: <https://www.elkem.com/globalassets/iceland/si-process.pdf>
- [8] W. Braun, T. Nettleton and A. Jamieson, 'Advanced furnace control,' in *Infacon VIII: Int. Ferro-Alloys Congr.*, Beijing, China, Jun. 1998, pp. 332–336.
- [9] R. Innvær, K. Fidje and T. Sira, '3-dimensional calculations on smelting electrodes,' *Model., Identification and Control*, vol. 8, no. 2, pp. 103–115, Apr. 1987. doi: 10.4173/mic.1987.2.3.
- [10] A. Bermúdez, J. Bullón and F. Pena, 'A finite element method for the thermoelectrical modelling of electrodes,' *Commun. Numer. Methods Eng.*, vol. 14, no. 6, pp. 581–593, Dec. 1998. doi: 10.1002/(SICI)1099-0887(199806)14:6<581::AID-CNM175>3.0.CO;2-S.
- [11] I. M. Dougall, C. F. R. Smith, B. Olmstead and W. A. Gericke, 'A finite element model of a søderberg electrode with an application in casing design,' in *Infacon X: Int. Ferro-Alloys Congr.*, Cape Town, South Africa, Feb. 2004, pp. 575–584.
- [12] H. T. Ingason and M. T. Jonsson, 'A three dimensional simulation model for a soderberg electrode,' in *Infacon VIII: Int. Ferro-Alloys Congr.*, Beijing, China, Jun. 1998, pp. 383–388.
- [13] K. Fidje, R. Innvær and R. Ugland, 'Effect of current variations on material properties and thermal stresses in søderberg electrodes,' in *Infacon IV: Int. Ferro-Alloys Congr.*, Rio de Janeiro, Brazil, Sep. 1986, pp. 321–330.

- [14] S. A. Halvorsen, H. A. H. Olsen and M. Fromreide, 'An efficient simulation method for current and power distribution in 3-phase electrical smelting furnaces,' *IFAC-PapersOnLine*, vol. 49, no. 20, pp. 167–172, Jan. 2016. doi: 10.1016/j.ifacol.2016.10.115.
- [15] M. Dhainaut, 'Simulation of the electric field in a submerged arc furnace,' in *Infacon X: Int. Ferro-Alloys Congr.*, Cape Town, South Africa, Feb. 2004, pp. 605–613.
- [16] Y. A. Tesfahunegn, T. Magnusson, M. Tangstad and G. Saevarsdottir, 'Dynamic current distribution in the electrodes of submerged arc furnace using scalar and vector potentials,' in *Int. Conf. Comput. Sci.*, Y. Shi, H. Fu, Y. Tian et al., Eds., Wuxi, China, Jun. 2018, pp. 518–527. doi: 10.1007/978-3-319-93701-4\_40.
- [17] I. Mc Dougall, 'Finite element modelling of electric currents in ac submerged arc furnaces,' in *Infacon XI: Int. Ferro-Alloys Congr.*, New Delhi, India, Feb. 2007, pp. 630–637.
- [18] B. Larsen, H. Feldborg and S. A. Halvorsen, 'Minimizing thermal stress during shutdown of søderberg electrodes,' in *Infacon XIII: Int. Ferro-Alloys Congr.*, Almaty, Kazakhstan, Jun. 2013, pp. 453–466.
- [19] L. H. Gunnewiek, L. Oshinowo, T. Plikas and R. Haywood, 'The application of numerical modelling to the design of electric furnaces,' in *Infacon X: Int. Ferro-Alloys Congr.*, Cape Town, South Africa, Feb. 2004, pp. 555–564.
- [20] I. J. Barker, 'An electrode controller for submerged arc furnaces,' *IFAC Proc. Volumes*, vol. 13, no. 7, pp. 611–621, Jan. 1980. doi: 10.1016/s1474-6670(17)64768-2.
- [21] M. A. Reuter, M. Oosthuizen, I. J. Barker, M. S. Rennie and A. de Waal, 'The dynamic response of submerged-arc furnaces to electrode movement,' *IFAC Proc. Volumes*, vol. 28, no. 17, pp. 121–127, Aug. 1995. doi: 10.1016/s1474-6670(17)46753-x.
- [22] N. Storey, *Electronics: A Systems Approach*, 6th ed. Harlow, U.K.: Pearson, 2017.
- [23] W. G. Hurley and W. H. Wölflé, *Transformers and Inductors for Power Electronics: Theory, Design and Applications*. Chichester, U.K.: Wiley, 2014.
- [24] A. R. Daniels, *Introduction to Electrical Machines*, Reprinted. London, U.K.: Macmillan, 1979.
- [25] A. von Meier, *Electric Power Systems: A Conceptual Introduction*. Hoboken, New Jersey, USA: Wiley, 2006.
- [26] P. M. Anderson, 'Symmetrical components,' in *Analysis of Faulted Power Systems*, Reprinted, New York, NY, USA: Wiley-IEEE Press, 1995, ch. 2, pp. 19–35.
- [27] *IEEE guide for identifying and improving voltage quality in power systems*, IEEE Standard 1250-2011 (Revision of IEEE Standard 1250-1995), 2011. [Online]. Available: <https://ieeexplore.ieee.org/document/5744556/>
- [28] J. Meintjes, 'A comparison of power-factor correction on submerged-arc furnaces by capacitors in shunt and series,' in *Infacon I: Int. Ferro-Alloys Congr.*, Johannesburg, South Africa, Apr. 1974, pp. 149–155.
- [29] G. Saevarsdottir, 'Electric and thermal operations of furnaces for ferroalloys production,' in *Handbook of Ferroalloys: Theory and Technology*, M. Gasik, Ed., Oxford, U.K.: Butterworth-Heinemann, 2013, ch. 5, pp. 139–175.

- [30] A. Bermúdez, D. Gómez and P. Salgado, *Mathematical Models and Numerical Simulation in Electromagnetism*. Cham, Switzerland: Springer, 2014. doi: 10.1007/978-3-319-02949-8.
- [31] S. K. Yadav, *Discrete Mathematics with Graph Theory*. Cham, Switzerland: Springer, 2023. doi: 10.1007/978-3-031-21321-2.
- [32] I. J. Barker and A. B. Stewart, ‘Inductive reactance, and the operation of large submerged-arc furnaces,’ *J. South Afr. Inst. Mining Metall.*, vol. 80, no. 3, pp. 123–128, 1980.
- [33] Z. Li, S. Chu, X. Tao, T. Li, J. Zhang and X. Bao, ‘Compensation of submerged arc furnace by capacitors connected in shunt on low voltage side,’ presented at the Infacon XV: Int. Ferro-Alloys Congr. Cape Town, South Africa, Feb. 2018.
- [34] G. A. Sævarsdóttir, P. Manolescu, P. Magnússon and K. Sigurjonsson, ‘Circulating currents in the delta connection, feasibility of skew tapping in the operation of submerged-arc furnaces,’ in *Infacon XIII: Int. Ferro-Alloys Congr.*, Almaty, Kazakhstan, Jun. 2013, pp. 443–452.
- [35] M. Sparta, D. Varagnolo, K. Stråbø, S. A. Halvorsen, E. V. Herland and H. Martens, ‘Metamodeling of the electrical conditions in submerged arc furnaces,’ *Metall. Mater. Trans. B*, vol. 52, no. 3, pp. 1267–1278, Jun. 2021. doi: 10.1007/s11663-021-02089-7.
- [36] ‘SAFECEI - smelting furnace electrical conditions metamodel,’ Accessed: Mar. 10, 2025. [Online]. Available: <https://safeci.web.norce.cloud/>
- [37] M. Sparta, M. Fromreide, V. K. Risinggård and S. A. Halvorsen, ‘Electrical conditions in submerged arc furnaces: A web-based simulator,’ in *Proc. Silicon Chem. Solar Industry XVI*, Trondheim, Norway, Jun. 2022. doi: 10.2139/ssrn.4118651.
- [38] A. De Waal, I. J. Barker, M. S. Rennie, J. Klopper and B. S. Groeneveld, ‘Electrical factors affecting the economic optimization of submerged-arc furnaces,’ in *Infacon VI: Int. Ferro-Alloys Congr.*, Cape Town, South Africa, Mar. 1992, pp. 247–252.
- [39] I. J. Barker, A. De Waal, M. S. Rennie and J. Klopper, ‘The interaction effect in submerged-arc furnaces,’ in *Proc. 49th Elect. Furnace Conf.*, Toronto, Canada, Nov. 1991, pp. 305–310.
- [40] M. Sparta, V. K. Risinggård and U. Thisted, ‘Bøckman method for measuring furnace core voltages: A modeling review,’ in *Proc. Silicon Chem. Solar Industry XVII*, Trondheim, Norway, Sep. 2024. doi: 10.2139/ssrn.4942623.
- [41] M. H. Samimi, A. Mahari, M. A. Farahnakian and H. Mohseni, ‘The rogowski coil principles and applications: A review,’ *IEEE Sensors J.*, vol. 15, no. 2, pp. 651–658, Feb. 2015. doi: 10.1109/JSEN.2014.2362940.
- [42] A. Luque. ‘File:rogowski coil.png - wikipedia commons,’ commons.wikimedia.org. Licensed under CC BY-SA 3.0. Accessed: Mar. 24, 2025. [Online]. Available: [https://commons.wikimedia.org/w/index.php?title=File:Rogowski\\_coil.png&oldid=554386218](https://commons.wikimedia.org/w/index.php?title=File:Rogowski_coil.png&oldid=554386218)
- [43] O. C. Bøckman, ‘Anordning for måling av kraterspenningene i en trefase smelteovn med elektrodene i trekant,’ Patent NO126288B, Jan. 15, 1973.
- [44] O. C. Bøckman, ‘Arrangement for measuring the crater voltages in a three-phase electric furnace with electrodes arranged in a delta,’ U.S. Patent 3757021A, Sep. 4, 1973.

- [45] A. Meurer, C. P. Smith, M. Paprocki et al., ‘SymPy: Symbolic computing in python,’ *PeerJ Comput. Sci.*, vol. 3, e103, Jan. 2017. doi: 10.7717/peerj-cs.103.
- [46] C. R. Harris, K. J. Millman, S. J. van der Walt et al., ‘Array programming with numpy,’ *Nature*, vol. 585, no. 7825, pp. 357–362, Sep. 2020. doi: 10.1038/s41586-020-2649-2.
- [47] J. D. Hunter, ‘Matplotlib: A 2d graphics environment,’ *Comput. Sci. Eng.*, vol. 9, no. 3, pp. 90–95, May 2007. doi: 10.1109/MCSE.2007.55.
- [48] M. L. Waskom, ‘Seaborn: Statistical data visualization,’ *J. Open Source Softw.*, vol. 6, no. 60, p. 3021, Apr. 2021. doi: 10.21105/joss.03021.
- [49] The pandas development team, *pandas-dev/pandas: Pandas*, (v2.1.4). Zenodo. [Online]. Available: <https://zenodo.org/records/10304236>
- [50] W. McKinney, ‘Data structures for statistical computing in python,’ in *Python Sci. Conf.*, Austin, Texas, USA, Jun. 2010, pp. 56–61. doi: 10.25080/Majora-92bf1922-00a.
- [51] I. Monsen. ‘Idamonse/master\_\_thesis,’ GitHub UiO. [Online]. Available: [https://github.uio.no/idamonse/master\\_\\_thesis](https://github.uio.no/idamonse/master__thesis)
- [52] P. Virtanen, R. Gommers, T. E. Oliphant et al., ‘Scipy 1.0: Fundamental algorithms for scientific computing in python,’ *Nature Methods*, vol. 17, no. 3, pp. 261–272, Feb. 2020. doi: 10.1038/s41592-019-0686-2.
- [53] A. I. Vistnes, ‘Fourier analysis,’ in *Physics of Oscillations and Waves: With use of Matlab and Python*, Cham, Switzerland: Springer, 2018, ch. 5, pp. 93–134.
- [54] ‘Discrete fourier transforms (scipy.fft) — SciPy v1.15.2 manual,’ [docs.scipy.org](https://docs.scipy.org/doc/scipy/reference/fft.html), Accessed: Apr. 25, 2025. [Online]. Available: <https://docs.scipy.org/doc/scipy/reference/fft.html>